NTNU

Norwegian University of
Science and Technology

Characterization of precipitates at maximum hardness and overaged conditions in Al-Mg-Si alloys

Halfdan Kristoffer Småbråten

Chemical Engineering and Biotechnology
Submission date: June 2011
Supervisor: Knut Marthinsen, IMTE
Co-supervisor: Sverre Gulbrandsen-Dahl, SINTEF Raufoss Manufacturing AS

Norwegian University of Science and Technology
Department of Materials Science and Engineering

Declaration

I hereby declare that the master thesis is carried out independently and pursuant to the examination regulations at the Norwegian University of Science and Technology (NTNU).

Halfdan Kristoffer Småbråten
16.06.2011, Trondheim

Abstract

A study of the influence of artificial ageing temperature on the precipitation behaviour in three distinct direct chill casted and extruded Al-Mg-Si alloys has been carried out. The total amount of alloying elements is approximately the same in these alloys, but the difference is the ratio between these elements. The master thesis is a continuation of the work reported in *Characterization of precipitates at maximum hardness in Al-Mg-Si alloys* which was written in connection to the course *TMT4500 Materials Technology, Specialization Project*. The primary objective of this work was to identify the value of maximum hardness, and at what time it is obtained for these alloys after they have been artificially aged, one set at 200 °C and another at 250 °C, i.e. six cases in total. The aim in the master thesis has been to investigate which type and relative amount of needle shaped precipitates that are present, and what size, number density and volume fraction that is responsible for these conditions by using transmission electron microscopy (TEM). In addition, all three alloys have been shown to obtain a local hardness maximum at overaged conditions in the 200 °C case. These conditions have also been analysed by comparing with an overaged condition for KK5 for an ageing time shorter than the one were the local maximum appears. Therefore, ten different conditions have been investigated in total.

One sample has been selected from each case based on the hardness curves in the project work, and prepared for analysis in two different TEM instruments. A number of general trends between alloy composition, heat treatment, and the resulting microstructure and hardness that already have been reported, have been verified during the master thesis. The maximum hardness conditions after artificial ageing at 200 °C have been found to be quite different for KK5, KK6 and KK7 in terms of type and relative amount of precipitates, and precipitate size and number density. Artificial ageing at 250 °C has been observed to give very similar values of maximum hardness for the three alloys primarily due to the size and number density of the precipitates. The local maximum hardness peaks observed at overaged conditions after artificial ageing at 200 °C have been seen to be purely due to precipitate size and number density, but the reason for their appearance has not been clarified. The observed differences between the three alloys in each condition and the differences between the conditions themselves for each alloy have been seen to be reflected in both type and relative amount of precipitates, and precipitate size and number density.

Preface

This report was written in the context of the master's degree programme Chemical Engineering and Biotechnology at NTNU as a part of the course Materials Chemistry and Energy Technology, master thesis. The work in this report is a continuation of the project work in the course *TMT4500 Materials Technology, Specialization Project* and is based on and gives supplemental results to a project called *Kimdanningskontroll for optimaliserte egenskaper* which is a collaboration between Hydro, SINTEF Raufoss Manufacturing AS, Steertec Raufoss AS and NTNU.

Throughout the master thesis I have positively developed my English, both in writing and oral, in addition to my report writing skills. My common understanding of metals in general has grown a lot in addition to detailed knowledge of the AA6xxx alloys. During the master thesis I have become a better collaborator and learned much about taking responsibility in every aspect of the work. Overall, this was a good learning experience which really prepared me for a future relevant job and represented a "springboard" into the job market.

Acknowledgements

Foremost, I would like to express my sincere gratitude to my supervisor professor Knut Marthinsen for the continuous guidance throughout of my master thesis, and to co-supervisor post doc Sverre Gulbrandsen-Dahl for general discussion and feedback on the experimental results. I appreciate all their contributions of time and effort to make my master thesis productive and stimulating.

I wish to thank PhD candidate Maulid Kivambe and Staff Engineer Bjørn Gunnar Soleim for giving me lessons at the transmission electron microscopes JEOL JEM-2010 and Philips CM30, respectively. Without their help, the research in this thesis would have taken far longer to complete.

It is difficult to overstate my gratitude to two of my colleagues at the KK-project, scientist Calin Marioara and PhD candidate Katharina Teichmann. They have both been a source of good advice as well as collaboration.

Many thanks also go to senior engineer Pål Ulseth for teaching me TEM sample preparation, and to senior engineer Yingda Yu for showing me ion milling and plasma etching, and for teaching me EELS and FFT at the JEOL JEM-2010 transmission electron microscope.

I am indebted to my many fellow students for providing a stimulating and fun environment, and for making this my best semester at NTNU.

Most importantly, none of this would have been possible without the love and encouragement of my family. I would like to thank my parents who raised and supported me in all my pursuits and for the presence of my brother at NTNU for two of my years.

Table of Contents

1. Introduction

Al-Mg-Si based alloys, also known as the AA6xxx alloys, have attracted much industrial attention throughout the years due to their good mechanical properties, and have a wide range of applications in the automotive, aerospace, aircraft, and construction industries [1]. In the continuing drive for automobile weight reduction, Al-Mg-Si alloys are considered to be the most promising candidates for heat treatable body sheet materials [2] as well as cylinder heads and wheels [3]. Methods to develop high performance Al-Mg-Si alloys are therefore very important. In the manufacturing process, these alloys are subjected to room temperature storage and heat treatment at more elevated temperatures (around 175 °C) which is known as artificial ageing. This heat treatment improves the mechanical properties of the alloys and is the last step in a strengthening process known as age or precipitation hardening. The classical representation of the precipitation sequence that arises during artificial ageing of the Al-Mg-Si alloys is given in Equation 1.1 [4].

$$SSSS \rightarrow GP-zones \rightarrow \beta'' \rightarrow \beta' \rightarrow \beta \tag{1.1}$$

The Al-Mg-Si alloys have in general been reported to be strengthened primarily by the β" phase [5] which also gives the maximum hardness [6]. However, this has been proven to be a very simplified version of the reality. A more complete picture involves clusters and metastable post-β" precipitates. However, the mechanical response and hardening effect of each of the post-β" precipitates are less studied, and in commercial alloys the precipitate structure is often a mixture of different precipitates. The knowledge of the mechanical effect of each type of precipitate may therefore be a significant contribution to further optimization of these alloys.

The work done in the master thesis is a contribution to a project called *Kimdanningskontroll for optimaliserte egenskaper*, also known as the KK project. This project is a collaboration between *Hydro*, *SINTEF Raufoss Manufacturing AS*, *Steertec Raufoss AS* and *NTNU*, and is co-funded by *Hydro*, *Steertec Raufoss* and *The Research Council of Norway*. In the KK project a number of direct-chill casted and extruded AA6xxx type alloys with different compositions are investigated to understand the relationship between microstructure and mechanical behaviour in order to optimize the hardening structure for different utilizations.

This include to make a survey of the nucleation of the precipitates in an early phase, and to manipulate the precipitation to get better properties in the alloys by affecting the number density and the volume fraction of the precipitates, and what type of precipitates that form [7].

It has been shown that Al-Mg-Si alloys form different precipitates of different amounts that vary in size, number density and volume fraction at underageing, maximum hardness and overageing [4]. This formation is dependent on alloy chemistry, room temperature storage time, and artificial ageing time and temperature. The work in this thesis is based on investigations of three distinct alloys called KK5, KK6 and KK6 with different compositions which are to be artificial aged at 200 °C and 250 °C in two separate sets. The aim has been to

- Determine what type of precipitates that are present at maximum hardness after artificial ageing at 200 °C and 250 °C in addition to determine the size, number density and volume fraction of these precipitates. This is done because it is desirable to know how to obtain as hard materials as possible for short ageing times and without too much hardness decrease due to overageing.

- Determine what type of precipitates that are present at obtained local maximum hardness peaks at overaged conditions after artificial ageing at 200 °C in addition to determine the size, number density and volume fraction of these precipitates by comparing with a sample which represents the overaged condition in general. This is done two understand the reason for the observed hardness peaks that deviate from the general decreasing trend in hardness at overaged conditions.

Both the maximum hardness peaks and the local maximum hardness peaks have been localized by hardness measurements in the project work last semester where measurements of electrical conductivities were done to assist the indication of precipitation and growth. This semester, the samples that represent these conditions have been prepared and analysed by transmission electron microscopy. This was done for all three alloys. The results from this work are only a tiny part of all the data which are to be gathered and analysed in the KK project.

2. Theoretical background

This section is supposed to give a short introduction to the theory prior to the master thesis. Both material processing and metallurgy on one hand, and experimental investigation methods on the other hand, will be presented.

2.1. AA6xxx alloys

Al-Mg-Si alloys (AA6xxx) are classified as heat-treatable wrought alloys [8]. These are widely used as medium strength structural alloys that can be strengthened by heat treatment through the presence of their main alloying elements silicon and magnesium (mostly in the range 0.3-1.5 wt% Si and Mg) [9]. These alloys have a good combination of high strength, formability, weldability, corrosion resistance and immunity to stress corrosion cracking, and have a vast variety of applications. Among the alloys used for extrusions, more than 90 % is covered by the these alloys [7], with smaller quantities being available as sheets and plates [3]. The strength in AA6xxx alloys may be increased by hardening caused by precipitates formed from solution, of merely 1 wt% of Mg and Si that is added to the aluminium [10]. The maximum hardness is achieved when the alloy contains a combination of very fine fully coherent so called Guinier Preston (GP-I) zones with diameters about 2.5 nm, and the semicoherent, larger needles, β" (GP-II zones), with a typical size 4x4x50 nm^3 and a composition known as Mg_5Si_6. Silicon improves the fluidity of the molten alloy and reduces the susceptibility to form hot crevices during solidification and heating [9]. It gives better corrosion resistance, but too much silicon reduces the machinability. Magnesium increases work hardening due to Mg in solid solution and makes the protecting oxide layer more anti-soluble which in turn also increases the corrosion resistance [8]. Other alloying elements like calcium, chromium, manganese, led and bismuth are also common.

The good combination of mechanical properties makes the AA6xxx alloys interesting in applications like transport (automotive outer body-panels, railcars, etc), building (doors, windows, ladders, etc), marine (offshore structures, etc) and heating (brazing sheet, etc) among others [9]. In the continuing drive for automobile weight reduction, these alloys are considered to be the most promising candidates for heat treatable body sheet materials [2].
The atoms in aluminium are arranged in a face-centred cubic (fcc) structure which is illustrated in Figure 2.1 (a) [11]. This crystal structure has a unit cell of cubic symmetry with

atoms located at each of the corners and the centres of all the cube faces. It is often necessary to be able to specify certain directions and planes in the crystal structure which can be described by using three Miller indices. The precipitates in the AA6xxx alloys are known to be needle or lath shaped oriented along the <100> directions in the aluminium fcc crystal system [12]. Thus, the precipitates will be oriented along the [100], [010] and [001] directions within the aluminium matrix. An [100] direction and an (100) plane are therefore illustrated in Figures 2.1 (b) and (c) [11].

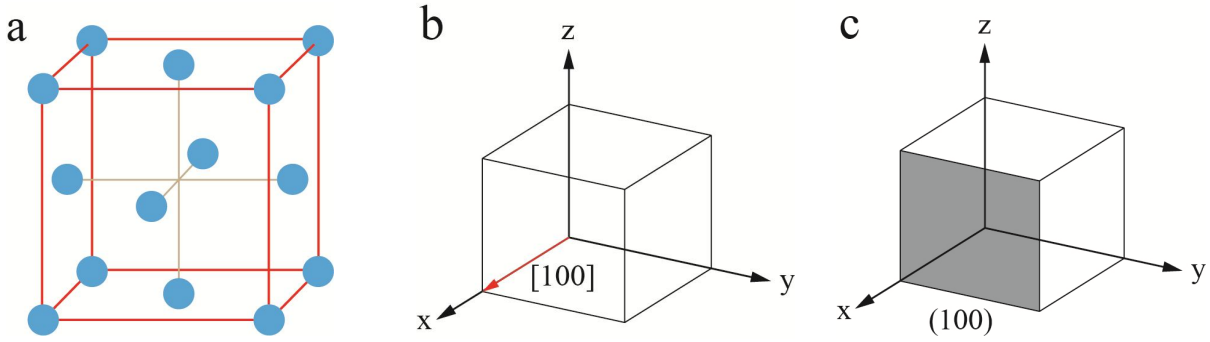

Figure 2.1: (a) fcc structure, (b) [100] direction in fcc and (c) (100) plane in fcc [11]

2.2. Casting and extrusion

In general, there are two principal classifications of aluminium alloys, namely casting alloys and wrought alloys, both of which are further divided into the subcategories heat-treatable and non-heat-treatable [8]. For heat-treatable alloys the mechanical properties can be tuned through thermal treatment, while the mechanical properties of the non-heat-treatable alloys are obtained through hot and/or cold working mechanisms. Casting is a forming operation where cast alloys are directly cast into their final shape by one of various methods such as sand-casting, die or pressure die casting [9]. This is a widely used method to obtain complex product shapes. Cast alloys are strengthened only by their alloying elements. For that reason, the cast alloys are often rich in alloying elements [8]. Wrought alloys are meant for plastic forming like rolling, drawing, forging and extrusion [3]. These alloys have to be ductile and give little resistance against deformation [8]. Thus, they often have a low amount of alloying elements. About 75-80 % of aluminium is used for wrought products which are produced from cast ingots [3]. Only the production of extruded wrought alloys, which consists of casting and extrusion, will be further discussed.

2.2.1. Casting

The production of wrought, extruded products starts with casting of an ingot [3]. Direct-chill (DC) casting is used to obtain a uniform ingot structure, normally in the vertical process where the molten alloy is poured into one or several fixed water-cooled moulds. Aluminium has a very good casting behaviour due to the fact that the melt is easy floating (low viscosity) and the setting temperature is low [8]. Addition of silicon lowers the viscosity and minimizes the volume reduction during setting. Both the viscosity and the volume reduction are at the lowest values near the eutectic point for Al-Si alloys (this is valid for pure metal and generally for eutectic alloys).

2.2.2. Extrusion

The last step in producing extruded wrought alloys, is the extrusion of the casted ingots [3]. Extrusion is a process used to create rods and tubing of a fixed cross sectional profile where a bar of metal is forced through a die orifice with the desired shape by a compressive force that is applied to a ram [11]. Extrusion of aluminium alloys offers a relatively cheap method of producing complex shapes in long lengths with high geometric tolerances [13]. Aluminium extrusions are used in areas such as shipping and offshore industry, furniture, the building industry (window and door frames, building structures, roofing, curtain walling, etc.), and in the transportation sector for aerospace applications, rail vehicles and automotive applications. As mentioned in Chapter 2.1, more than 90% of the total extruded volume is estimated to be made from the AA6xxx alloys due to an attractive combination of properties [9].

The deformation may be done at temperatures above that at which recrystallization occurs which is termed hot working [11]. This process enables large deformations which may be successively repeated because the metal remains soft and ductile. When the deformation is done at temperatures below the recrystallization temperature, the process is called cold working. Here the material strain hardens which gives an increase in strength with the corresponding decrease in ductility. Cold working requires more energy than hot working, but the advantages include a higher quality surface finish, better mechanical properties and a greater variety of them, and a closer dimensional control of the finished piece.

During successive extrusion of a number of billets, some remains from the first extruded billet is left in the camber weld [14]. When the material of a billet bonds with this residue, severely curved surfaces called charge welds, or transverse welds, are made. Due to the adhesion of

aluminium to the tool surface, the flat contact surface is deformed into a tongue as illustrated in Figure 2.2 [15]. The result is that some remains of the first billet covers the first centimeters of the second billet and so on. This part is regarded as scrap and has to be cut away. In the case extrusion of hollow sections, the billet is divided into two or more streams that flow together before the hollow section is formed by metallic bonding of the stream [14]. During this process, seam welds (or longitudinal welds) are formed. When billets of the same material is extruded successively, the charge welds are still cut away because the weld regions have been reported to be less ductile than the no-weld regions [15].

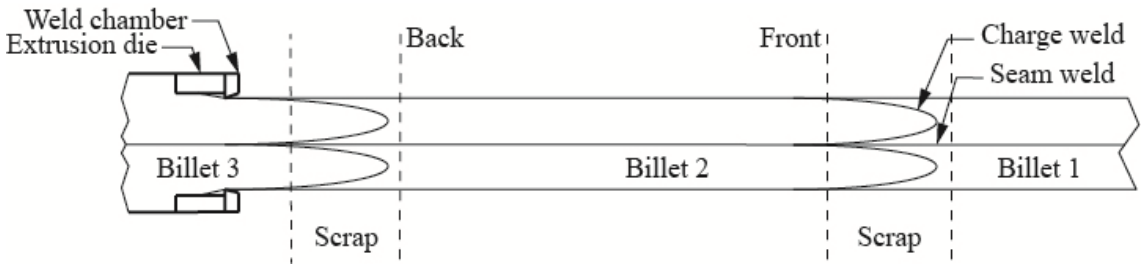

Figure 2.2: Successive extrusion showing the seam weld and the charge weld [15]

A sketch of the different process steps in a general production of aluminium extrusions is given in Figure 2.3 [13]. Melting and alloying, die casting of extrusion ingots and homogenisation of the ingots are all done in the cast house. Then the ingots are preheated to the desired extrusion temperature, extruded, cooled, stretched and aged at an extrusion plant.

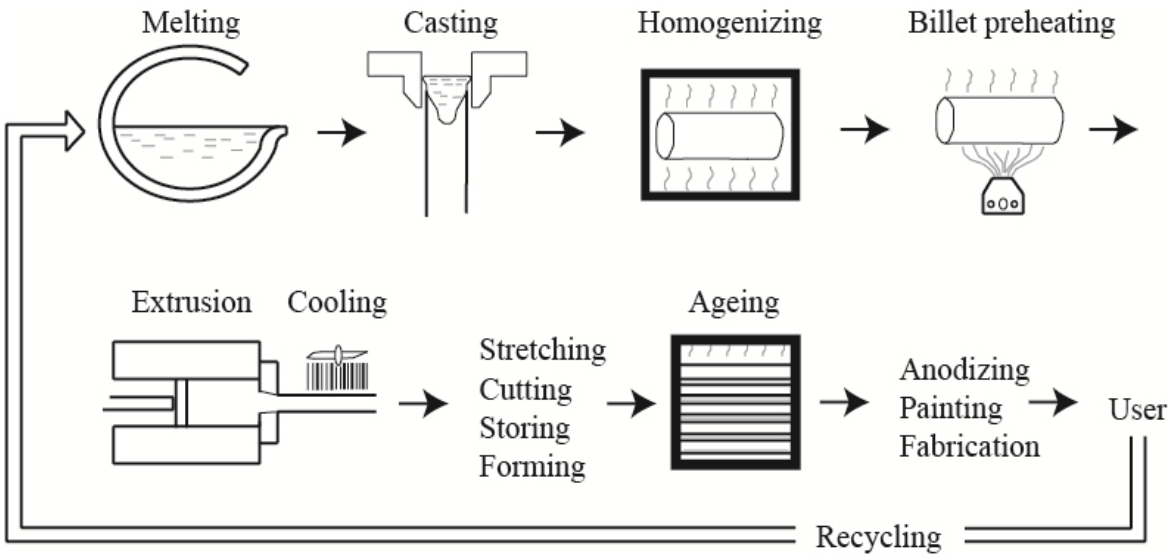

Figure 2.3: The different process steps related to the production of extrusions [13]

The extrusion speed may be limited by available pressure, unbalanced metal flow, geometric tolerances and the occurrence of surface defects like die lines, pick-ups, tearing or hot shortness, and spalling [13]. All these factors lower the productivity in an extrusion plant. One very important reason for speed limiting surface defects is the onset of local melting reactions in the material during extrusion.

The maximum extrusion speed is also affected by the billet preheating temperature which can be presented in the form of an extrusion limit diagram as in Figure 2.4 [13]. At low billet temperatures, the extrusion speed is limited by available pressure of the press due to the high deformation resistance at these temperatures. At higher billet temperatures, the maximum extrusion speed decreases with increasing billet temperatures because of limitations in the quality of the extrusions.

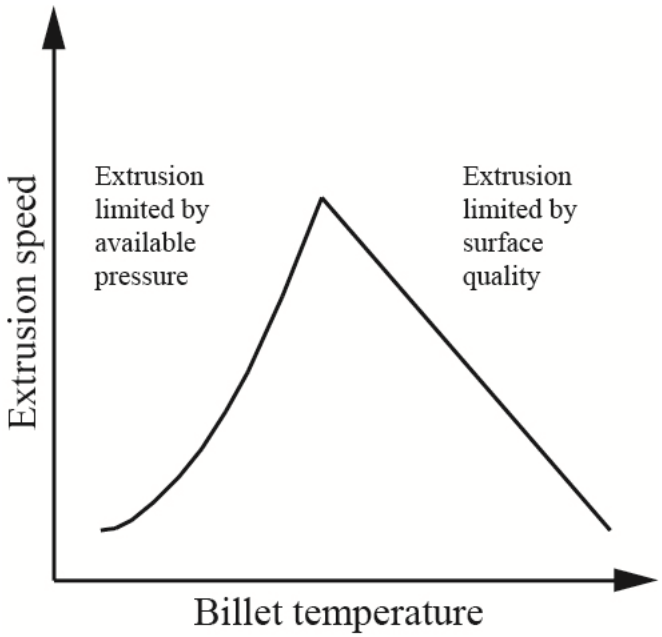

Figure 2.4: Sketch of an extrusion limit diagram [13]

The heating rate to the homogenization temperature, the homogenization temperature and time as well as the cooling rate from the homogenization temperature may all influence extrudability and section properties [13]. The extrudability is increasing with increasing cooling rate after homogenization due to changes in the microstructure. High cooling rates may be obtained by water quenching. However, because of the challenges regarding water quenching of the extruded sections (distortion, water staining, etc.), forced air cooling from the homogenization temperature is recommended.

The temperature and time-course through a general extrusion of Al-Mg-Si alloys steps with indications of typical temperatures and times used is given in Figure 2.5 [13].

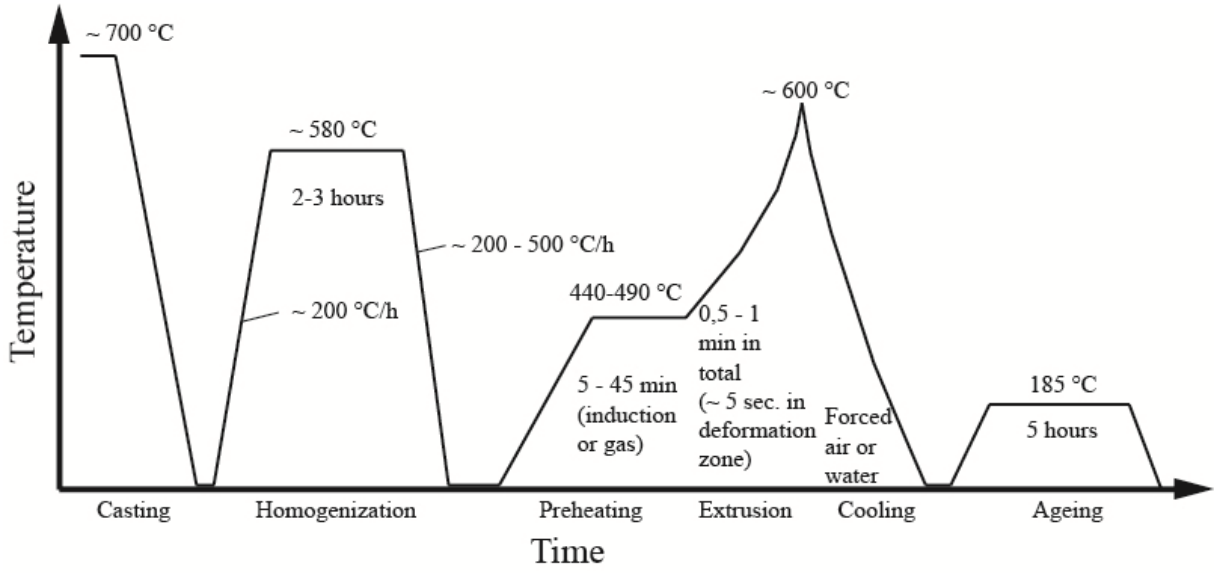

Figure 2.5: The temperature/time profile for the production of extrusions with typical temperatures and times used for Al-Mg-Si alloys indicated [13]

Addition of magnesium and silicon to aluminium tends to lower the maximum extrusion speed before tearing occurs in the surface of the extrusion [13]. For that reason, the extrudability of AA6xxx alloys is strongly affected by their microstructure which is dependent on their alloy compositions. First of all, at a relatively low Mg and Si content, the tearing on the surface is observed at profile exit temperatures close to the solidus temperatures of the alloys. The concentration of Mg and Si determines the solidus temperature and has an impact on the deformation resistance. Increasing content of Mg and Si decreases the solidus temperature and increases the deformation resistance. Secondly, at higher alloy compositions, Mg_2Si will start to precipitate before the material is extruded. These particles reduce the extrudability even further due to the onset of melting in the material at a lower temperature. Therefore, in the selection of alloy composition, a compromise has to be made between the alloy strength and the extrusion productivity.

It seems like there exists an optimum billet preheating temperature in order to maximise the extrusion speed as seen in Figure 2.4. However, a higher billet temperature is used for several reasons [13]. For Al-Mg-Si alloys, it has been shown that when billets are heated directly to a desired temperature, the maximum extrusion speed decreases with increasing billet

temperature. At a certain billet temperature, the curve is shifted upwards to a higher extrusion speeds before the speed again decreases with increasing billet temperatures. This phenomenon is due to the existence of large Mg_2Si particles at low billet temperatures which may cause internal melting when the eutectic temperature is exceeded during extrusion, and initiate surface tearing. However, at a higher preheating temperature, the Mg_2Si particles will dissolve and the eutectic temperature may be exceeded during extrusion without risking melting reactions. Experiments indicate that billets that has been overheated prior to extrusion to dissolve the Mg_2Si particles, can be extruded at significantly higher speeds than billets heated directly to the same temperature [13]. This is explained by the fact that the overheated billets were cooled down to temperatures below the Mg_2Si solvus temperature quick enough to avoid any new precipitation of Mg_2Si particles before they were extruded. Thus, the critical temperature for tearing initiation is higher in these billets than compared to the directly heated billets and the overheated billets could consequently be extruded faster. If the extrusions contain coarse Mg_2Si phase particles, the Mg and Si content tied up in these particles will not be available to form hardening particles during the subsequent ageing procedure and will not contribute to the strengthening of these alloys [13]. The strength of extruded sections from billets that contain coarse Mg_2Si particles will increase by increasing the billet temperatures for billets heated directly to the extrusion temperature due to the dissolution of these particles.

At low cooling rates from the homogenization temperature, Al-Mg-Si alloys contain large Mg_2Si phase particles which will cause melting to occur at low temperatures during extrusion [13]. These particles will need extensive time to dissolve during preheating. However, by increasing cooling rates, the size of these Mg_2Si particles is reduced. Thus, these smaller particles will dissolve at lower billet preheating temperatures, and the shift in extrusion speed is consequently occurring at lower billet temperatures. If the cooling rate is high enough, precipitation of harmful Mg_2Si precipitates is avoided [13]. Billets exposed for such cooling rates can be extruded at high speeds regardless of the variation in billet preheating temperature, i.e. with no shift in extrusion speeds at low preheating temperatures.

2.3. Age hardening

2.3.1. Microstructural development

Age hardening, also called precipitation hardening, provides one of the most widely used mechanisms for the strengthening of metal alloys, including most structural alloys of aluminium, magnesium, nickel and titanium, and some stainless steels. The function of the heat treatment is to make a material obtain desired mechanical properties for a certain application [3]. Alloys that respond to strengthening by heat treatment are called age-hardenable alloys and have a strong decrease in solubility of alloying elements with decreasing temperature so that a large supersaturation is obtained at quenching from the single phase region into the two-phase region [8]. These alloys are characterized by a phase diagram such as the Al-Cu alloys which will be used as an example throughout this chapter. A section of the Al-Cu phase diagram is schematically sketched in Figure 2.6 [16].

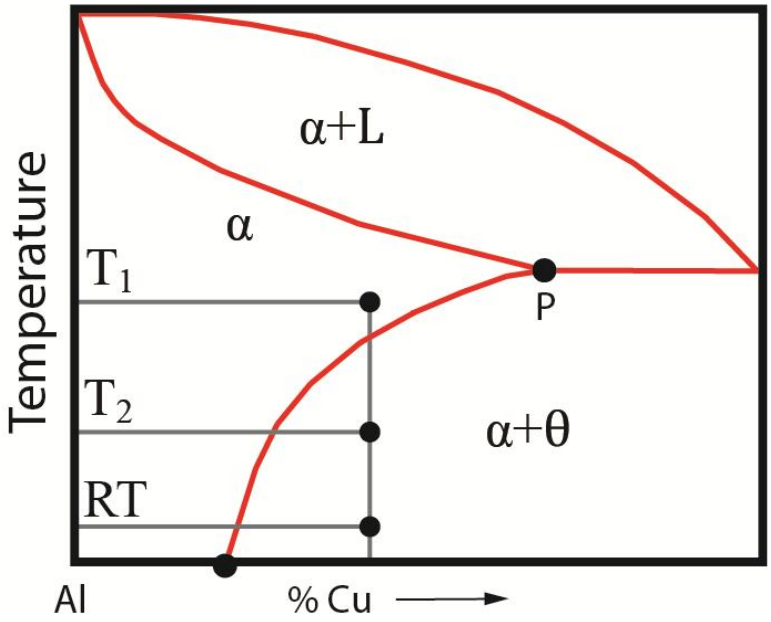

Figure 2.6: A section of the phase diagram for Al-Cu [16]

By introducing lattice defects which provide obstacles to dislocation motion, metal alloys are generally strengthened [8]. Precipitates act like such obstacles. Strengthening of alloys by precipitation hardening consists of the three stages; solution heat treatment, quenching and ageing [3]. Solution heat treatment involves heating the alloy above the solvus temperature (T_1 in Figure 2.6) so that all the components are taken into solid solution (i.e. single phase) [9], and to get a high concentration of vacancies. However, it is important that alloys are not

heated above the eutectic temperature which will cause overheating, i.e. liquation of compounds and grain boundary regions with a following adverse effect on ductility among others [3]. Unnecessary high temperatures and excessively long solution treatment times are also to be avoided in solution treatment of hot worked products to prevent growth of course, recrystallized grains. This is especially important for extrusions. After the solution treatment, the alloy must be quenched rapidly as illustrated in the general temperature profile in Figure 2.7 [17], usually to room temperature (RT in Figure 2.6) which is in the two-phase region to prevent precipitation of alloying elements. A similar profile can be seen in the right part of Figure 2.5 in Chapter 2.2.2.

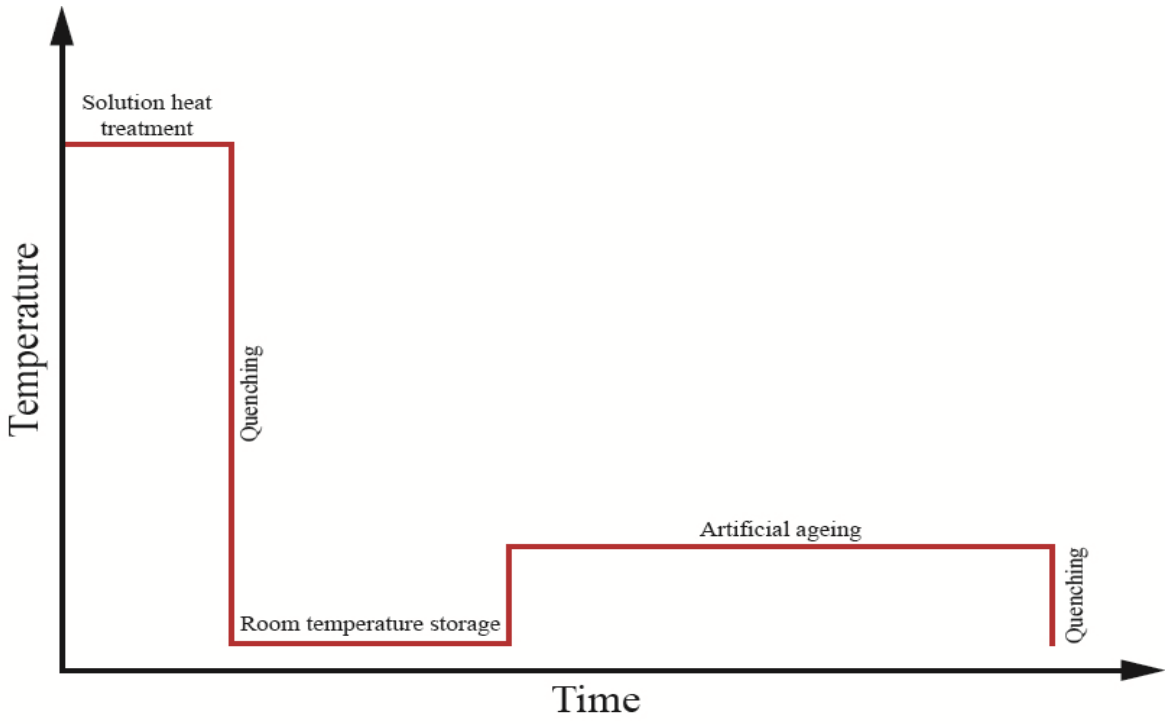

Figure 2.7: General temperature profile during age hardening [17]

This is done to achieve a maximum supersaturation of alloying elements and vacancies prior to the ageing. Cold water is a very good quenching medium which gives sufficient cooling rates for thicker samples [3]. Ageing is the final stage where finely dispersed precipitates form. Room temperature storage now follows which affects the final microstructure and has a negative effect upon the hardness even though no precipitation occurs [18]. However, some alloys undergo ageing at room temperature which is called natural ageing, but most alloys require heating at more elevated temperatures below the solvus temperature (T_2 in Figure 2.6) for precipitation to happen which is known as artificial ageing [3].

During ageing the excess vacancies will diffuse into clusters [8]. At the same time the supersaturated alloying elements will diffuse through the excess of vacancies towards the clusters and condensate on them (for artificial ageing, the precipitation is faster due to increased diffusion). This gives formation of Guinier-Preston (GP) zones which are solute-rich groups of atoms that may be only one or two atom planes in thickness. GP-zones are fully coherent with the matrix and therefore have a very low interfacial energy [16]. In addition, the zones minimize their strain energy by adopting a certain orientation in relation to the host matrix. Despite the fact that the driving force for precipitation of GP zones is less than for the equilibrium phase, the barrier to nucleation is still less, and the zones nucleate most rapidly. Because the alloying atoms have a different size than the host atoms, elastic lattice strain effects arise and extra stress is required to force dislocations through the coherent zones [19]. This gives a contribution to the hardening and the material gets harder. The formation of GP-zones is usually followed by the precipitation of so-called metastable transition phases. In the case of Al-Cu alloys the equilibrium θ-phase is preceded by θ'' and θ'. These form because the free energy for these phases is lower than for the GP zones as illustrated by the molar free energy diagram in Figure 2.8 [19].

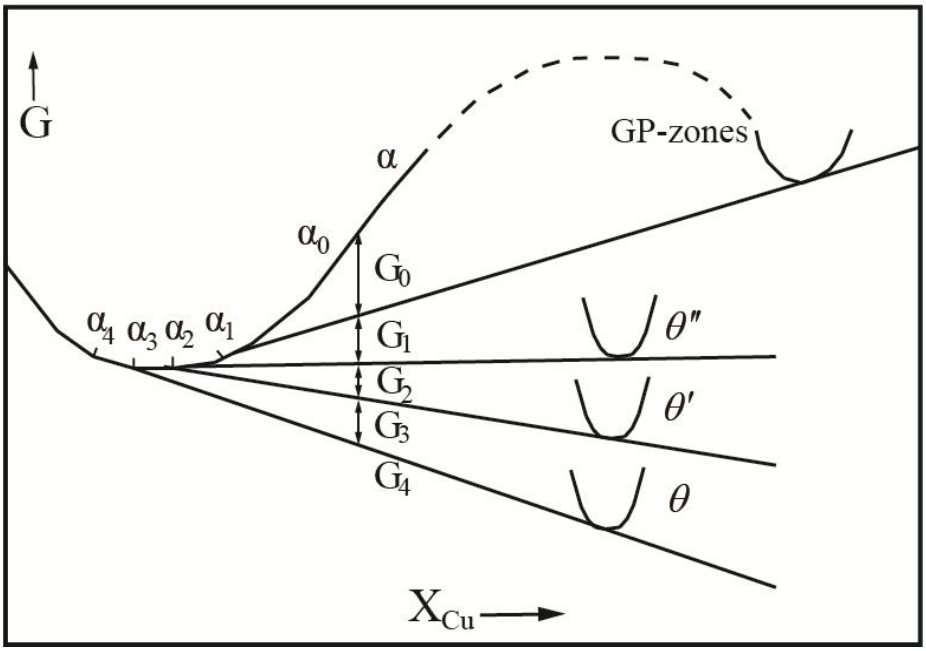

Figure 2.8: Molar free energy diagram for the Al-Cu system [19]

The total precipitation process for this system can be written as given in Equation 2.1 [19].

$$\alpha_0 \rightarrow \alpha_1 + GP - zones \rightarrow \alpha_2 + \theta'' \rightarrow \alpha_3 + \theta' \rightarrow \alpha_4 + \theta \qquad (2.1)$$

Here α_0 is the original supersaturated solid solution, α_1 is the composition of the matrix in equilibrium with GP zones, and α_2 is the composition in equilibrium with θ", etc. G_0 to G_4 are the corresponding free energies for each precipitation sequence. But still the equilibrium phase will not be formed because, like GP-zones, the transition phases have a lower activation energy barrier for nucleation. This is illustrated in Figures 2.9 (a) and (b) for the Al-Cu system where one may observe that the activation energy barrier (ΔG*) to the formation of each transition phase is very small in comparison to the energy barrier against the direct precipitation of the equilibrium phase [19].

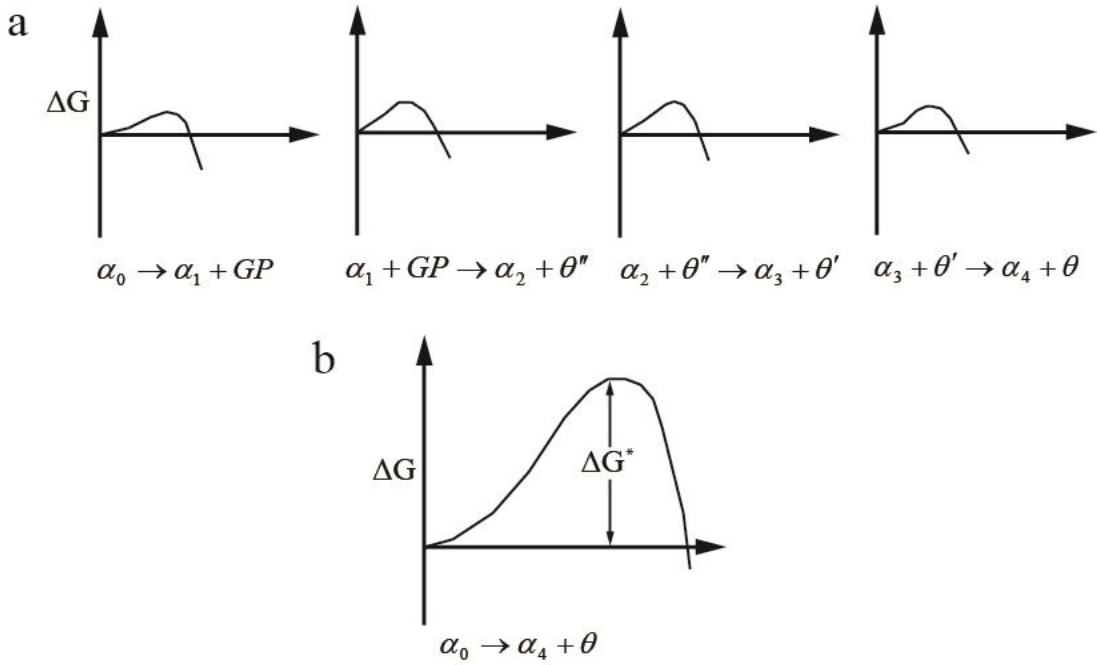

Figure 2.9: Activation barrier for (a) each transition phase and (b) the direct precipitation of equilibrium phase [19]

Lower activation energy barriers are achieved because the crystal structures of these precipitates are intermediate between those of the matrix and the equilibrium phase [19]. In this way, the transition phases can achieve a high degree of coherence and thus a low interfacial energy contribution to the barrier to nucleation. The hardness will increase with the

formation of the first metastable precipitate as the GP zones disappear, and will reach a maximum hardness due to the θ" phase [8]. At longer ageing times, the hardness is observed to decrease when the θ' precipitates are formed. In addition, the precipitates start to diffuse towards one another and agglomerate which give coarsening, reducing the overall number of precipitates and the material strength [17]. This is known as overageing and is illustrated in Figure 2.10 for the Al-Cu system where hardness is given as a function of ageing time [17]. The transformation stops when the minimum free energy equilibrium state is reached [19].

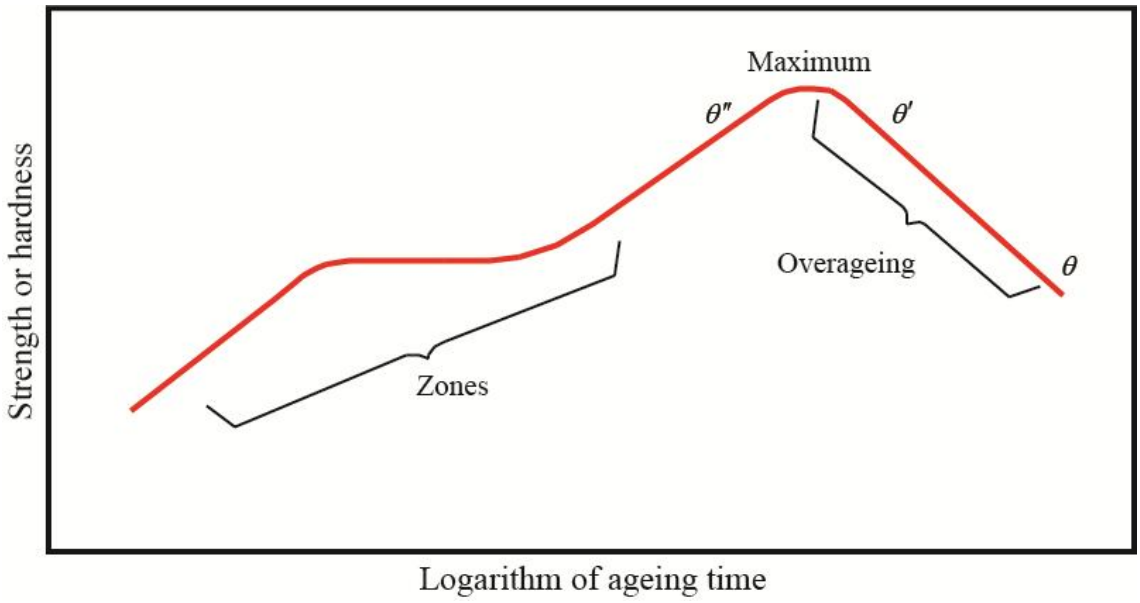

Figure 2.10: Development of hardness as function of ageing time [17]

However, if the temperature is too high, the first precipitates in the precipitation sequence may not form [20]. This is because the heat then is energetically high enough to momentarily overcome the activation barrier of, for instance, the first type of precipitate in the sequence. And since the second precipitates have a lower free energy than the first precipitates, the formation of the first ones are suppressed. This can be illustrated in Figure 2.11 which shows the Al-rich end of the Al-Cu phase diagram [19].

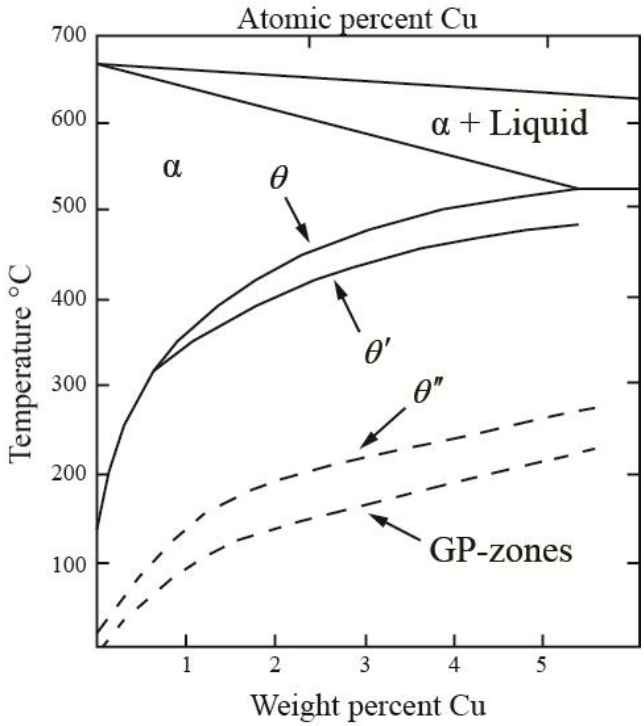

Figure 2.11: Solvus lines for different precipitates in the Al-Cu system [19]

Consider an alloy with the composition Al-4 wt% Cu which is solution heat treated and quenched to room temperature. The solid solution is now supersaturated with Cu. By artificially ageing this at 300 °C, it can be seen from Figure 2.11 that the first precipitates to nucleate is not GP-zones, but θ" [19].

2.3.2. Strengthening processes

Both particles and incoherent precipitates increase the strength with decreasing particle spacing, which in turn decreases with decreasing particle size (r) and increasing volume fraction of precipitates (f_p) [21]. Thus, the strength (τ) is basically a function of size and volume fraction of the precipitates as given in Equation 2.2 [21]. These quantities are further related to the number density which is defined as the number of precipitates per given volume [4]. Since the number density increase with decreasing particle size and increasing volume fraction, the strength increase with increasing number density.

$$\tau = f\left(f_p / r\right) \tag{2.2}$$

Generally, the strengthening which results from age hardening depends on the nature of the precipitates formed. Three mechanisms can be identified, namely coherency strain hardening,

chemical hardening and dispersion hardening [9]. Coherency strain hardening, illustrated in Figure 2.12 (a) [19], is resistance to dislocation motion provided by coherency strain fields which are formed because of lattice mismatch between the aluminium matrix and the precipitates, here represented by α and β, respectively [8]. This contribution will depend on the number and the spacing of the zones or precipitates, and also on the degree of strain produced by each. Maximum hardness is expected when the average spacing between precipitates is similar to the limiting radius of dislocation curvature [3].

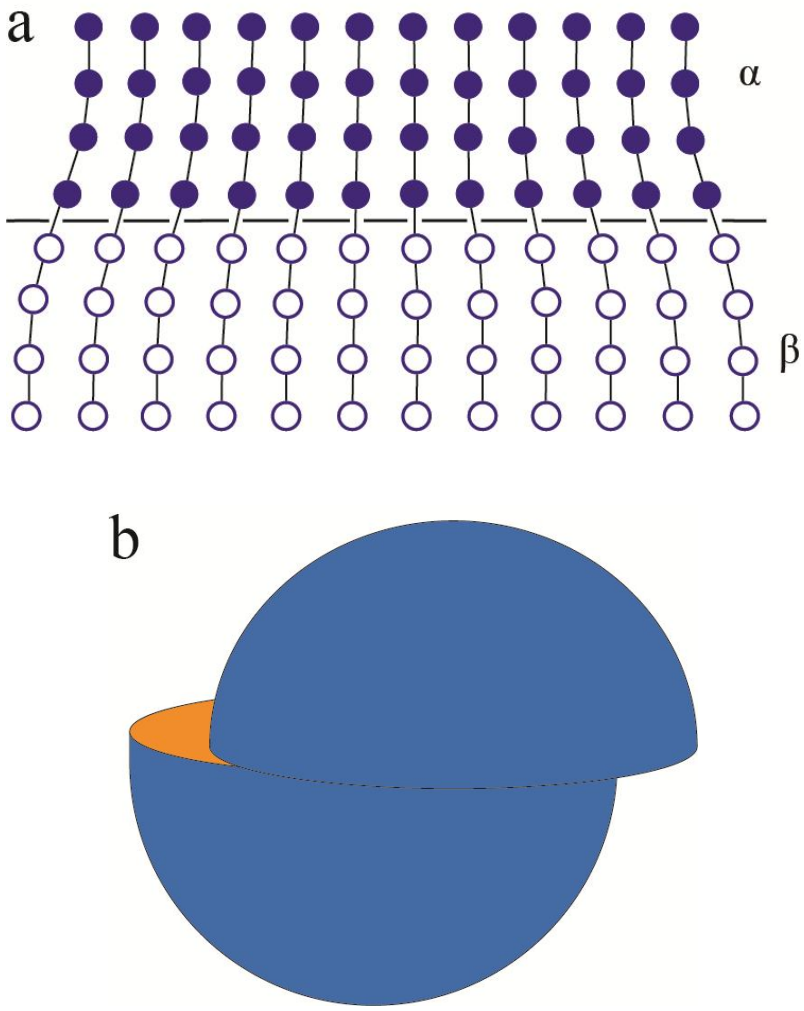

Figure 2.12: (a) Coherency strain hardening [19] and (b) chemical hardening [9]

The increase in stress required to force a dislocation through a coherent zone/precipitate, is termed chemical hardening and is illustrated in Figure 2.12 (b) [9]. This is due to three possible causes: the energy required to increase the precipitate/matrix interfacial area, the energy required to create an anti-phase boundary (APB) in an ordered precipitate, and the change in separation distance of dissociated dislocations due to differing stacking fault

energies. At around maximum hardness, the precipitates also change from being shearable to non-shearable, i.e. moving dislocations during deformation changing their passing of precipitates from cutting (shearing) to looping/bowing [3]. This is illustrated in Figure 2.13 [22].

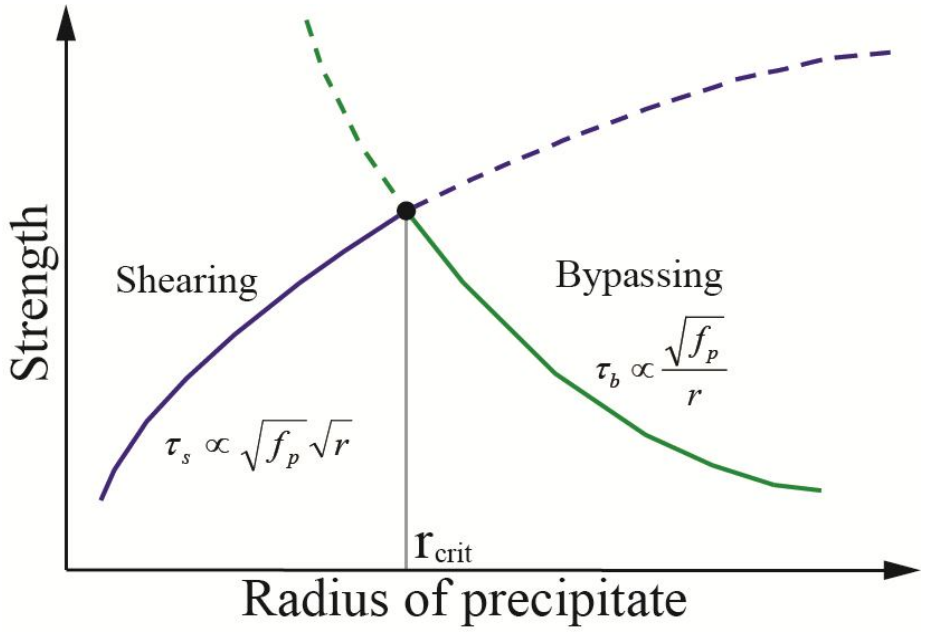

Figure 2.13: Strength from bowing and cutting [22]

The shear stress and the bypassing stress are related to the volume fraction and the radius of the precipitates by Equations 2.3 and 2.4, respectively [22].

$$\tau_s \sim \gamma_s^{3/2} \sqrt{f_p}\sqrt{r} \tag{2.3}$$

$$\tau_b = Gb_l \frac{\sqrt{f_p}}{r} \tag{2.4}$$

Here G is the shear modulus, b_l is the burgers length and γ_s the surface energy of the precipitate. It can be seen that cutting will dominate at a small precipitate radius, while at a large radius bowing will dominate. The change from cutting to bowing occurs because at higher ageing times and/or temperatures, the precipitates become large and incoherent, and the dislocations are no longer able to cut through them [9]. Instead, they undergo a third

strengthening mechanism, namely dispersion hardening. This means that the dislocations must by-pass the precipitates by one of a number of possible mechanisms, including Orowan looping, climbing and cross-slip. These mechanisms are illustrated in Figures 2.14 (a)-(c), respectively [9].

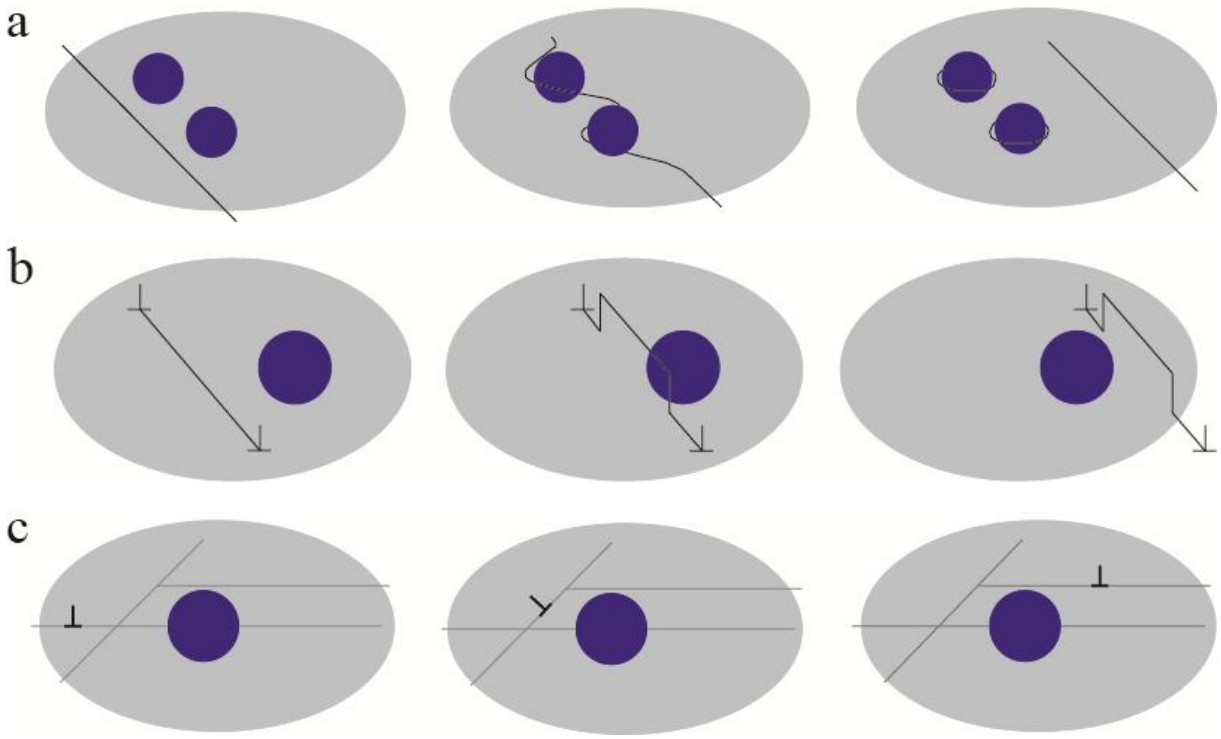

Figure 2.14: (a) Orowan looping, (b) climbing and (c) cross-slip [9]

Orowan looping is a phenomenon where a moving dislocation bows out between the precipitates and rejoin after the by-passing, leaving loops of dislocation around the precipitates [3]. This type of internal dislocation source is known as the Frank-Read source [21]. The precipitates may also be passed by climbing where the dislocation moves perpendicular to its glide plane in planes that do not contain its burgers vector [23]. This is valid for edge dislocations. Under such conditions, atoms have to be added or removed at the dislocation core by a diffusion process that usually takes place only at high temperatures. The last mechanism is cross-slip, which is important at high temperatures, where the dislocation slip from one slip plane to another intersecting plane which contains the same burgers vector [24]. This mechanism is relevant for screw dislocations because these do not have defined glide planes and thus can change their glide planes which is referred to as cross-slip [21].

2.3.3. AA6xxx alloys

For Al-Mg-Si alloys the precipitation stages during artificial ageing is known to be as given by Equation 2.5 [25].

$$SSSS \rightarrow atomic\ clusters \rightarrow GP-zones \rightarrow \beta'' \rightarrow \beta', \text{ U1, U2, B}' \rightarrow \beta \qquad (2.5)$$

Here SSSS is the supersaturated solid solution obtained when quenching from a high temperature during solid solution heat treatment to room temperature, while β', U1, U2 and B´ are the metastable post-β" precipitates which form after β" [12]. During ageing, transformation from β" to β' precipitates may go through the formation of disordered precipitates, and β' precipitates may be further transformed into U1, U2 and B' precipitates [20]. The nature of the precipitation sequence during artificial ageing is very much dependent on three factors: the composition (especially the amount of Mg and Si), the storage time at room temperature and the ageing temperature [4]. The GP zones might be small spheres of magnesium and silicon, and partly consist of coherent needles along the <100> directions in aluminium [8]. β" is made of semicoherent needles, and maximum hardness and strength is generally obtained by this precipitate [10]. The composition of this phase has been found to be Mg_5Si_6 [10]. β' is made of needles with the composition $Mg_{1,8}Si$ [26], U1 consists of $MgAl_2Si_2$ needles [25], and U2 consists of needles made up by MgAlSi [27]. B' on the other hand has a lath shape with a Mg/Si ratio of about 1 [28]. β represents the equilibrium phase Mg_2Si which consists of incoherent, square plates/cubes [6, 25]. Generally, both β" and all the post-β" precipitates are needle or lath shaped precipitates aligned parallel to the <100> aluminium directions [12]. The length distribution of these precipitates tend to be narrow when only one type of precipitate is responsible for the hardening effect, and broad when several are present [29]. In addition, experiments show that long needle precipitates normally have large cross section areas [20]. All the precipitates, except the equilibrium phase (β), are illustrated in Figures 2.15 (a)-(e) [10, 25-28]. The shaded areas represent the image planes while the white circles indicate atoms projected on to the image planes. A full overview of the chemical and structural characteristics of the metastable post-β" precipitates is given in Table D.2 in Appendix D.

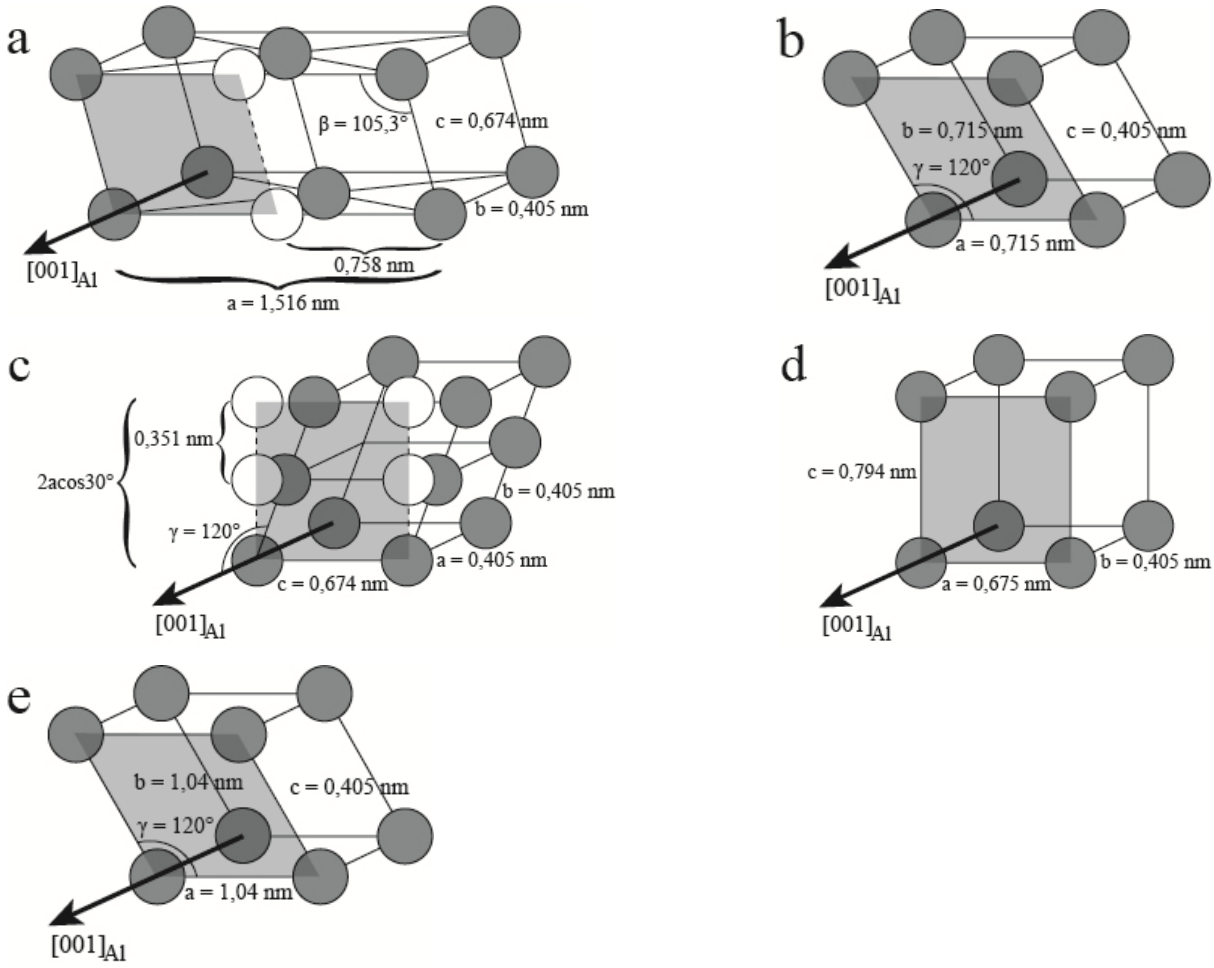

Figure 2.15: Crystal structure of (a) β'' [10], (b) β' [26], (c) U1 [25], (d) U2 [27] and (e) B' [28]

During artificial ageing of the Al-Mg-Si alloys, β" is not necessarily responsible for the maximum hardness condition as illustrated for the Al-Cu system in Figure 2.11 in Chapter 2.3.1. β' (as θ' in Al-Cu) may as an example be the first type of precipitates to be formed and can then theoretically be responsible for maximum hardness because the β" precipitates never were nucleated [19]. However, this value for maximum hardness will be lower than if the β" precipitates were present. In addition, fewer and more course precipitates will be present at higher temperatures which give less strength and lower maximum hardness. The hardening effect of each of the metastable post-β" precipitates are less studied than β", and in commercial alloys the precipitate structure is often a mixture of different precipitates [6]. Therefore, a full explanation of the hardness decrease is not known.

The alloy composition and thermal history determine the final precipitate microstructure of the alloys, i.e., type, size, amount, number density, volume fraction and distribution of precipitates [30]. The room temperature storage prior to artificial ageing may also have a

significant effect on the precipitate microstructure due to formation of atomic clusters [18]. A long storage time commonly produces a coarser final microstructure in Si-rich alloys. For a 6082 alloy at maximum hardness, this results in lower strength. For reduced alloy content or Mg-rich alloys, the situation may be reversed. Since the storage time is constant in the master thesis, this aspect will not be further considered. When it comes to the alloy composition, investigation of six pure Al-Mg-Si alloys artificially aged at 175 °C where the total Mg + Si amount was kept at 1,3 at%, but with different Si/Mg ratios, revealed the influence of the alloy composition on the precipitates [30]. An Si/Mg ratio of 6/5 is an important reference for the composition of the alloys since the composition of β" is Mg_5Si_6 [10]. It was observed that the Si-rich alloys contain a very fine precipitate microstructure giving high hardness (due to GP zones and β" having a near full coherency with the matrix) despite a low volume fraction of precipitates. These Si-rich alloys obtain a sharp hardness peak that can be attributed to GP zones after 3 hours ageing, and this peak rests on a wider peak (~17 hours) corresponding to the β" precipitates [30]. Mg-rich alloys consist mainly of β" and β' precipitates, where the β" precipitates are responsible for strength, and produce a single peak coinciding with the centre of the broad maximum in the Si-rich alloys. These alloys have a coarse microstructure and overage faster than the Si-rich alloys. If the alloy composition is changed from the ideal ratio Si/Mg = 6/5, the β" precipitates display a more disordered atomic arrangement, and an increasing number of other precipitates will also form [30]. For longer ageing times, the U2 phase is common in the Si-rich alloys. The U2 precipitate and a higher stability of β" seem to be the main reasons for the slower overageing observed in the Si-rich alloys. A Si-rich alloy with a lower total content of solutes has a Mg-rich behaviour (it has a coarse microstructure). The Mg-rich alloys contain less U phases, but are richer in β'. It seems like Si controls the number of precipitates by clustering in the beginning of annealing.

2.4. Electrical conductivity

The electrical conductivity of a material is a material's ability to conduct an electric current, and is the reciprocal of electrical resistivity which is a measurement of how strongly a material opposes the flow of electric current [9]. The SI unit of electrical conductivity is Siemens per meter (S/m = 1/Ωm), but is often given in $m/\Omega mm^2$. A good electrical conductor is characterized by a high conductivity and a low resistivity. Values of electrical conductivity are typically reported at 20 °C [31]. This is done because the conductivity of a material is

temperature dependant, and for most materials it decreases as the temperature increases. This dependence is often expressed as shown in the Equation 2.6 where σ represents the conductivity adjusted to the temperature T at which the conductivity value needs to be known. [31]. σ' is the known or measured conductivity, while T´ is the temperature where the known or measured value was obtained. α' is the temperature correction slope which is characteristic for the specific material.

$$\sigma = \frac{\sigma'}{1+\alpha'(T-T')} \tag{2.6}$$

The concept of electric conductivity was presented in the project work, and as a summary, it is observed that the conductivity decrease for short artificial ageing times due to a scattering of the electrons by the small precipitates even though this process leads to removal of solute atoms from solid solution which tends to increase the conductivity [32]. However, experiments show an increase in electrical conductivity for longer ageing times. In addition, the effect of precipitates is negligible at higher ageing temperatures. Therefore, the electrical conductivity decreases for short ageing times before it increases at longer ageing times during precipitation, being a measure of just the kinetics and amount of precipitation.

2.5. Transmission electron microscopy

2.5.1. The microscope

The resolution of an optical microscope is defined as the smallest distance between two details that can be distinguished from one another, and becomes better with decreasing wavelength of the light [33]. A transmission electron microscope (TEM) has a much greater resolving power than an optical microscope because it uses electrons that have wavelengths about 100 000 times shorter than visible light, and can achieve a resolution as small as 0,1 nm [34].

How a TEM is constructed can be seen from the schematic sketch in Figure 2.16 [35]. An electron gun at the top of the microscope emits electrons that travel through the column of the microscope [34]. To avoid spreading of the electrons, there has to be a vacuum in this column. Instead of glass lenses focusing the light as in the light microscope, the TEM uses

electromagnetic lenses to gather the electrons into a very thin focused beam. A condition for all transmission electron microscopy is that the samples have to be so thin that the electrons can be transmitted through the material (we say that they have to be electron-transparent). At an acceleration voltage of 200kV, the maximal specimen thickness is about 1000 nm [34].

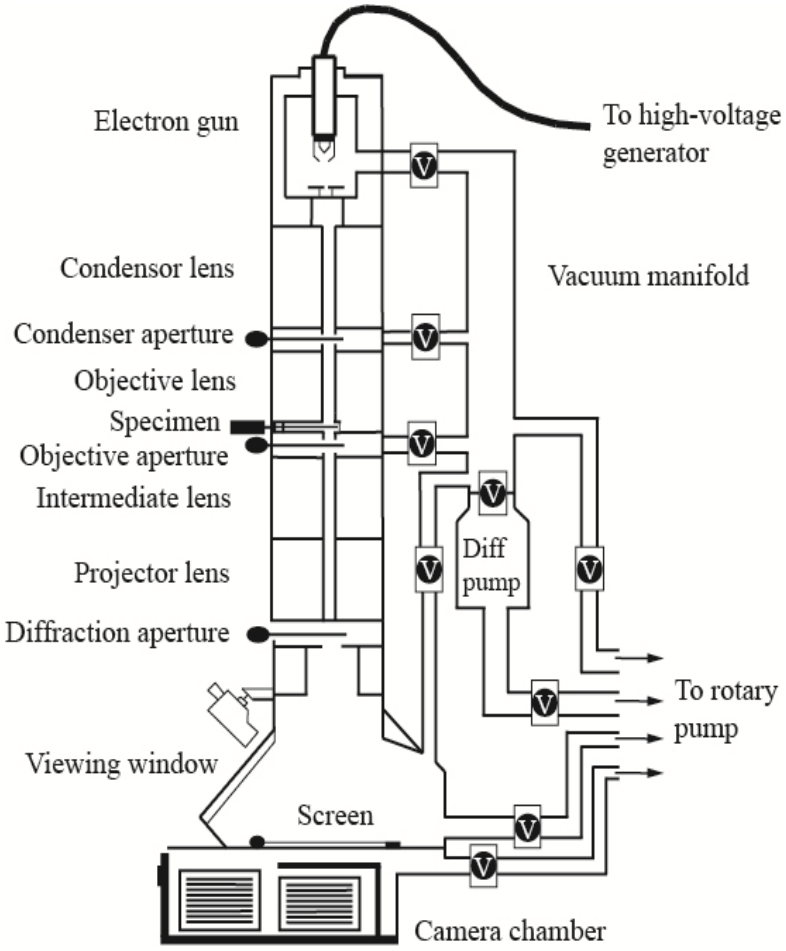

Figure 2.16: Schematic sketch a transmission electron microscope [35]

There are mainly two methods to operate the TEM, namely microscopy and diffraction [34]. The microscopy mode is used to depict the microstructure of the sample. Here the electron beam travels through the specimen you want to study, and depending on the density of the material present, some of the electrons are scattered and disappear from the beam. At the bottom of the microscope, the unscattered electrons hit a fluorescent screen which gives rise to a "shadow image" of the specimen with its different parts displayed in varied darkness according to their density [36]. The image can be studied directly by the operator or photographed with a camera. Good contrast is obtained by inserting an objective aperture into the focal plane of the objective lens [34]. By changing the position of the objective aperture

one may obtain both bright field and dark field imaging. Bright field is obtained when the objective aperture is oriented in such way that the direct electron beam passes through the aperture, while the scattered electrons are stopped. Therefore, grains, defects, particles and other things that causes scattering of the electrons appears dark on a bright background. The bright intensity is high due to the fact that most of the sample is flat so that almost all electrons go through the objective aperture. By moving the objective aperture such that only the scattered electrons pass through it, dark field is obtained [34]. The areas that are responsible for electron scattering will appear bright on a dark background. In analogy to bright field, the bright intensity in dark field images is low. However, this improves the contrast dramatically due to the fact that only the electrons scattered by the sample is collected.

The other method that is normally used is diffraction in the case of crystalline materials where a diffraction pattern is generated [37]. Electrons are scattered in every direction and will interfere constructively or destructively with each other in given directions that depends on the crystal structure and the crystal orientation [34]. As a result, a diffraction pattern is created which can be projected onto a CCD camera (converts light into electrons) [37]. For the single crystal case, the diffraction pattern is dependent upon the orientation of the specimen and the structure of the sample illuminated by the electron beam. This image provides the investigator with information about the space group symmetries in the crystal and the crystal's orientation to the beam path. If one wants to obtain a certain crystal orientation, the diffraction mode in the TEM may be used. As an example, the indexed diffraction patterns for fcc crystals in the [100], [110] and [111] directions are given in Figures 2.17 (a), (b) and (c), respectively [34].

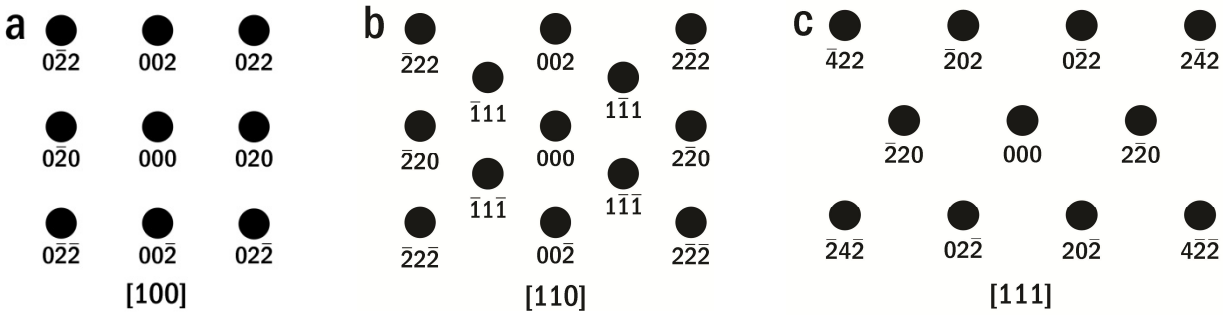

Figure 2.17: Indexed diffraction pattern for fcc crystals in the (a) [100], (b) [110] and (c) [111] direction [34]

It is possible to see the crystallographic structure of a sample at an atomic scale by using an imaging mode called high-resolution transmission electron microscopy (HRTEM) [38]. HRTEM images are formed by removing the objective aperture entirely or by using a very large objective aperture such that not only the transmitted beam, but also the diffracted ones are let through. Thus, a number of diffracted beams are allowed to contribute to the image which is necessary to construct an image of the crystal lattice. This is known as phase-contrast imaging.

Since the needle precipitates in Al-Mg-Si alloys are oriented along the <100> directions in the aluminium matrix, the specimen has to be oriented along one of these directions in order to do the quantification of the precipitates [8]. Due to the fact that the diffraction pattern is dependent upon the orientation of the specimen, it can be used to obtain the correct specimen orientation before taking bright or dark field images. A certain <100> orientation is obtained when the diffraction pattern has units of 2 by 2 atoms that are equally distanced from each other as illustrated by the indexed diffraction pattern for fcc crystals in the [100] direction given in Figure 2.17 (a) [34].

Once a diffraction pattern is obtained in the transmission electron microscope that looks like, for instance, the [100] direction, one can verify that the correct orientation have been obtained by measuring the three distances R1, R2, and R3 as shown in Figure 2.18 [34].

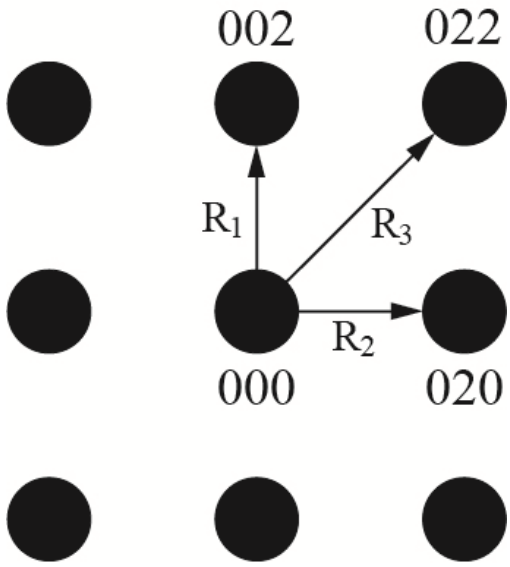

Figure 2.18: Distances in a diffraction pattern [34]

By referring to Figure 2.1 (a) in Chapter 2.1 and use the Pythagorean theorem, one may observe the ratios given in Equations 2.7 and 2.8 [39]. If the three distances measured in the diffraction pattern correlates with Equation 2.7 and 2.8, the correct orientation is obtained, i.e. the [100] direction.

$$\frac{R_2}{R_1} = 1{,}000 \tag{2.7}$$

$$\frac{R_3}{R_1} = 1{,}414 \tag{2.8}$$

If one of the other two diffraction patterns given in Figures 2.17 (b) and (c) is obtained, the kikuchi line map given in Figure 2.19 may be used to find out in what direction one have to tilt the specimen to obtain the [001] direction that is wanted in the master thesis [40]. Other diffraction patterns that are closer to the [001] direction are also indicated.

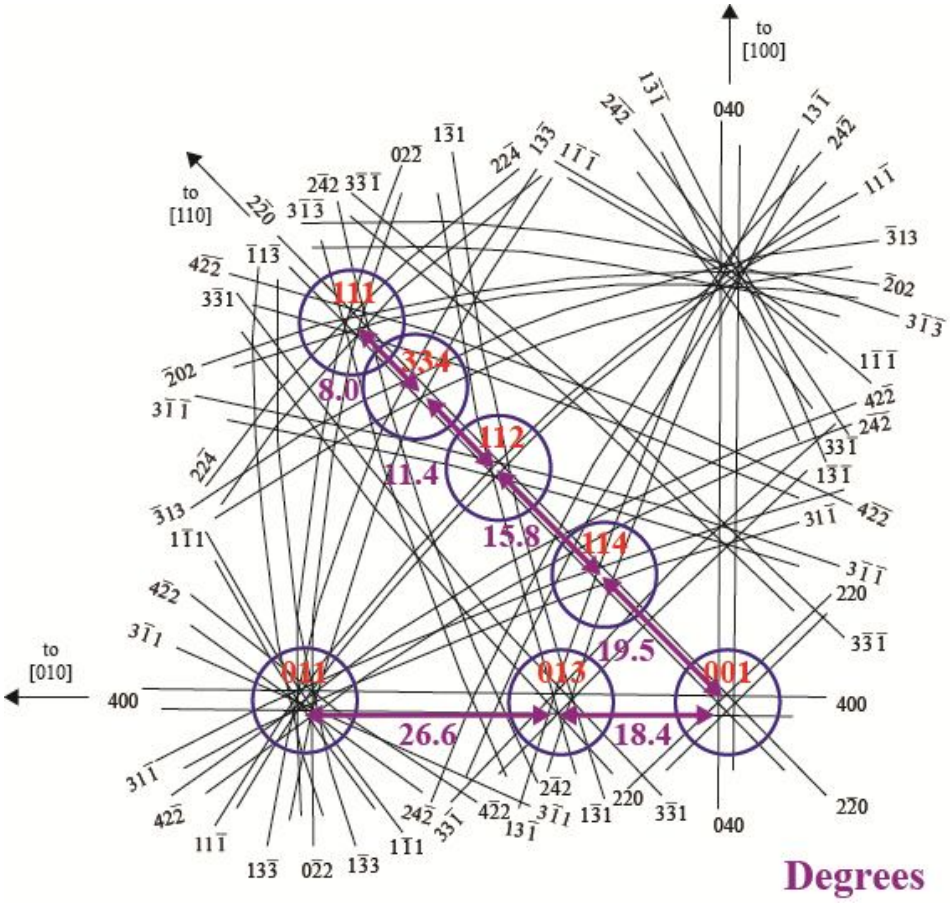

Figure 2.19: Stereographic [001] pole kikuchi line map for diamond fcc crystals [40]

2.5.2. Supplemental TEM methods

The TEM may also be used as a scanning microscope (STEM) or to perform convergence beam diffraction (CBD), chemical analysis with energy dispersive spectroscopy (EDS) and electron energy loss spectroscopy (EELS) among others, given that the relevant detectors are present [34]. In addition, the digital imaging software (if any) is often equipped with several image processing tools like Fast Fourier Transforming (FFT). However, only EELS and FFT will be described further since these are used during the master thesis.

Several transmission electron microscopes are fitted with an electron spectrometer that forms an electron energy-loss spectrum (EELS) from electrons passing through the sample [41]. When travelling through the sample, the electrons may lose energy due to inelastic scattering events [37]. The amount of energy that is transferred from the incident electron to the sample is dependent on the composition and the thickness of the sample. Because the primary beam of electrons has a well-defined energy, the spectrum of the electrons that have passed the sample contains chemical information on the irradiated area. There are three main parts in an energy-loss spectrum, that is zero-loss peak (0 eV), low-loss region (5-50 eV) and high-loss region (> 50 eV) as illustrated in Figure 2.20 [41].

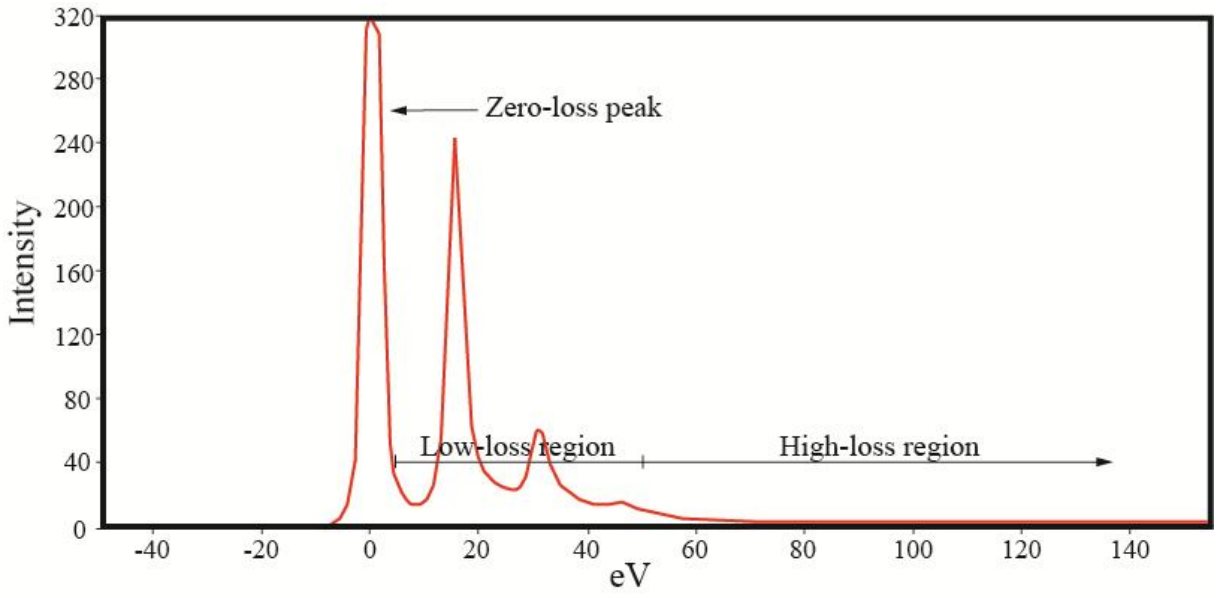

Figure 2.20: A typical electron energy-loss spectrum [41]

The thickness may be computed as a multiple of the inelastic mean free path (MFP) using the log-ratio method given by Equation 2.9, where is the thickness, I_0 is the sum of zero-loss peak counts, I_t is the sum of total spectrum counts (zero-loss peak plus extrapolated loss part), and λ is the inelastic MFP [42].

$$t = \lambda \ln(I_t / I_0) \tag{2.9}$$

Fourier transform is an important digital image processing tool used in a wide range of applications, such as image analysis, image filtering, image reconstruction and image compression, and is used to decompose an image (spatial domain) into its sine and cosine components (frequency domain) [43]. The Discrete Fourier Transform (DFT) is a sampled Fourier transform that does not contain all frequencies forming an image, but only a set of samples which is large enough to fully describe the spatial domain image. The Fast Fourier Transform (FFT) is an efficient implementation of DFT which computes the same result more quickly. Fast Fourier Transforms are widely used in general because applying filters to images in the frequency domain is computationally faster than to do the same in the image domain. An image is filtered by being fourier transformed, multiplied with the filter function that determines the effects of the operator, and then re-transformed into the spatial domain [44]. There are basically three different kinds of filters. A low-pass filter attenuates high frequencies and retains low frequencies which result in smoothing of the image. A high pass filter yields edge enhancement/detection in the spatial domain because edges contain many high frequencies. A band pass filter attenuates both low and high frequencies, but retains a middle range band of frequencies and is used to reduce the noise and enhance the edges at the same time.

2.6. Quantification of needle precipitates

Quantification of precipitates in an AA6xxx alloy may be done in a transmission electron microscope. To get optimum orientation for needle analysis, the aluminium matrix must be oriented along an <100> direction due to the fact that all the precipitates have lengths oriented along the crystallographic <100> directions in as explained in Chapter 2.3.3. An overview of a general sample with its geometrical relations is given Figures 2.21 (a) and (b) [45].

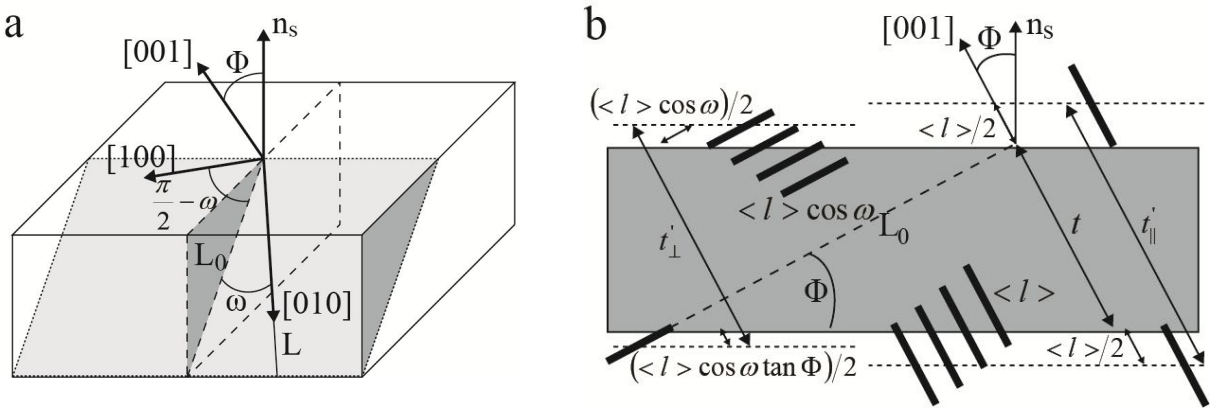

Figure 2.21: General sample with geometrical relations in (a) 3D and (b) 2D [45]

Φ represents the tilt angle in the TEM in order to obtain an <100> direction in the aluminium matrix and shows how the [001] direction is oriented in respect to the surface normal n_s. This is also the viewing direction in the TEM and is a function of the two tilt directions Φ_1 and Φ_2 in the TEM instrument as given in Equation 2.10 [20].

$$\Phi = \arccos\left(\cos\Phi_1 \cos\Phi_2\right) \tag{2.10}$$

In Figures 2.21 (a) and (b), ω is the angle showing how the [100] and the [010] directions in the aluminium matrix are oriented in respect to the specimen geometry, and is often assumed to be close to 45° [45]. Some relations are given in Figures 2.11-2.13 [45].

$$L \parallel [010]Al \tag{2.11}$$

$$L_0 = L\cos\omega \tag{2.12}$$

$$L,\ L_0,\ [100]Al \perp [001]Al \tag{2.13}$$

From Figures 2.21 (a) and (b), one can see that the thickness of the analysed slice is given by Equation 2.14 [45].

$$t = L_0 \tan\Phi \tag{2.14}$$

One may calculate the number density of precipitates ($\rho_{\parallel}$) by counting the number of precipitates over a given image area (A) of a specimen of thickness (t) as given by Equation 2.15 [4, 45].

$$\rho_{\parallel} = \frac{3N_{\parallel}}{V_{\parallel}^{'}} = \frac{3N_{\parallel}}{At_{\parallel}^{'}} = \frac{3N_{\parallel}}{A(t+ < l >_m)} \tag{2.15}$$

The precipitates appear as streaks and dots in the TEM because they are needle or rod shaped and oriented along the <100> directions in the Al-matrix. Only the dots are counted because they are easiest to count, and the number of needles parallel to the [001] direction ($N_{\parallel}$) must therefore be multiplied by 3 [4]. Needles close to the specimen surface have parts that stick out which may be cut during specimen preparation. These would give an underestimation of the average measured needle length and an overestimated number density due to the fact that they belong to a larger volume than that of the analysed specimen foil [45]. In order to correct for precipitates extending out of the foil, the measured average length ($<l>_m$) of the precipitates is added to the specimen thickness which gives a volume correction. The volume fraction of the precipitates (VF) is then given by Equation 2.16 where <CS> is the average cross sectional area of the needles [4].

$$VF = \rho_{\parallel} < CS >< l >_m \tag{2.16}$$

Based on previous observations, it is necessary to introduce error estimations in the average measured needle length in addition to the volume correction due to the cut of the needle parts that stick out of the specimen surface [45]. The estimated error in the average needle length must take into consideration the orientation of the <100> aluminium directions with respect to the viewing direction in the TEM in the same way as for the volume correction. Since both the number density and the volume fraction are functions of the average needle length, there will be errors in these as well. These errors may be found by error propagation. The relative error of the average needle length, the needle number density and both upper and lower limit for the precipitate volume fractions are given in Equations 2.17, 2.18, 2.19 and 2.20, respectively, where the fractions on the left hand side represents the relative errors [45]. Some additional mathematical relations in connection with these equations are given in Appendix F. It can be seen from Equation 2.17 that the error of the average needle length becomes large

for high tilt angles (Φ) and long needles, as compared to the specimen thickness. Due to the error propagation, the relative error of both the number density and the volume fraction also increase for higher tilt angles (Φ) and longer needles. The relative errors of average needle length, number density and volume fraction (upper and lower limit) are given in Equations 2.18-2.20 [45]. Some mathematical derivations and more relations connected to this are given in Appendix F.

$$\frac{\Delta < l >}{< l >} = \frac{< l >_m}{t} \cos\omega \tan\Phi \tag{2.17}$$

$$\frac{\Delta\rho_{\parallel}}{\rho_{\parallel}} = \sqrt{\left(\frac{\Delta V}{V}\right)^2 + \frac{\left(\frac{\Delta < l >}{< l >}\right)^2 + \left(\frac{\Delta t}{t}\right)^2}{\left(1 + \frac{t}{< l >}\right)^2}} \tag{2.18}$$

$$\frac{\Delta VF}{VF} upper = \sqrt{\left(\frac{\Delta < CS >}{< CS >}\right)^2 + \left(\frac{\Delta < l >}{< l >}\right)^2} \tag{2.19}$$

$$\frac{\Delta VF}{VF} lower = \sqrt{\left(\frac{\Delta < CS >}{< CS >}\right)^2 + \left(\frac{\Delta V'_{\parallel}}{V'_{\parallel}}\right)^2} \tag{2.20}$$

3. Previous work

The purpose of this section is to present parts of similar work done by SINTEF reported in *Hardening of Al-Mg-Si alloys and effect of particle structure* [46] and in *Mechanical characteristics of post-β'' precipitates in Al-Mg-Si alloy* [6] which can be used to put the results in the master thesis in a broader context. In addition, a short summary of the project work reported in *Characterization of precipitates at maximum hardness in Al-Mg-Si alloys* [32], will be given which is the basis and starting point for the master thesis. The same materials were analysed in all three studies, but with different conditions in the master thesis. These materials are described in Chapter 3.1. A brief presentation of parts of the two studies done by SINTEF is given together in Chapter 3.2, while a summary of the project work is given in Chapter 3.3.

3.1. Materials

The three alloys, named KK5, KK6 and KK7, used in the project work were made by *SINTEF Materialer og kjemi* [6, 32]. These alloys were direct chill cast into billets with a diameter of 95 mm before they were homogenized at 585 °C for 2 hours (± 15 min). The billets were then extruded into 20 mm rods using an 800 ton instrumented laboratory press. The difference between these three alloys is their chemical compositions which are optimized for certain type of precipitates. The alloy compositions are given in Table 4.1 in Chapter 4.1.1, and the alloy designations which reflects what precipitate(s) the alloys were chemically optimized for are given in Table D.1 in Appendix D along with other chemical facts [6].

3.2. Presentation of similar work done by SINTEF

Several samples were prepared for each alloy in the both SINTEF studies. These were solution heat treated in an air circulation furnace for 1 hour at 540 °C, quenched in water, stored at room temperature for 4 hours and artificially aged in an air circulation furnace to various tempers; 3 hours at 175°C, 10 hours at 175 °C and 3 hours at 260 °C [46]. A part of KK7 was quenched in boiling water after solution heat treatment and artificially aged directly in an air circulation furnace for 3 hours at 260 °C. Figure 3.1 from the report *Hardening of Al-*

Mg-Si alloys and effect of particle structure shows the hardening curves for artificial ageing of the alloys at 175 °C [46].

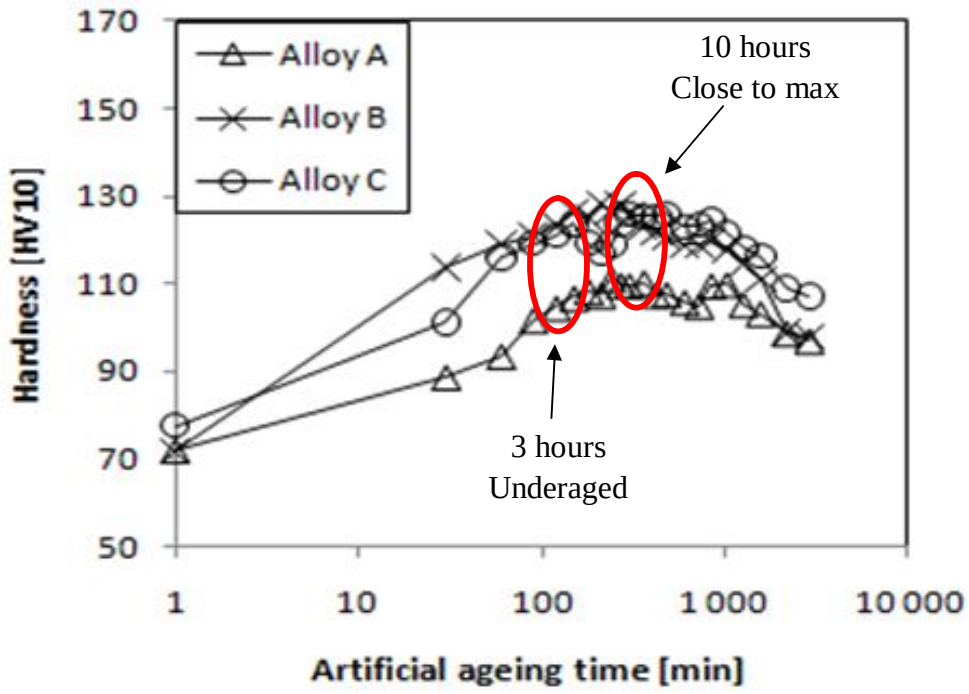

Figure 3.1: Hardness curves for KK5, KK6 and KK7 after artificial ageing at 175 °C [46]

It is observed that artificial ageing for 3 hours at 175 °C corresponds to an underaged condition for all three alloys, while heat treatment for 10 hours results in a condition close to maximum hardness. Both conditions are indicated in Figure 3.1. Artificial ageing at 260 °C for 3 hours resulted in various precipitate structures containing purely post-β" precipitates corresponding to an overaged condition for the three alloys [47].

The three alloys were investigated in a TEM instrument to perform quantitative measurements and to identify the different type of precipitates present. Table 3.1 shows number density, volume fraction, average needle length and cross section area of the needle shaped precipitates, while the type and relative amount of the different precipitates present is given in Table 3.2 [46].

Table 3.1: Measured quantities for KK5, KK6 and KK7 after artificial ageing at 175 °C [46]

Alloy	Artificial ageing [h@°C]	Needle length [nm]	Needle cross section [nm^2]	Number density [µm^{-3}]	Volume fraction [%]
KK5	3@175	47 ± 23.2	7.5 ± 3.2	6 743 ± 986	0.24 ± 0.03
	10@175	83 ± 40.0	18.4 ± 10.1	7 240 ± 913	1.10 ± 0.14
	3@260	253 ± 14.2	247 ± 16.5	213.3 ± 25.8	1.33 ± 0.16
KK6	3@175	37 ± 17.5	7.0 ± 3.0	33 120 ± 4 883	0.85 ± 0.13
	10@175	50 ± 28.3	9.0 ± 5.0	30 767 ± 1 809	1.41 ± 0.08
	3@260	527 ± 20.8	169 ± 80.5	200.7 ± 19.7	1.79 ± 0.18
KK7	3@175	52 ± 43.5	13.1 ± 5.0	10 599 ± 1 838	0.72 ± 0.13
	10@175	64 ± 54.5	15.0 ± 10.8	13 283 ± 1 172	1.28 ± 0.11
	3@260	276 ± 14.7	212 ± 17.6	249.3 ± 24.0	1.46 ± 0.14
	Quenched 100 °C 3@260	329 ± 21.2	247 ± 23.3	223.3 ± 18.5	1.82 ± 0.15

Table 3.2: Precipitates present in KK5, KK6 and KK7 after artificial ageing at 175 °C [46]

Alloy	Artificial ageing [h@°C]	β'' [%]	β' [%]	U2 [%]	U1 [%]	B' [%]
KK5	3@175	76.1	23.9	-	-	-
	10@175	46.6	53.4	-	-	-
	3@260	-	100	-	-	-
KK6	3@175	100	-	-	-	-
	10@175	100	-	-	-	-
	3@260	-	-	25.6	7.1	67.3
KK7	3@175	87.0	13.0		-	-
	10@175	73.9	25.2	0.9	-	-
	3@260	-	26.3	61.5	-	12.2
	Quenched 100 °C 3@260	-	26.5	69.6	-	3.9

The hardness was measured for all these conditions, and Figures 3.2 (a)-(d) show the hardness as a function of volume fraction, number density, cross section area and length of hardening precipitates, respectively [46]. The main type of hardening precipitate of each temper is also indicated. The labels without references in these figures were obtained in [46], while the labels with the reference "[10] " were obtained in [47].

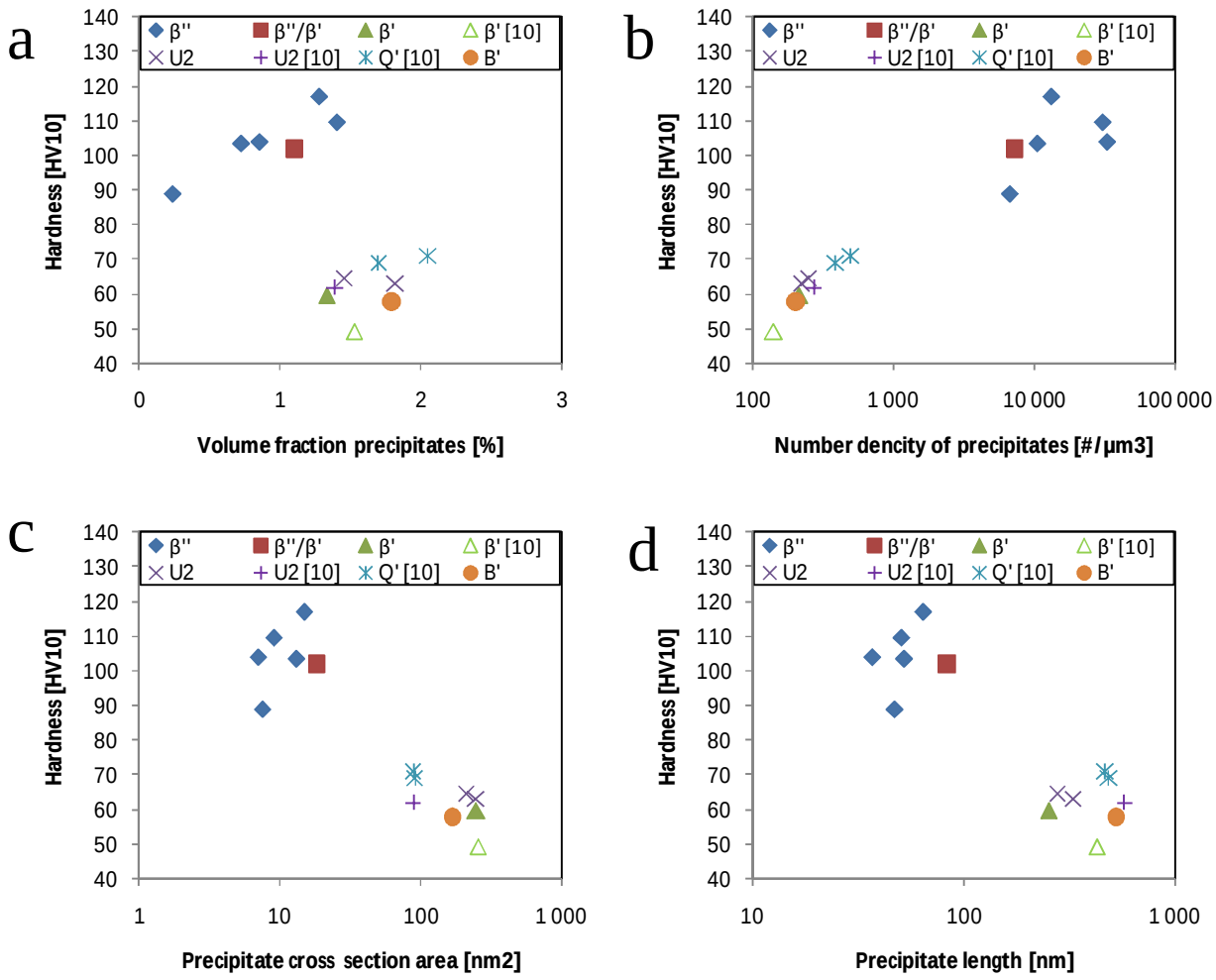

Figure 3.2: Hardness as a function of (a) volume fraction, (b) number density, (c) cross section area and (d) length of the needle precipitates [46]

From Figure 3.2 (a) it is seen that the volume fraction of rod-shaped precipitates in a structure consisting of mainly β" type precipitates increase with increasing hardness [46]. However, when the precipitates are substituted with post-β" precipitates, but still rod-shaped precipitates, this relationship is no longer valid. Figure 3.2 (b), on the other hand, shows almost a linear increment in hardness with the logarithm of the number density of both β" and post-β" type precipitates [46]. A linear decrease in hardness is observed with the logarithm of the precipitate cross section area and length as shown in Figures 3.2 (c) and (d), respectively [46].

All precipitates were considered to be non-shareable and this was confirmed by dislocation loops around precipitates in deformed samples of all temperatures analysed [46]. However, it was not known if the increase in strength from the precipitates is based on a strengthening

model with spherical or rod-like precipitates. The increment in strength from spherical ($\Delta\sigma_s$) and rod-like ($\Delta\sigma_r$) precipitates is given in Equations 3.1 and 3.2 [46]. In these equations, G is the shear modulus of the aluminium matrix (28 GPa), b_v is the Burgers vector in aluminium (0.286 nm), M_T is the Taylor factor (~3.1), ψ is a constant close to 0.5, r_s and f_s are mean precipitate radius and volume fraction of spherical pre-β precipitates, respectively, r_r and r_0 is cross sectional and inner cut-off of radius, respectively, and f_r is the volume fraction of the rod precipitates.

$$\Delta\sigma_s = \frac{M_T}{r_s}(2\varphi Gb)\left(\frac{3f_s}{2\pi}\right)^{1/2} \tag{3.1}$$

$$\Delta\sigma_r = 0{,}075\frac{Gb_v}{r_r}\left[f_r^{1/2} + 1{,}84f_r + 1{,}84f_r^{3/2}\right]\ln\left(\frac{2{,}632r_r}{r_0}\right) \tag{3.2}$$

To find out what model the strengthening is caused by, the relationship between the hardness and Equations 3.1 and 3.2 was plotted. These are given in Figures 3.3 (a) and (b) [46].

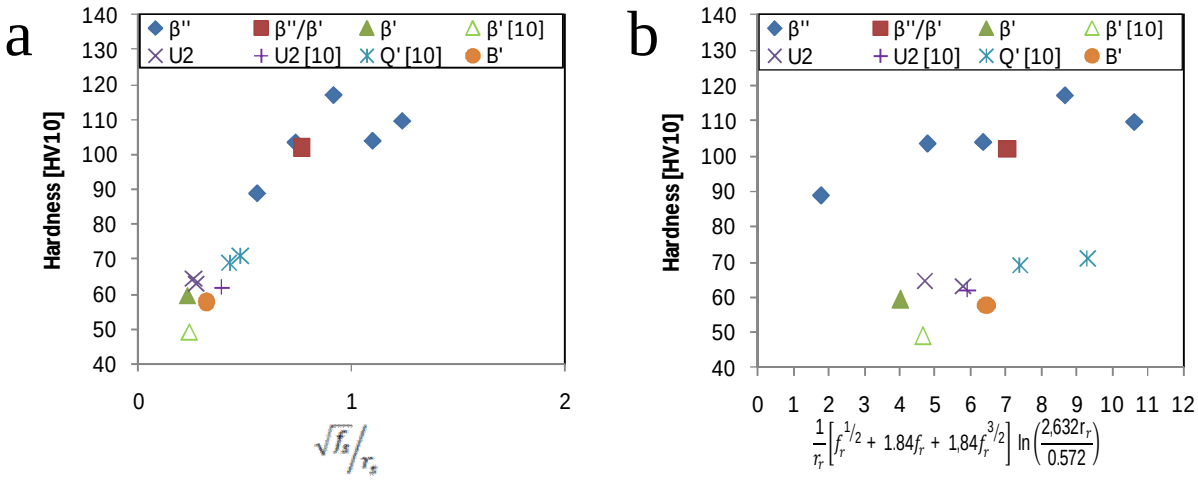

Figure 3.3: Hardness as a function of (a) Equation 3.1 and (b) Equation 3.2 [46]

From Figures 3.3 (a) and (b) it is seen that strengthening model based on spherical precipitates gives a reasonable estimate for strengthening of a wide range of non-shareable rod-shaped precipitates since a linear relationship between hardness and Equation 3.1 is observed [46].

The work reported in [6] is based on the same experimental results as the other report. However, here the annealing condition that produced alloys with as pure precipitate structures as possible were investigated in order to study the mechanical response and hardening effect of each of the post-β" precipitates [6]. The condition chosen was 3 hours of directly artificial ageing in an air circulation furnace at 260 °C as already presented in Table 3.2. The mechanical properties of the alloys are given in Table 3.3 [6]. From these experimental results, it is observed that the alloys containing U2 have somewhat higher strength. It was concluded that the reason for this is that the hardening effect of the β' and U1 precipitates is purely due to their volume fraction in the microstructure because they have no secondary coherency direction. In addition, the discrepancy in periodic distances between the aluminium matrix and $\mathbf{a}_{U2}$ results in a strain field around the U2 precipitates and a corresponding additional hardening, while the discrepancy in periodic distance between the aluminium matrix and $\mathbf{a}_{B'}$ and the lath morphology of the B' precipitates results in a higher additional hardening than the U2 precipitates.

Table 3.3: Mechanical properties for KK5, KK6 and KK7, 3h of artificial ageing at 260 °C [6]

Alloy	Alloy designation	Yield strength [MPa]	Tensile strength [MPa]	Fracture strain [%]	Hardness [HV10]
KK5	β'	124 ± 2.1	187 ± 1.3	18.9 ± 0.55	59.4 ± 0.49
KK6	U1+ B'	118 ± 2.8	182 ± 2.9	18.0 ± 0.36	57.8 ± 1.33
KK7	U2	139 ± 3.4	205 ± 5.0	16.9 ± 0.95	64.6 ± 0.98
	U2Q100	132 ± 2.0	197 ± 3.7	17.3 ± 1.04	63.0 ± 1.10

3.3. Summary of the project work

Similar heat treatments to the ones described in the project work reported in *Characterization of precipitates at maximum hardness in Al-Mg-Si alloys* [32], has already been done at 175 °C by *SINTEF Raufoss Manufacturing AS* as given in Chapter 3.2. However, the temperatures used in the project work were 200 °C and 250 °C, where the precipitation of transition phases were expected to be faster and occur earlier in time due to faster vacancy diffusion [8] and new annealing procedures for both temperatures were suggested. These were tested in an initial screening to be sure of getting useable procedures that gave adequate hardness curves which displayed all relevant variations in hardness as a function of ageing time. The

suggested annealing procedure for artificial ageing at 200 °C was not adjusted, but for the 250 °C case the original suggested time interval was changed because all the three alloys reached overaged conditions very quickly without showing an obvious maximum hardness peak [6]. The suggested annealing procedures are given for both the initial screening and the full procedures in Tables B.1 and B.2 in Appendix B, respectively [32].

Several samples of each alloy were prepared and artificially aged for different ageing times at 200 °C and 250 °C. Vickers hardness and electrical conductivity was measured and plotted as a function of artificial ageing time. The experimental data for these measurements are given in Tables A.1-A.6 in Appendix A, and the obtained graphs are given in Figures 3.4 and 3.5 [32]. The three conditions that are investigated in the master thesis are marked in Figure 3.4 with red circles.

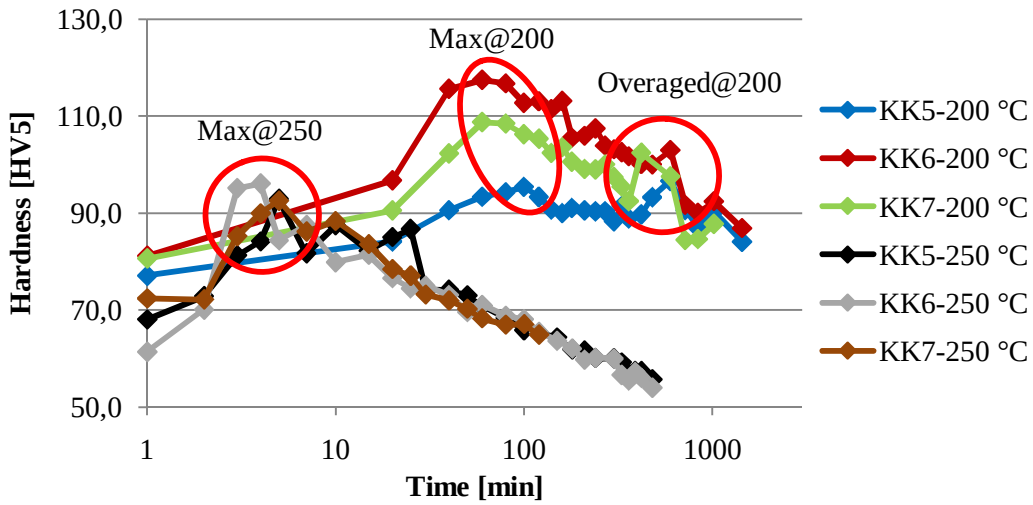

Figure 3.4: Hardness curves for KK5, KK6 and KK7 at 184 °C and 250 °C [32]

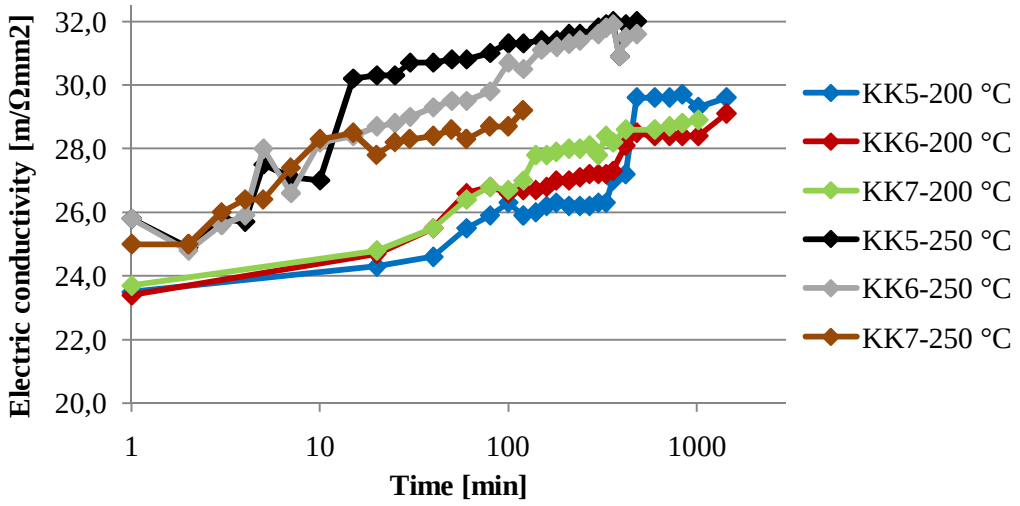

Figure 3.5: Electrical conductivity for KK5, KK6 and KK7 at 200 °C and 250 °C [32]

From Figure 3.4 it is seen that the maximum hardness for the 200 °C case is quite different for the three alloys. A sudden jump in the electrical conductivities, corresponding to maximum condition in the hardness curves, is seen from Figure 3.5. It was concluded that these results indicate that the precipitates present at peak hardness in the three alloys were of different types since the number densities and the volume fractions probably not would give that large hardness differences due to the fact that the ageing temperature was the same and the ageing times, where the maximum appeared, were not significantly different [32]. It is also seen from Figure 3.4 that the obtained maximum hardness values were much lower and occurred way faster for all three alloys that were artificially aged at 250 °C compared to the alloys that were artificially aged at 200 °C. Also here, jumps in the electrical conductivities were observed around the maximum hardness condition which could be seen in Figure 3.5. The conclusion was that the precipitates responsible for maximum hardness at 250 °C most probably were of the same type [32].

4. Experimental

This section describes the experimental work done during the master thesis, and presents the analysed materials and the related experimental methods. Chapter 4.1 gives an overview of the materials that have been investigated and the chemicals that have been used during the experiments. A short survey of the experimental methods and the theory behind them is presented in Chapter 4.2. An overview of the experiments performed is given chronological with the given conditions in Chapter 4.3 while a more detailed experimental procedure is given in Chapter 4.4.

4.1. Materials

4.1.1. KK5, KK6 and KK7

The three alloys, named KK5, KK6 and KK7, investigated in the master thesis are the same materials that were artificially aged to find maximum hardness for all three alloys in the project work *Characterization of precipitates at maximum hardness in Al-Mg-Si alloys* [32]. These alloys were produced by *SINTEF Materialer og kjemi* as described in Chapter 3.1 and were the raw materials handed over at the beginning of the project work last semester.

The difference between the three alloys is their chemical compositions which are optimized for certain precipitate(s). The solute ratio Si/Mg is different for each alloy, but the total amount of Mg and Si is approximately constant. The alloy compositions are given in Table 4.1 [6]. The alloy designations which reflects what precipitate(s) the alloys were chemically optimized for are given in Table D.1 in Appendix D along with other chemical facts [6].

Table 4.1: Composition of KK5, KK6 and KK7 [6]

	Si [at%]	Mg [at%]	Fe [at%]	Mn [at%]	Si + Mg [at%]	Si/Mg [at%]
KK5	0,61	1,0	0,10	0,27	1,54	0,71
KK6	1,12	0,50	0,10	0,27	1,61	2,58
KK7	0,87	0,75	0,10	0,27	1,57	1,34

4.1.2. Used chemicals

Several chemicals were used during the experiments at the laboratory throughout the semester. Some of these represent potential elements of risk. Protecting the hands and the eyes is the best way to stay safe when handling chemicals. The fastest way to get hurt by chemicals is by being unaware of what chemicals that are used. Therefore, it is very important to know what one is working with. For that reason the chemicals used in this work and their properties are listed in Table 4.2 with risk and safety statements [48]. An expletive list with explanations of the relevant risk and safety statements is given in Table E.1 in Appendix E.

Table 4.2: List of materials used in the master thesis with material properties [48]

Name	Molecular formula	CAS number	Appearance	Melting point [°C]	Boiling point [°C]	Specific gravity	Toxicology
Acetone	$(CH_3)_2CO$	67-64-1	Colourless liquid with a fragrant, sweet odour	-95	56	0,79	R11 R23 R36 R66 R67 S9 S16 S26
Ethanol	C_2H_5OH	64-17-5	Colourless liquid	-114	78	0,789	R11 R20 R21 R22 R36 R37 R38 R40 S7 S16 S24 S25 S36 S37 S39 S45
Liquid Nitrogen	N_2	7727-37-9	Colourless odourless liquid at temperatures up to the boiling point	-209,95	-195.86	0.808	S39 S51
Methanol	CH_3OH	67-56-1	Colourless liquid with a characteristic odour	-98	64,7	0,791	R11 R23 R24 R25 R39 S7 S16 S24 S36 S37 S45
Nitric acid	HNO_3	7697-37-2	Colourless liquid with a choking odour	-42	83	1,5	R8 R23 R24 R25 R35 R41 S23 S26 S36 S37 S39 S45
Sulphur hexafluoride	SF_6	2551-62-4	Colourless odourless gas	-63,7	-	5,11	S38

4.2. Experimental methods

4.2.1. Vickers hardness test

Hardness is defined as a material's resistance to localized plastic deformation [11]. Many quantitative techniques have been developed, including Rockwell, Knoop, Brinell and Vickers hardness test, where a small indenter is forced into the surface of the material subjected to testing. Hardness tests are the most common mechanical tests due to the fact that they are simple, inexpensive and non-destructive (the specimens are neither fractured nor excessively deformed). In addition, other mechanical properties such as tensile strength may be estimated from hardness data. There is also a useful approximate relationship between Vickers hardness and yield strength which is widely used, but is not always strictly correct. This relationship states that Vickers hardness is approximately 0,3 times the yield strength in MPa [9]. However, hardness is only relative, so comparing values determined by different techniques should be done carefully.

The Vickers hardness test is a widely used technique which has a small diamond pyramidal indenter as shown in Figure 4.1, that relates directly to Vickers hardness [9].

Figure 4.1: Resulting indentation from a Vickers hardness test [9]

The Vickers hardness is calculated by measuring the two diagonals of the indentation and apply Equation 4.1 where F is the applied load in kg and $\bar{d}$ is the average diagonal in mm [11].

$$HV = \frac{1{,}854 \cdot F}{\overline{d}^{\,2}} \qquad (4.1)$$

Vickers hardness numbers are reported as xxxHVyy where xxx is the hardness number and yy is the load used in kg [11]. Applied loads for both Vickers and Knoop hardness are much smaller than for Rockwell and Brinell, and are referred to as microindentation-testing methods due to the indenter size.

4.2.2. Jet polishing

To investigate a specimen in TEM, its thickness has to be sufficient small enough to let electrons through so the formation of a TEM image is possible [34]. Several techniques are available depending on the specimen nature and quality. Twin jet electrolytic thinning, from now on called jet polishing which is an electrochemical dissolution technique, is one of the methods [49]. The aim of jet polishing is to make a thin, damage-free sample by thinning down a disc until a central hole is obtained. In the area around this hole, the specimen is thin enough to let through electrons so the formation of TEM images is possible. An illustration of this is given in Figure 4.2 [34].

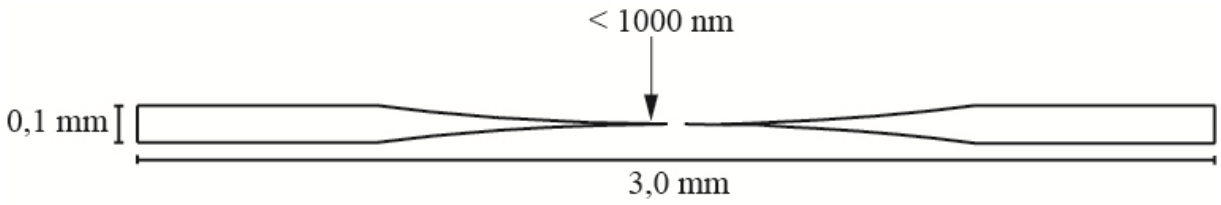

Figure 4.2: Jet polished TEM sample [34]

This is done by electro polishing of a conducting material associated with the hydrodynamic action of two electrolyte jets, one to each side of the specimen [49]. Two dissolution dimples are formed from each side of the specimen and join at its mid thickness to give a perforation. Before the jet polishing, the sample has to be mechanically thinned, usually by grinding and polishing down to about 0,1 mm thickness [34]. The sample is punched out to discs with a diameter of 3 mm. These discs are connected one at the time to the positive pole in a current device and works out as the anode. On each side of the specimen, there is a cathodic plate with holes where a suitable electrolyte is continuously gushing through. Electro polishing of the sample is obtained by adjusting the voltage. The polishing can be automatically stopped

when the perforation is detected by a photocell receiving a light beam emitted from the other side of the object [50]. In the areas around the hole, the specimen thickness is now lower than 1000 nm which is the approximate thickness limit to make imaging in the TEM possible at 200 kV acceleration voltage [34]. After this, the specimen has to be removed from the electrolyte as fast as possible to avoid further etching, and is washed in alcohol. The sample is now ready for investigation in TEM.

4.2.3. Ion beam thinning

Ion beam thinning, also known as ion milling, is a preparation technique used on TEM specimens to reduce the thickness to electron transparency by momentum transfer [51]. To prepare them for microscopy, the samples are first mechanically sectioned and ground before polishing or milling to remove additional material. This method is effective for all materials including those that are relatively nonconductive such as semiconductors and insulators as well as those that are conductive. All types of compact single-phased or multi-phased material can be ion thinned, but porous or divided materials must be impregnated or embedded beforehand [49]. Inert gas, typically argon, is ionized and then accelerated toward the specimen surface as illustrated in Figure 4.3 [51]. Surface atoms at the specimen surface are removed by the interaction of the accelerated ion beam (sputtering). This leads to relief polishing and suppression of the possible mechanical damages introduced during the preparation [49]. Abrasion by the ion beam can be applied to plane longitudinal and cross sections and to wedges. Alternatively, a reactive gas may be used to increase the effective milling rate since its chemical reactivity supplements momentum transfer [51]. Cooling of the samples with liquid nitrogen, known as cold stage ion milling, may be used to eliminate heat-induced artefacts in the samples [52].

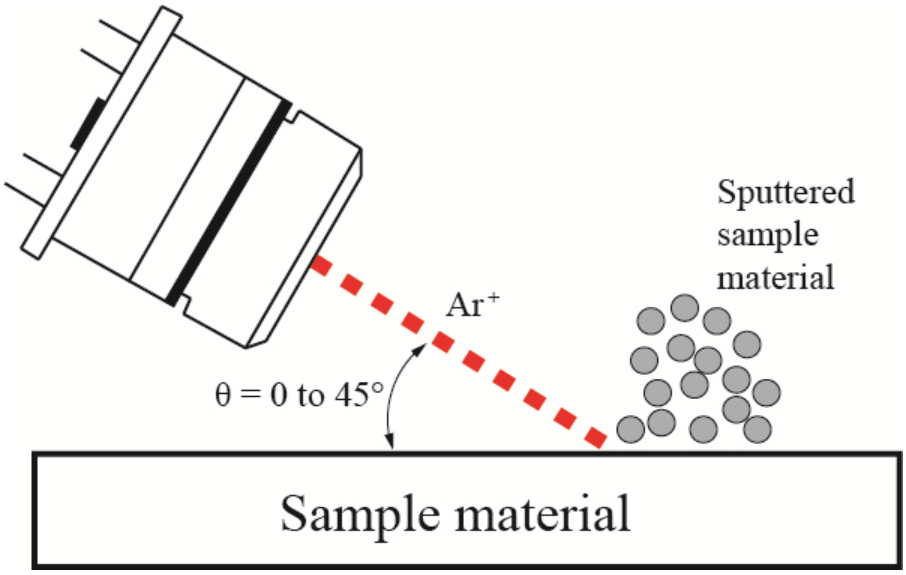

Figure 4.3: The principle of ion beam thinning [51]

The apparatus consists of a chamber operating under secondary vacuum (~10^{-5} Torr) fitted with one or two argon ion guns [49]. The ion beam is accelerated by a potential difference ranging from a few volts to several kV. Generally, a specimen is pre-thinned by mechanical polishing or dimpling before it is placed on its holder and set in motion according to a continuous rotation or to a sector oscillation shielding parts of the specimen from the ion beam. The polishing is done by using a single (sometimes dual) ion beam focused on the desired face or an ion beam on each side of the specimen in order to polish both faces simultaneously. The perforation may be detected either by a photocell or by using an optical microscope. The ion beam incident angle can be adjusted between 0-45° according to the type of apparatus. Low angle milling gives a thin high quality zone over a large width.

The advantages of ion beam thinning is that thinning is obtained with no mechanical damage, irrespective to the material hardness or fragility [49]. It can be applied to mixed-composite materials, and is also adapted to specimens prepared in laminate form. However, the drawbacks are that ion beams may cause radiation and thermal damages such as Ar+ ion implantation, selective etching, chemical diffusion and matter transport from one point to the other of the bombarded surface. These effects may be minimized by cooling down the specimen or by decreasing the incident angle and the ion beam energy.

4.2.4. Plasma cleaning

For imaging and microanalysis in electron microscopy, it is imperative to prepare specimens without altering their microstructure or composition too much [53]. Modern electron microscopes with high brightness electron sources combine a small electron probe for microanalysis with increased beam current density, yielding high resolution images and enhanced analytical data. Unfortunately, current specimen preparation techniques often introduce amorphous damage in addition to contamination. The contamination increases as probe size decreases and beam current density increases, and comes from several sources including inadvertent touching of specimens or specimen holders, back streaming of oil from an oil diffusion pumped ion milling system, electron microscope column contamination, and adhesives or solvents used in the preparation process. Therefore, the quality of the specimen and the cleanliness of both the specimen and the specimen holder are very important.

Plasma cleaning involves the removal of impurities and contaminants from surfaces through the use of energetic plasma created from gaseous species by using high frequency voltages to the gas. Gases such as argon and oxygen as well as mixtures like air and hydrogen/nitrogen are used. However, a mixture of 25% oxygen and 75% argon is generally recommended to optimize the cleaning [53]. The plasma process creates disassociated oxygen which combines chemically and breaks apart high molecular weight surface contaminants. These organic contaminations are reduced to CO, CO_2 and H_2O that are evacuated by the vacuum system. The specimen properties is not altered because the plasma ions impact the surface with energies less than 15 eV [53], an energy level which is below the sputtering threshold for the specimens. Two TEM images of TiN coated Si before and after 30 seconds of plasma etching are given in Figures 4.4 (a) and (b), respectively [53].

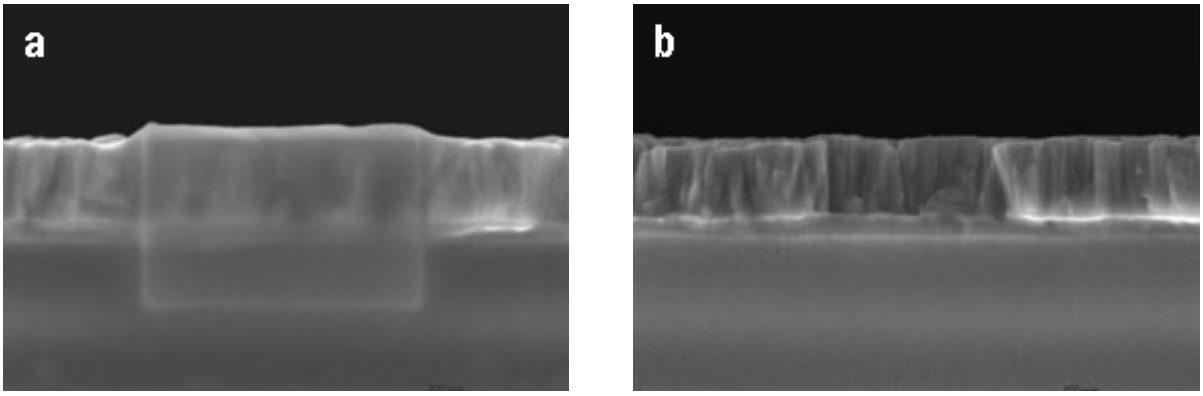

Figure 4.4: TiN coated Si (a) before plasma cleaning and (b) after 30s of plasma cleaning [53]

Prior to plasma cleaning, a proper specimen preparation has to be applied [53]. Techniques such as electro polishing, mechanical pre-thinning and ion milling may be used for TEM samples depending on the material properties. It is also important to consider what type of TEM analysis that is required in order to choose the correct preparation method to obtain optimum results. Plasma cleaning is a final operation before insertion into the electron microscope, and can be applied to most types of materials research specimens.

4.3. Experimental program

4.3.1. Selection of samples for TEM investigation

- Selection of maximum hardness samples from all three alloys and for both artificial ageing temperatures, i.e. six cases in total
- Selection of samples that represents a local maximum at overaged condition for all three alloys for an artificial ageing temperature of 200 °C, and one sample for KK5 that represents an area right before the local maximum, i.e. four cases in total

4.3.2. Preparation of TEM samples

- Cutting of a thin discs from each sample with a Struers Minitom
- Grinding the samples with a Struers Knuth-Rotor down to 1200 grit grinding paper on both sides until ~100 µm thickness
- Punching out several small discs with a diameter of 3 mm from each sample
- Jet polishing with a Struers TenuPol-5 to obtain thin specimen areas (< 1000 nm)
- Cold stage ion milling of all TEM samples
- Plasma cleaning of all TEM samples before insertion in the TEM instruments

4.3.3. TEM analysis

- JEOL JEM-2010: Twenty images for each case with magnifications of 25 000, 30 000 and 40 000, and thickness measurements with EELS
  - Calculation of average needle lengths (<l>)
  - Calculation of needle length distributions
  - Calculation of number densities ($\rho_{\parallel}$)

- Philips CM30: Fourteen to thirty six high resolution images with magnifications of 420 000 and 600 000 (image calibration for images with magnification of 420k)
  - Calculation of average needle cross section areas (<CS>)
  - Calculation of volume fractions (VF)
  - Identification of needle precipitates and their relative amount
- Calculation of relative errors based on images from both transmission electron microscopes

4.3.4. Casting and extrusion of new material

- Direct chill casting of KK5, KK6 and KK7 into billets
- Extrusion of KK5, KK6 and KK7 billets into rods

4.4. Experimental procedures

4.4.1. Selection of samples for TEM investigation

The microstructure at maximum hardness was investigated for all three alloys and for both artificial ageing temperatures, i.e. six cases in total which are marked in Figure 3.4 in Chapter 3.3. The samples that were artificially aged to maximum hardness were picked out by using the obtained hardness measurements from the project work. From Tables A.1-A.3 in Appendix A, sample number 6 for KK5, 4 for KK6 and 4 for KK7 were chosen for the samples that were artificially aged at 200 °C. Likewise, sample number 2 for KK5, 26 for KK6 and 2 for KK7 were chosen for the 250 °C case from Tables A.4-A.6 in Appendix A

The microstructure at local maximum hardness at overaged condition was also investigated for all three alloys artificially aged at 200 °C which are marked in Figure 3.4 in Chapter 3.3. These were investigated by choosing sample number 19 for KK5, 19 for KK6 and 17 for KK7 based on information from Tables A.1-A.3 in Appendix A. Sample number 16 for KK5 was also picked out from Table A.1 in Appendix A. This sample represents an area right before the local maximum hardness peak for KK5 and was used for comparison of the microstructure at the local maximum hardness peaks with the general overaged conditions in order to find out why these local peaks are observed.

4.4.2. Preparation of TEM samples

A thin disc was cut with a Struers Minitom, which is depicted in Figure 4.5 (a), from all the samples that were chosen for TEM analysis. These were grinded down to 1200 grit grinding paper on both sides with a Struers Knuth-Rotor, shown in Figure 4.5 (c), until the samples had a thickness of about 100 µm.

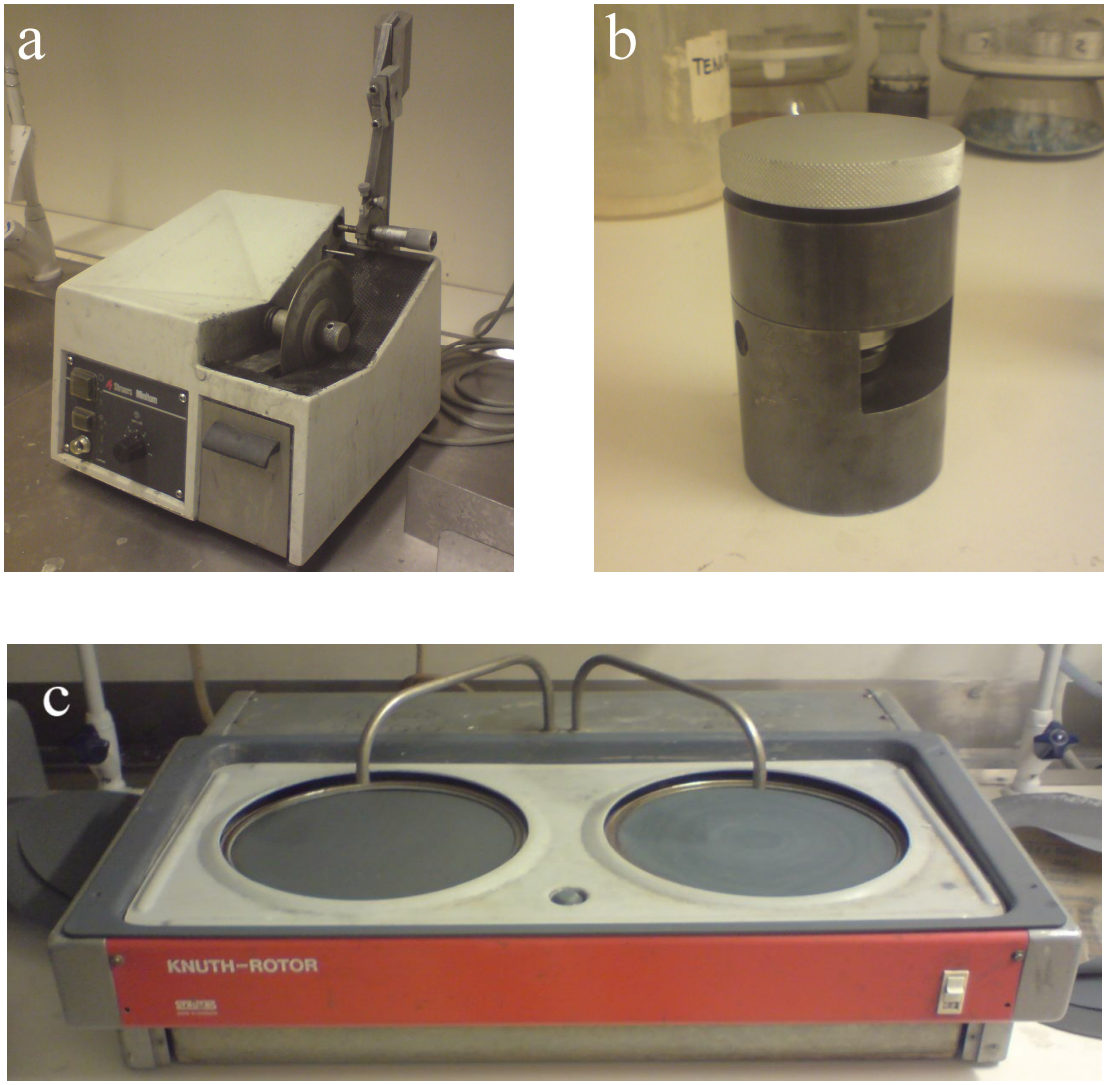

Figure 4.5: (a) Struers Minitom (b) Punching device and (c) Knuth-Rotor

About 20-25 small discs with a diameter of 3 mm were punched out from each of the samples with the punching device shown in Figure 4.5 (b). The discs were put in acetone and placed in an ultrasonic bath for cleaning before they were further thinned by jet polishing with a Struers Tenupol-5, one alloy at the time. An image of the Tenupol-5 is given in Figure 4.6 (a) along with some TEM samples in Figure 4.6 (b). The electrolyte used in the jet polishing was made of one third nitric acid and two-thirds methanol.

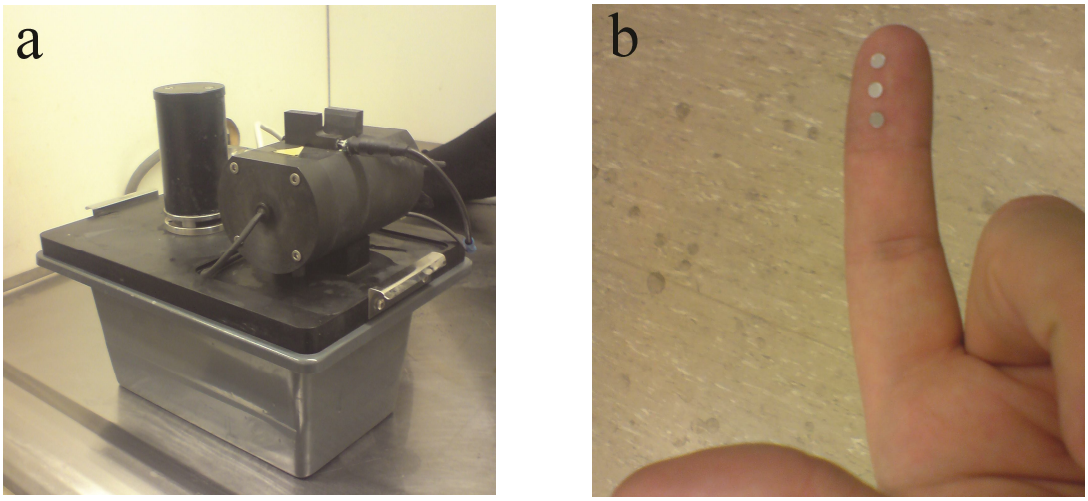

Figure 4.6: (a) Struers Tenupol-5 and (b) TEM samples

All the samples were exposed to cold stage ion milling. The cooling is important because it prevents any further growth and/or transformation of the precipitates during milling if any [29]. They were first ion milled at 3,7 kV for 30 minutes, and then for another 30 minutes at 1,5 kV in a Fischione Model 1010 Ion Mill pictured in Figure 4.7 (a). This was done to make even larger and thinner electron transparent areas in the specimens. These parameters were used because they have been utilized by a PhD candidate [54] for exactly the same type of materials and are known to give the TEM samples a very good finish. Before the samples were inserted in the transmission electron microscope, they were cleaned for 10 minutes [53] with a Fischione Model 1020 Plasma Cleaner depicted in Figure 4.7 (b). This was done to remove organic contamination from the specimen holder as well as the specimens themselves.

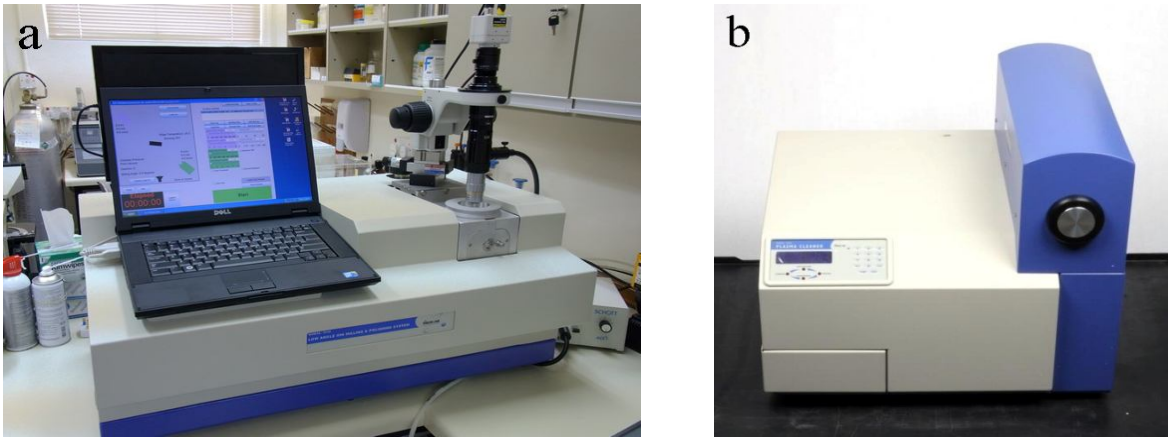

Figure 4.7: (a) Fischione Model 1010 Ion Mill and (b) Fischione Model 1020 Plasma Cleaner

4.4.3. TEM analysis

The samples were investigated in two different TEM instruments. Twenty digital bright field images were taken with JEOL JEM-2010 at Department of Materials Science and Engineering, shown in Figure 4.8, at a magnification of 25 000 and 30 000, from now on referred to as 25k and 30k. These images were used to calculate average length (<l>), length distribution and number density ($\rho_{\parallel}$) of the needle precipitates. Several needle lengths parallel to the [100] and [010] directions in the aluminium matrix were measured in order to calculate the average length and the length distribution of the needles. The number density was calculated by counting the number of needles parallel to the [001] direction ($N_{\parallel}$) over the area represented by each image and use Equation 2.15 in Chapter 2.6. Before the images were analysed, their contrast were improved by using Fast Fourier Transform in the imaging software DigitalMicrograph. The thickness of the specimens, which is used in the needle quantification, was measured for each of these twenty images by using electron energy loss spectroscopy (EELS) which is another function in DigitalMicrograph.

Figure 4.8: JEOL JEM-2010 Transmission Electron Microscope

Depending on the number density, fourteen to thirty six high resolution bright field images were taken on film of needle cross section areas with Philips CM30 at Department of Physics, shown in Figure 4.9, at a magnification of 420 000 and 600 000 or from now on referred to as 420k and 600k. These were used to measure the average cross section area (<CS>) and to calculate the volume fraction of the precipitates (VF) according to Equation 2.16 in Chapter 2.6. Identification of the precipitates was also done with these images by zooming in on the precipitates oriented in the [001] direction, and comparing their crystal structure with earlier findings as given in Figure 2.15 in Chapter 2.3.3. Number densities, average cross section areas and volume fractions were also calculated for each type of precipitates present at the given conditions.

Figure 4.9: Philips CM30 Transmission Electron Microscope

In order to measure cross section areas so that volume fractions could be calculated, scale bars had to be added. These were added automatically to the digital images taken with JEOL JEM-2010 by the imaging software DigitalMicrograph. The film images taken with Philips CM30 at a magnification of 420k on the other hand, had to be calibrated in the same program before manual addition of scale bars. This was done by scanning the films into tiff images before

marking distances between atoms in the identified precipitates and inserting the correct lattice parameters known from the literature. Twenty-four images were calibrated and one scale factor was calculated for each image. These were then used to calculate an average scale factor (nm/mm) which was used to draw a common scale bar for all the scanned film images taken at CM30 at 420k magnification. The image calibration resulted in a small dataset as given in Table A.24 in Appendix A. An average scale factor for all the scanned CM30 film images taken at 420k magnification was calculated to be 0,9194 nm/mm after printing them out in regular A4 format. The images taken at 600k magnification did not have to be calibrated because the real magnification for these images was known to be 491,8k [29].

Relative errors were estimated for all the key numbers for the overall analysis to have a survey of all sources of error and their magnitudes. Relative error in the average measured needle length was estimated by using Equation 2.17 in Chapter 2.6. Due to error propagation, the relative error for the needle number density and the volume fraction (both upper and lower limit) were also estimated according to Equations 2.18-2.20, respectively. The relative errors for all the alloys and ageing conditions are given in Table A.25 in Appendix A.

4.4.4. Casting and extrusion of new material

New raw material (rods of KK5, KK6 and KK7) were made for other participants at the KK project from both Department of Materials Science and Engineering, and Department of Physics. The three alloys were direct chill cast in a laboratory furnace into three billets of each alloy with a diameter of 95 mm. The billets were homogenized at 585 °C for 2 hours (± 15 min) and extruded into 20 mm rods using an 800 ton instrumented laboratory press at SINTEF.

All the billets were extruded successively which means that some parts of the extruded rods had to be cut away due to formation of charge welds. These parts were cut away to obtain pure KK5, KK6 and KK7 rods for investigation in the case of extruding of different materials successively, and to avoid influence on mechanical properties in general due to the fact that charge welds decrease the ductility of the alloys. Figure 4.10 is an image of one of the scraps after it has been cut alongside with the extrusion direction. This scrap represents the bonding area between the first extruded KK5 alloys and an unknown aluminium alloy that was extruded by someone else earlier that day. Here the charge weld can easily be seen at the right hand side.

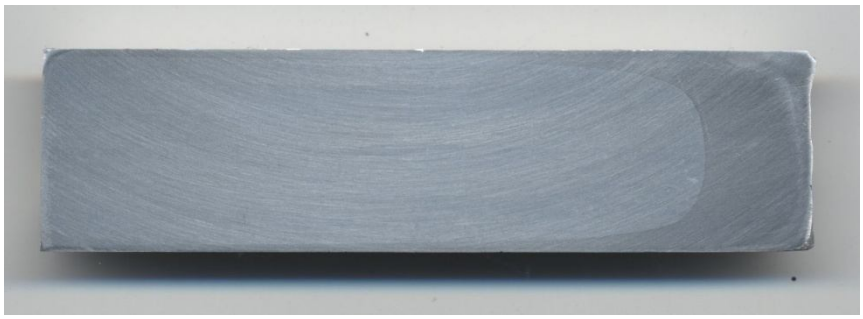

Figure 4.10: Typical charge weld

5. Results

This section deals with the experimental results obtained during the master thesis performed as described in Chapter 4.4. A summarised presentation of the TEM analysis done this semester will be given together with the hardness measurements done last semester as reported in *Characterization of precipitates at maximum hardness in Al-Mg-Si alloys* [32]. The image calibration of the CM30 films and the results from the casting and extrusion process will also be presented. Chapter 5.1 and 5.2 presents the results from the analysis of KK5, KK6 and KK7 at maximum hardness after artificial ageing at 200 °C and 250 °C, respectively. The results from the analysis of the local maximum hardness peaks after artificial ageing at 200 °C are given in Chapter 5.3. These three chapters are further divided into two subchapters; one overall microstructural analysis chapter which does not discriminate between the different precipitates, and another where the number density, volume fraction, cross section area and relative are calculated for each of the different type of precipitates present at a given condition. In Chapter 5.4, one zoomed in image for each type of precipitate observed during the master thesis is given.

5.1. Maximum hardness for artificial ageing at 200 °C

5.1.1. Overall analysis

The results from the overall TEM analysis of maximum hardness for the three alloys KK5, KK6 and KK7 artificially aged at 200 °C are given below. The TEM images that were used for calculation of average needle length, length distribution and number density were taken with a JEOL JEM-2010 at Department of Materials Science and Engineering at magnifications of 30k and 40k. One such image for each of the alloys is given in Figures 5.1 (a)-(c). Four more examples are given in Figures C.1 (a)-(d), C.3 (a)-(d) and C.5 (a)-(d) in Appendix C for KK5, KK6 and KK7, respectively. The precipitates were identified from images taken with Philips CM30 Department of Physics at magnifications of 420k and 600k before calculation of average cross section area, volume fraction and amount of the different precipitates present. Examples of these images are given in Figures 5.2 (a)-(c) and more in Figures C.2 (a)-(d), C.4 (a)-(d) and C.6 (a)-(d) in Appendix C. Average length, average cross section area, number density and volume fraction of the needle shaped precipitates are given

in Table 5.1 for each of the three alloys together with the actual ageing time and the Vickers hardness measured with 5 kg load. The needle length distribution is given in Figure 5.3.

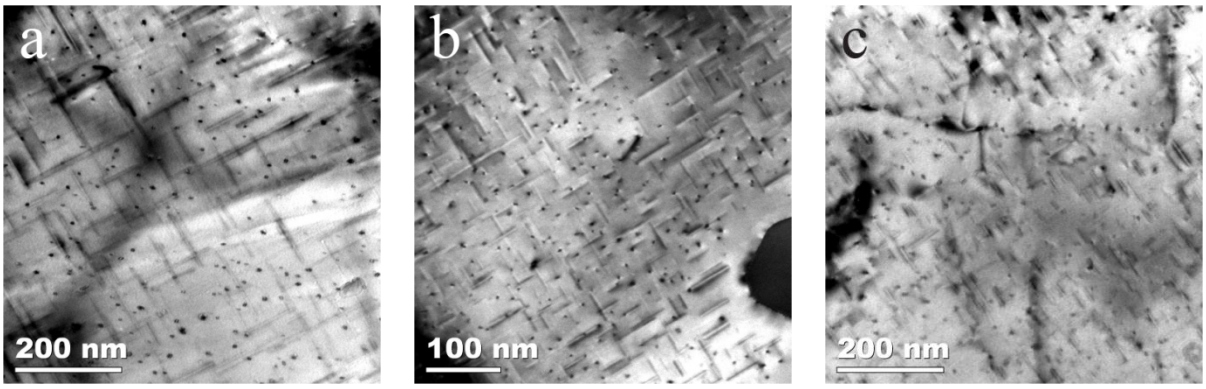

Figure 5.1: Examples of TEM images taken with JEOL JEM-2010 at max hardness after artificial ageing at 200 °C for (a) KK5 at 30k, (b) KK6 at 40k and (c) KK7 at 30k magnification

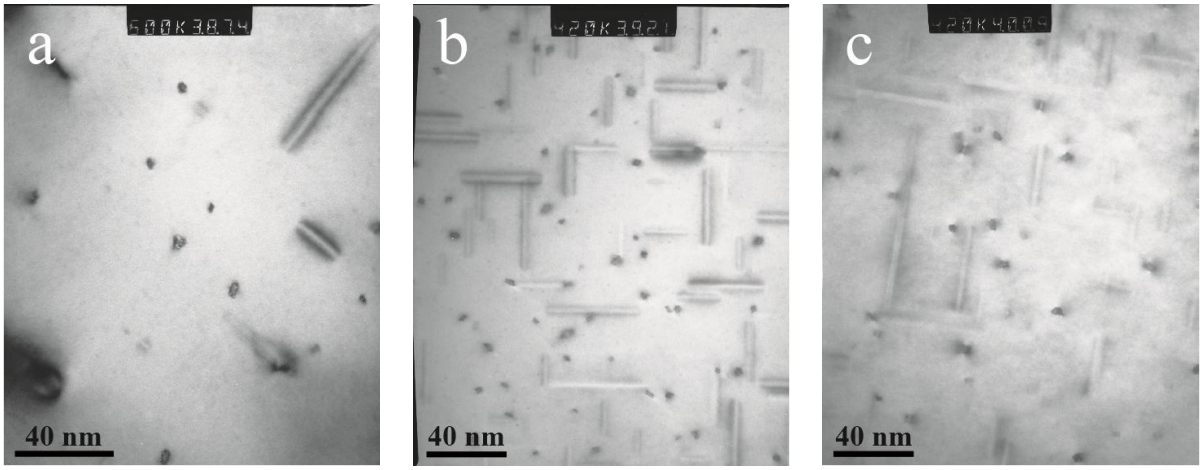

Figure 5.2: Example of TEM images taken with Philips CM30 at max hardness after artificial ageing at 200 °C for (a) KK5 at 600k, (b) KK6 at 420k and (c) KK7 at 420k magnification

Based on these images, a first observation may be seen before the analysis (Figures 5.1 and 5.2). It seems like KK6 has the highest number density and the shortest precipitates, while KK5 has the lowest number density and the longest precipitates.

Table 5.1: Analysed data at max hardness after artificial ageing at 200 °

Analysed data	KK5	KK6	KK7
Vickers hardness [HV5]	95,4	117,4	108,7
Ageing time [min]	100	60	60
Average needle length [nm]	86,04	42,56	44,39
Average cross section [nm^2]	17,95	7,72	14,17
Number density [μm^{-3}]	4679,81	19480,91	8884,74
Volume fraction [%]	0,72	0,64	0,56

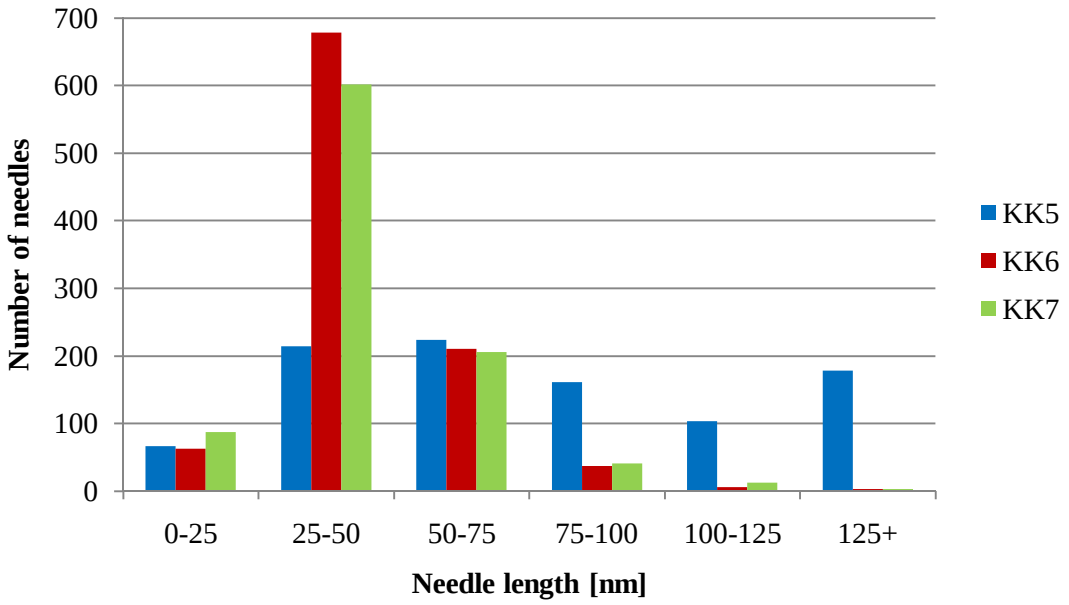

Figure 5.3: Needle length distribution at max hardness after artificial ageing at 200 °C

For the artificial ageing temperature of 200 °C, maximum hardness occurs after relative long ageing times and the Vickers hardness values for the different alloys are quite different from one another (Table 5.1). The Vickers hardness seems to be higher for decreasing average needle length and cross section area, and for increasing number density. KK5 has the highest volume fraction, while KK7 has the lowest. The needle length distribution seems significantly broader for KK5 and narrower for KK6 and KK7 which have a clean maximum in the length range 25-75 nm (Figure 5.3).

5.1.2. Analysis of each type of precipitate

The results from the analysis of the different type of precipitates present in KK5, KK6 and KK7 at maximum hardness after artificial ageing at 200 °C are given below. Volume fraction of the different precipitates is presented in Figure 5.4. Figures 5.5 and 5.6 give number density and cross section area of the needle precipitates, respectively. In the two first figures,

the experimental data is presented in stacked column charts where the stacked rectangles represents the volume fraction or number density for each of the precipitates while the total length of each bar gives the total number density or volume fraction at the given condition. In this way the relative amount of the different precipitates present in the three alloys is given relatively in the number density chart. The amount of the different type of precipitates is given in percent in Table A.12 in Appendix A.

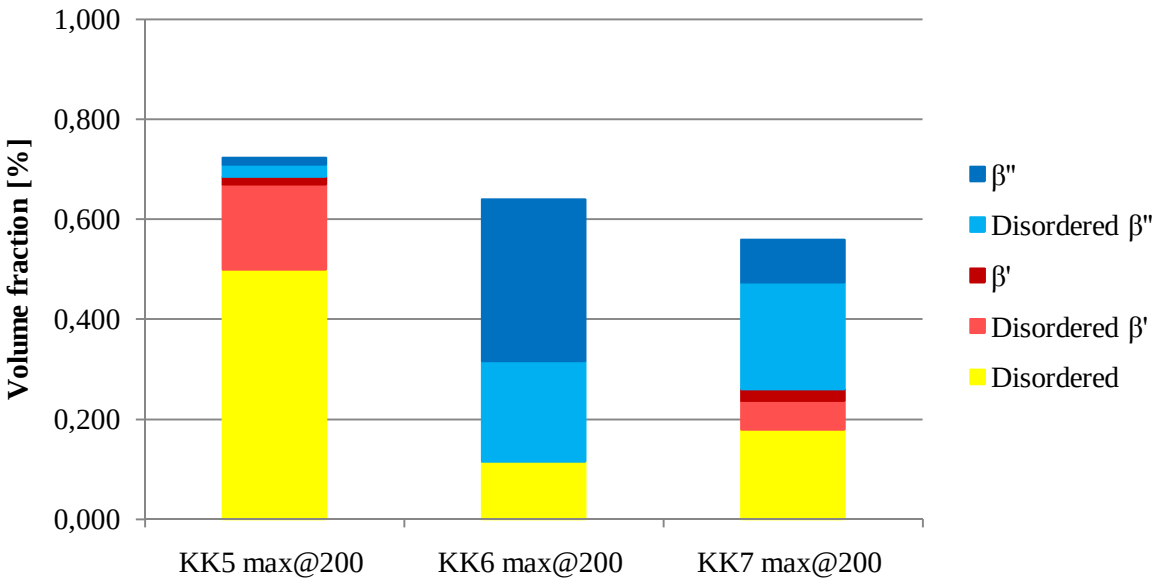

Figure 5.4: Volume fraction of needles at max hardness after artificial ageing at 200 °C for the different type of precipitates

The volume fraction is high for the β' and fully disordered precipitates in KK5 (Figure 5.4). For KK6 the β" precipitates have a high volume fraction, while the disordered precipitates have a medium value. The volume fraction is highest for the disordered β" and disordered precipitates for KK7. As already seen in Table 5.1 in Chapter 5.1.1, the total volume fraction is highest for KK5 and lowest for KK7.

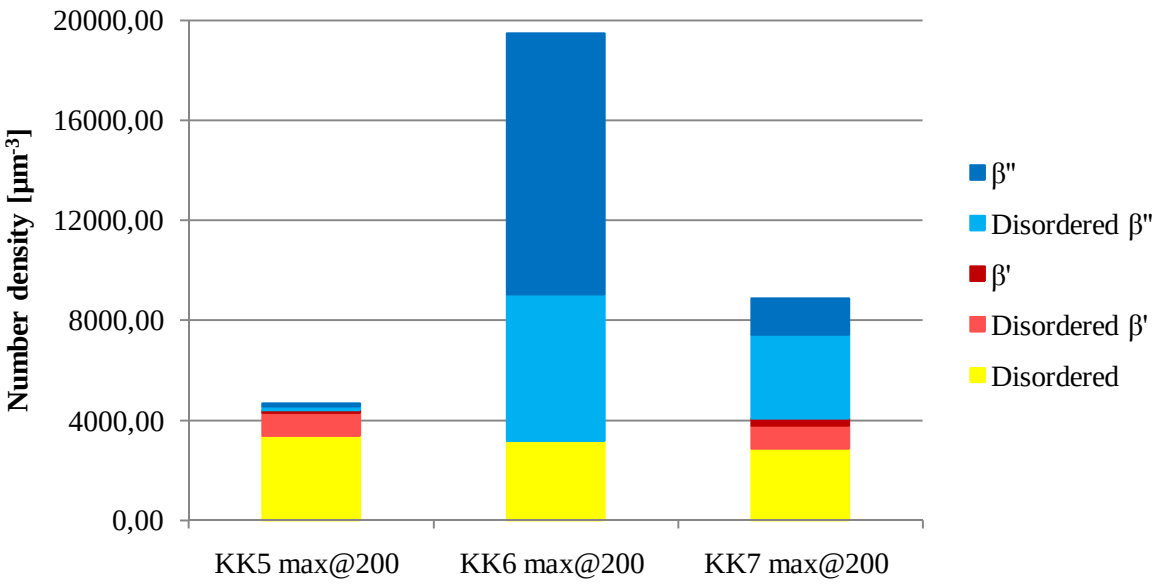

Figure 5.5: Needle number density at max hardness after artificial ageing at 200 °C for the different type of precipitates

One may see that KK6 has the largest amount β" precipitates and the smallest amount of disordered precipitates, while KK5 has the lowest amount β" and largest amount of disordered precipitates (Figure 5.5). The β' precipitates are not present at all in KK6. As already seen in Table 5.1 in Chapter 5.1.1, the total number density is highest for KK6 and lowest for KK5.

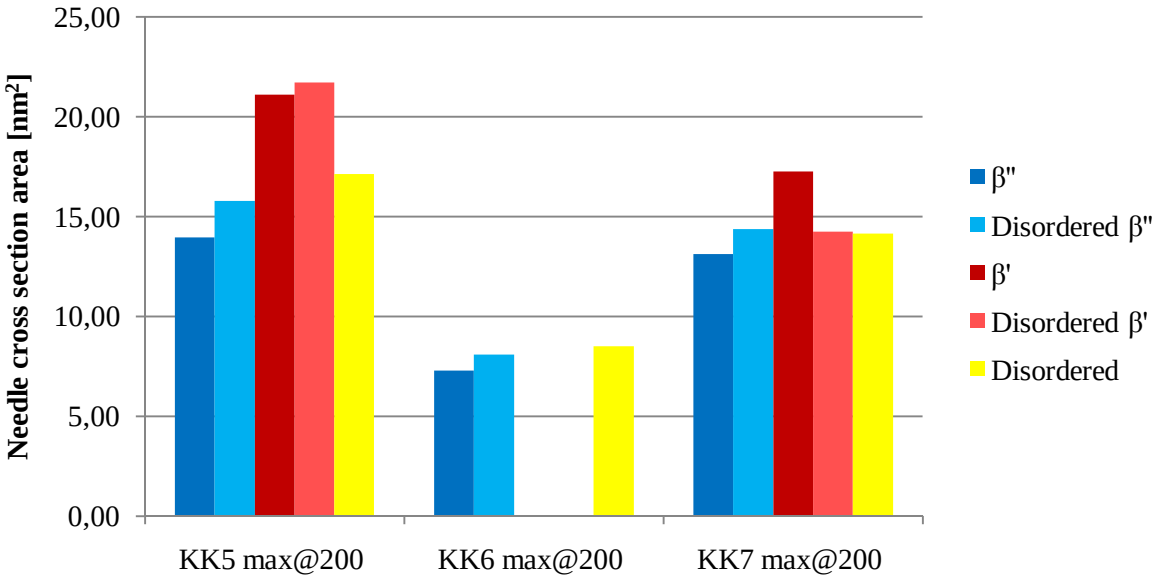

Figure 5.6: Needle cross sections at max hardness after artificial ageing at 200 °C for the different type of precipitates

It seems like both the ordered and disordered β" precipitates have a lower cross section area than the ordered and disordered β' precipitates, while the disordered precipitates tend to have a medium cross section area (Figure 5.6). From now on, if a type of precipitate is not specified as either ordered or disordered, both forms are covered. One may also observe that the cross section area for the different precipitates in general is highest for KK5, and lowest for KK6 as already seen in Table 5.1 in Chapter 5.1.1.

5.2. Maximum hardness for artificial ageing at 250 °C

5.2.1. Overall analysis

The TEM analysis of maximum hardness for the 250 °C case gave the following results. In the same way as for the 200 °C case, examples of the images taken with JEOL JEM-2010 at a magnification of 30k and with Philips CM30 at a magnification of 420k are given in Figures 5.7 (a)-(c), and Figures 5.8 (a)-(c), respectively. More example are given in Figures C.7 (a)-(d), C.9 (a)-(d) and C.11 (a)-(d) for the JEOL images and Figures C.8 (a)-(d), C.10 (a)-(d) and C.12 (a)-(d) for the Philips images in Appendix C. Vickers hardness, actual ageing time, needle length, cross section area, number density and volume fraction are presented in Table 5.2. The needle length distribution is given in Figure 5.9.

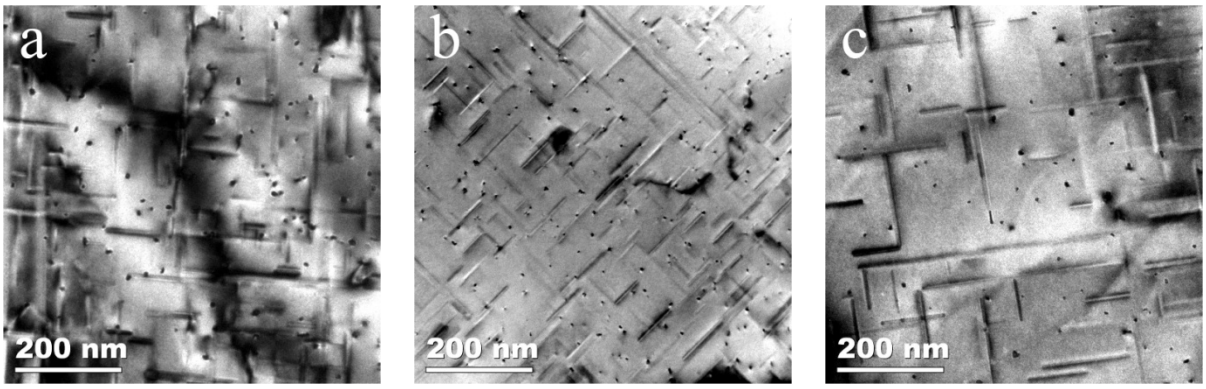

Figure 5.7: Examples of TEM images taken with JEOL JEM-2010 at max hardness after artificial ageing at 250 °C for (a) KK5, (b) KK6 and (c) KK7, all at 30k magnification

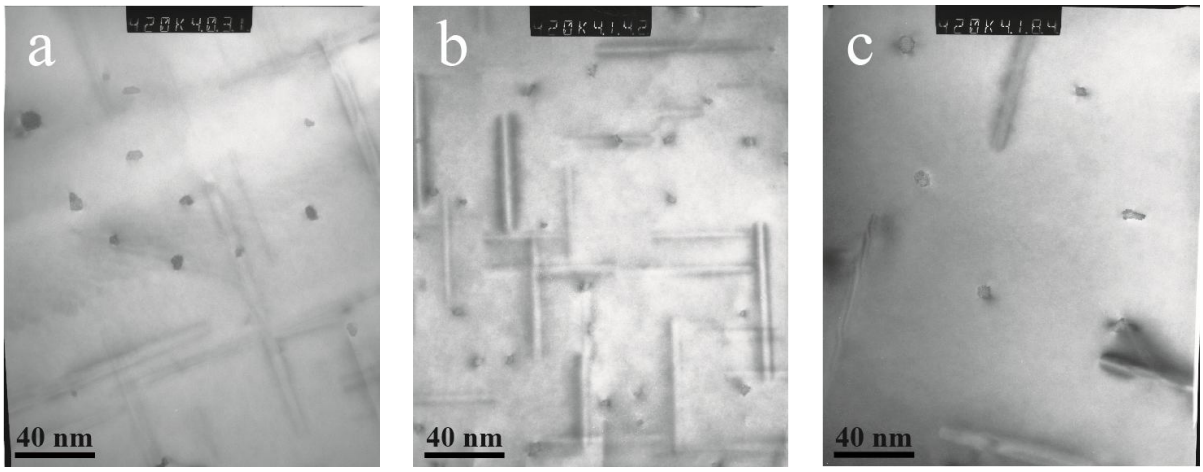

Figure 5.8: Example of TEM images taken with Philips CM30 at max hardness after artificial ageing at 250 °C for (a) KK5, (b) KK6 and (c) KK7, all at 420k magnification

Just by visual inspection of these images before analysis, it looks like KK6 has a higher number density and shorter precipitates than both KK5 and KK7 (Figures 5.7 and 5.8). However, it seems like the microstructure of KK5 and KK7 are quite similar.

Table 5.2: Analysed data at max hardness after artificial ageing at 250 °

Analysed data	KK5	KK6	KK7
Vickers hardness [HV5]	92,9	96,1	92,5
Ageing time [min]	5	4	5
Average needle length [nm]	71,75	67,14	87,60
Average cross section [nm^2]	25,77	22,21	30,71
Number density [μm^{-3}]	2565,98	5222,63	2620,56
Volume fraction [%]	0,47	0,78	0,70

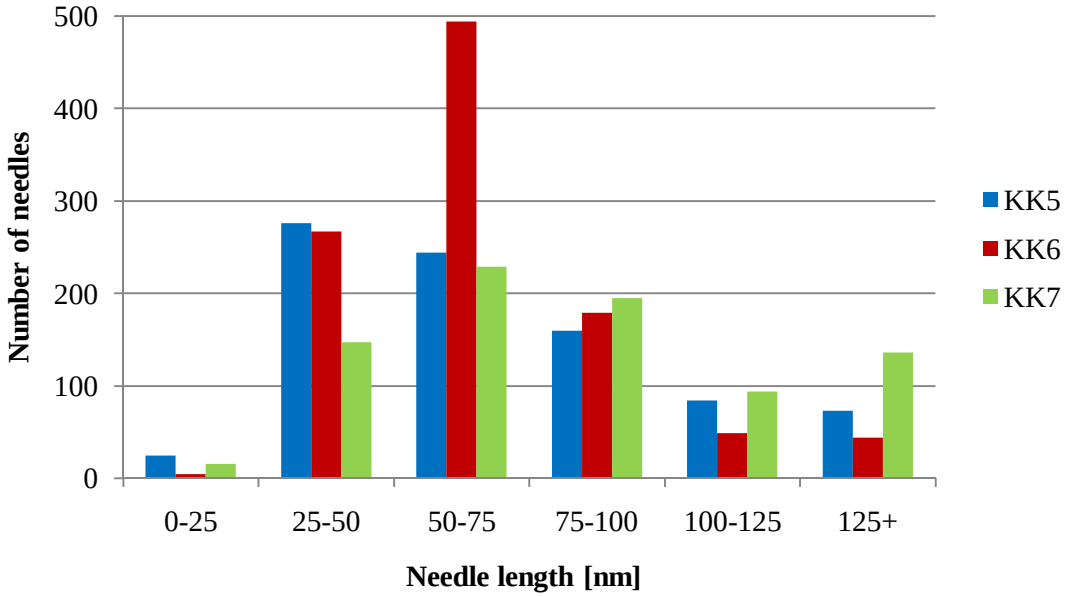

Figure 5.9: Needle length distribution at max hardness after artificial ageing at 250 °C

For artificial ageing at 250 °C, maximum hardness occurs after a very short ageing time where the Vickers hardness values for the three different alloys are much closer to one another with a lower average value of hardness (Table 5.2), close to the value for KK5 artificially aged at 200 °C (Table 5.1). Some of the trends observed in the 200 °C case, may also be seen after artificial ageing at 250 °C. KK6 is observed to have a bit higher Vickers hardness and number density than the two other alloys in addition to a lower average needle length and cross section area. However, the trend in the volume fractions is somewhat different. Here KK7 is at the same magnitude has in the 200 °C case, while the value for KK5 has decreased and for KK6 increased. The needle length distribution seems broad quite broad for all the alloys (Figure 5.9), and broader in general than at 200 °C (Figure 5.3).

5.2.2. Analysis of each type of precipitate

The analysis of the different type of precipitates present at maximum hardness after artificial ageing at 250 °C gave the following results. Volume fraction, number density and needle cross section area are presented in Figures 5.10-12, respectively. As in the 200 °C case, the amount of the different type of precipitates may be seen from the number density chart, but is also given in percent in Table A.13 in Appendix A. The first observation made is that a higher number of different precipitates are present after artificial ageing for 250 °C than in the 200 °C case.

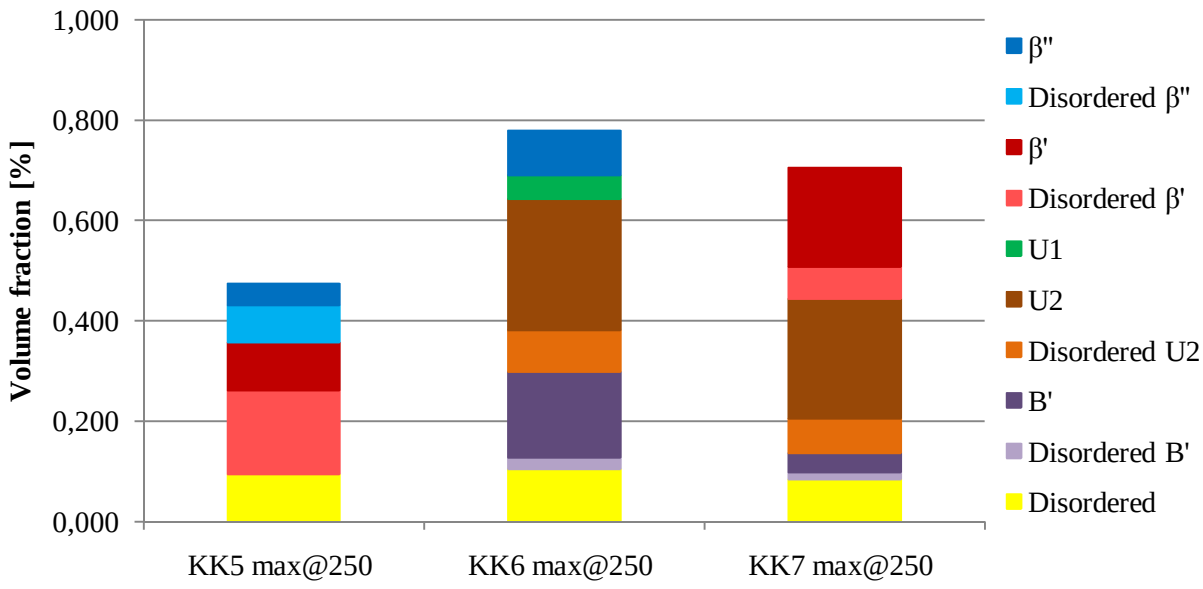

Figure 5.10: Volume fraction of needles at max hardness after artificial ageing at 250 °C for the different type of precipitates

The volume fraction is lowest for KK5 and highest for KK7 (Figure 5.10), at approximately the same order of magnitude as for the 200 °C case (Figure 5.4). The volume fraction distribution is very complex, but ordered U2 has a large volume fraction for both KK6 and KK7. U1 and disordered B' precipitates have a small volume fraction.

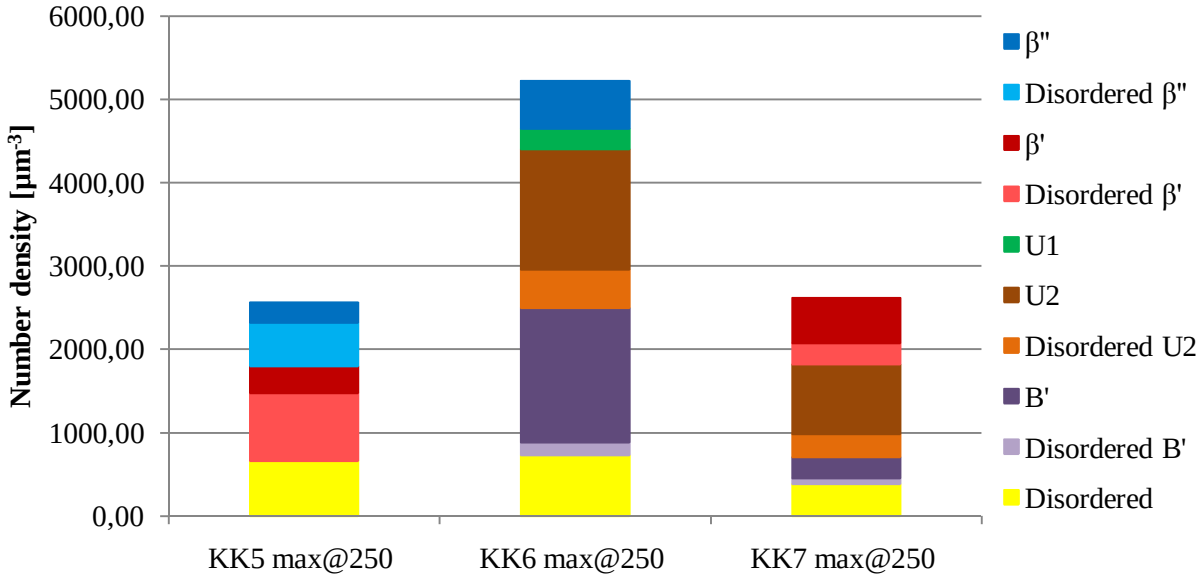

Figure 5.11: Needle number density at max hardness after artificial ageing at 250 °C for the different type of precipitates

It is observed that the amount of ordered β" and completely disordered precipitates in general has been reduced (Figure 5.11) compared to the maximum hardness after artificial ageing at 200 °C (Figure 5.5), while the amount of post-β" precipitates has increased. The β' precipitates are still only present in KK5 and KK7. On the other hand, the B' precipitates are only present in relatively large amounts in KK6 and some in KK7. The amount of disordered post-β" precipitates is generally low. The total number density is observed to be highest for KK6 and lower for both KK5 and KK7 as also seen in Table 5.2 in Chapter 5.2.1.

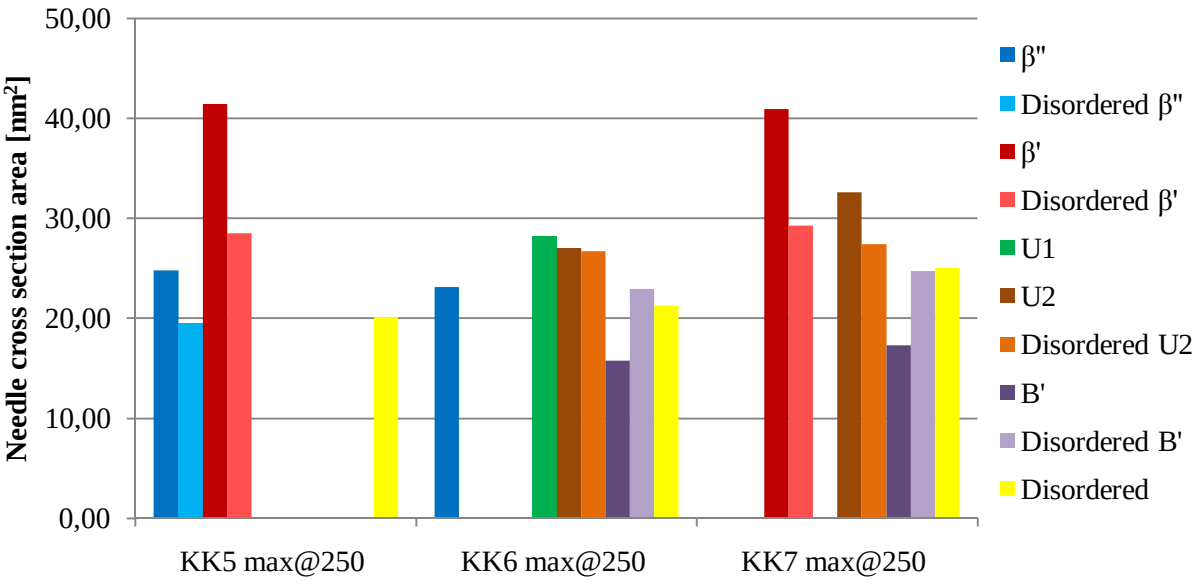

Figure 5.12: Needle cross sections at max hardness after artificial ageing at 250 °C for the different type of precipitates

As already seen in Table 5.2 in Chapter 5.2.1, the average cross section area is lowest for KK6 and highest for KK7 (Figure 5.12), and all the alloys show a higher cross section area than at 200 °C in general (Figure 5.6). The ordered β' precipitates have the largest average cross section area, while the ordered B' precipitates have the lowest. The other precipitates have values in between.

5.3. Local peaks at overaged conditions for artificial ageing at 200 °C

5.3.1. Overall analysis

The results from the TEM analysis of the local maximum hardness peaks at overaged conditions for KK5, KK6 and KK7 artificially aged at 200 °C are given below. A before-peak KK5 sample (called KK5 BP) which represents a lower hardness and shorter ageing time right than KK5, is also investigated. Examples of the images taken with JEOL JEM-2010 at a magnification of 30k and with Philips CM30 at a magnification of 420k are given in Figures 5.13 (a)-(d) and Figures 5.14 (a)-(d), respectively. More example are given in Figures C.13 (a)-(d), C.15 (a)-(d), C.17 (a)-(d) and C.19 (a)-(d) for the JEOL images and Figures C.14 (a)-(d), C.16 (a)-(d), C.18 (a)-(d) and C.20 (a)-(d) for the Philips images in Appendix C. Vickers hardness, actual ageing time, needle length, cross section area, number density and volume fraction are presented in Table 5.3. The needle length distributions are given in Figure 5.15.

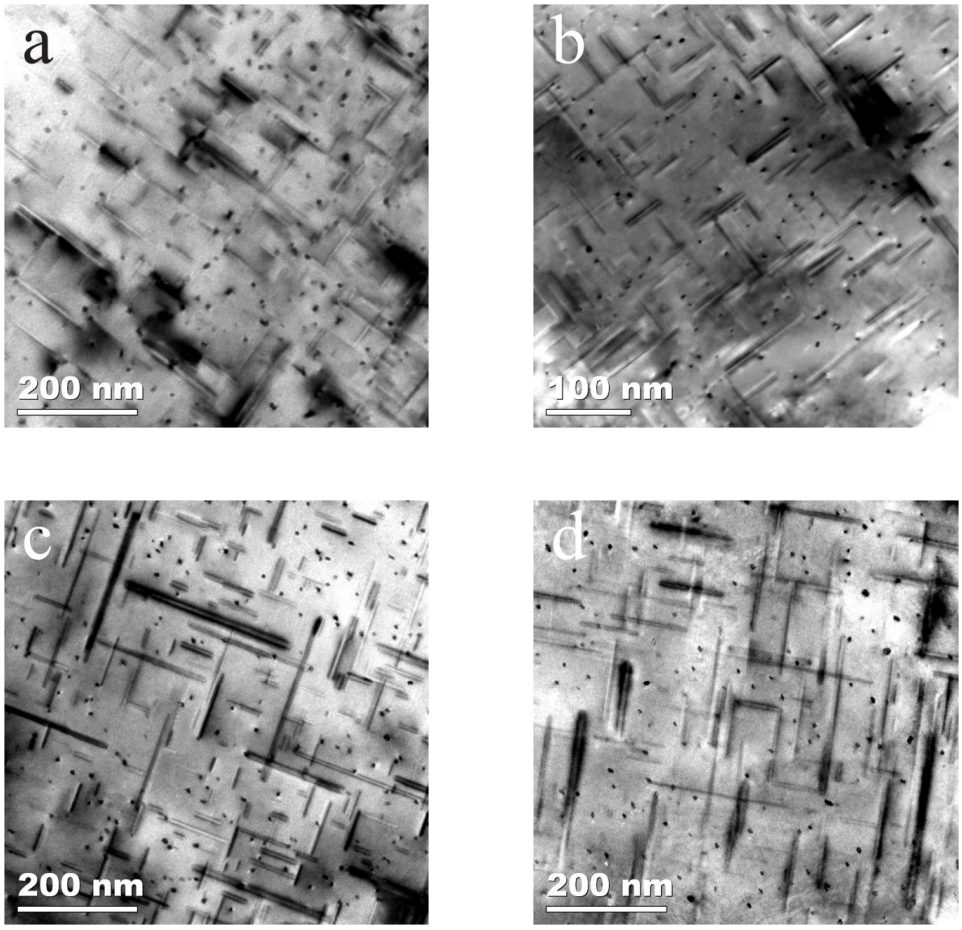

Figure 5.13: Examples of TEM images taken with JEOL JEM-2010 at local max at overaged conditions after artificial ageing at 200 °C for (a) KK5 at 30k, (b) KK6 at 40k, (c) KK7 at 30k and (d) KK5 before peak at 30k magnification

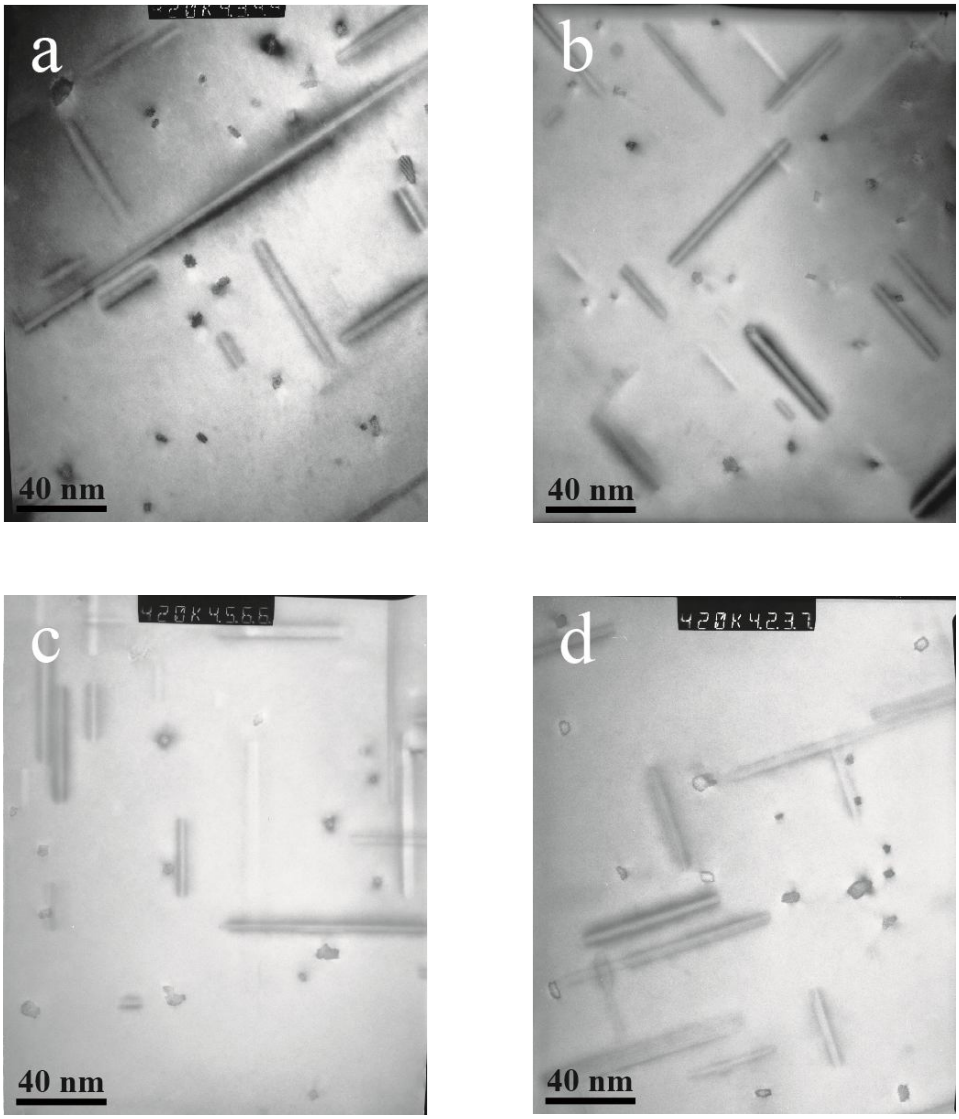

Figure 5.14: Example of TEM images taken with Philips CM30 at local max at overaged conditions after artificial ageing at 200 °C for (a) KK5 (b) KK6, (c) KK7 and (d) KK5 before peak, all at 420k magnification

Without any detailed analysis of these images, it seems like KK6 has the highest number density and the shortest precipitates (Figures 5.13 and 5.14). In addition, it looks like both KK5 and KK5 BP have low values of number density.

Table 5.3: Analysed data at local max hardness after artificial ageing at 200 °C

Analysed data	KK5	KK6	KK7	KK5 BP
Vickers hardness [HV5]	96,6	102,9	102,4	88,9
Ageing time [min]	600	600	420	360
Average needle length [nm]	73,77	49,44	72,54	88,31
Average cross section [nm^2]	22,86	10,88	57,96	23,51
Number density [μm^{-3}]	4605,92	9607,56	6463,02	3705,11
Volume fraction [%]	0,78	0,52	2,72	0,77

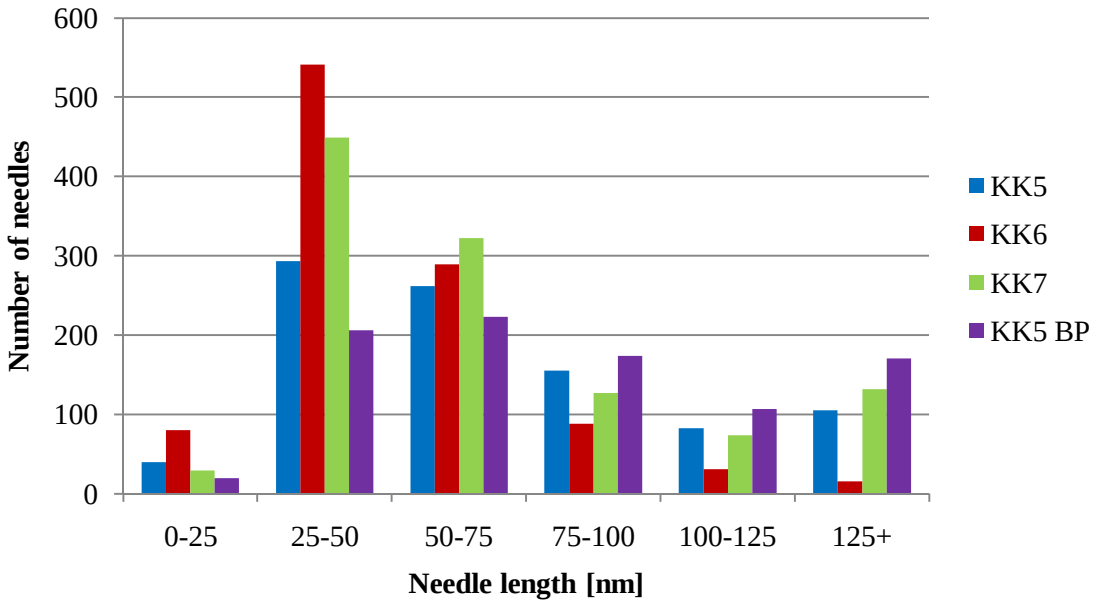

Figure 5.15: Needle length distribution at local max hardness after artificial ageing at 200 °C

By first considering the local maximum conditions, one may observe that the Vickers hardness values (Table 5.3) are very close to each other like for the 250 °C case (Table 5.2), but also here KK6 is observed to have a bit higher Vickers hardness, while KK5 has the lowest. As earlier, the same trend is observed, namely the fact that KK6 has the highest number density, and the lowest average needle length and cross section area. Here KK7 clearly has the highest volume fraction, while KK5 has a bit higher volume fraction than KK6. The needle length distribution is broad for all alloys (Figure 5.15) like for the 250 °C case (Figure 5.9). KK5 BP has a lower hardness than KK5. By comparing these two, some of the same trends as earlier are observed. KK5 has longer needles with larger cross sections in addition to a higher number density and amount of disordered precipitates than KK5 BP. The volume fraction is approximately the same for the two conditions.

5.3.2. Analysis of each type of precipitate

The results from the analysis of different type of precipitates present in KK5, KK6 and KK7 at local maximum hardness peaks after artificial ageing at 200 °C are given below. Volume fraction, number density and needle cross section area are presented in Figures 5.16-5.18, respectively. The amount of the different precipitates is given relatively in Figure 5.17, but is also presented in percent in Table A.14 in Appendix A.

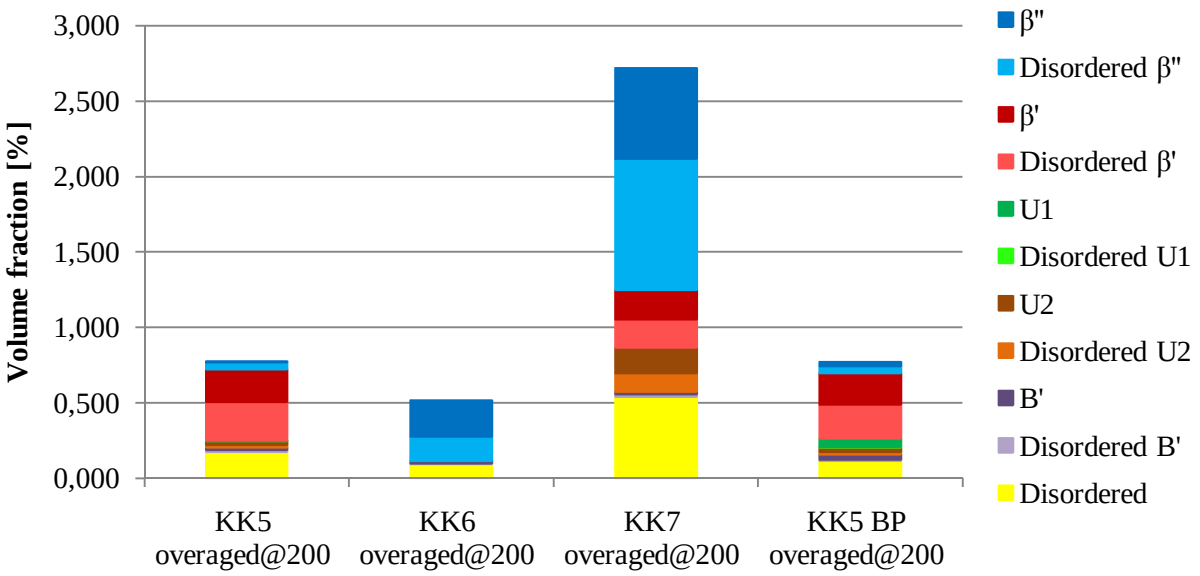

Figure 5.16: Volume fraction of needles at overaged local max hardness after artificial ageing at 200 °C for the different type of precipitates

By first considering the local maximum conditions, one may observe that volume fraction of the completely disordered precipitates have increased for KK5 and KK7 (Figure 5.16) compared to the case with maximum hardness after artificial ageing at 200 °C (Figure 5.4). The volume fraction of the β" precipitates have also increased noticeably for KK7. The U1, U2 and B' precipitates have a relatively low volume fraction in general. As already seen in Table 5.3 in Chapter 5.3.1, the volume fraction is highest for KK7 and lowest for KK6. By comparing KK5 and KK5 BP, the volume fraction has increased for ordered U1 and decreased for disordered precipitates for KK5 BP. The total volume fraction is approximately the same in the two cases as already seen in Table 5.3.

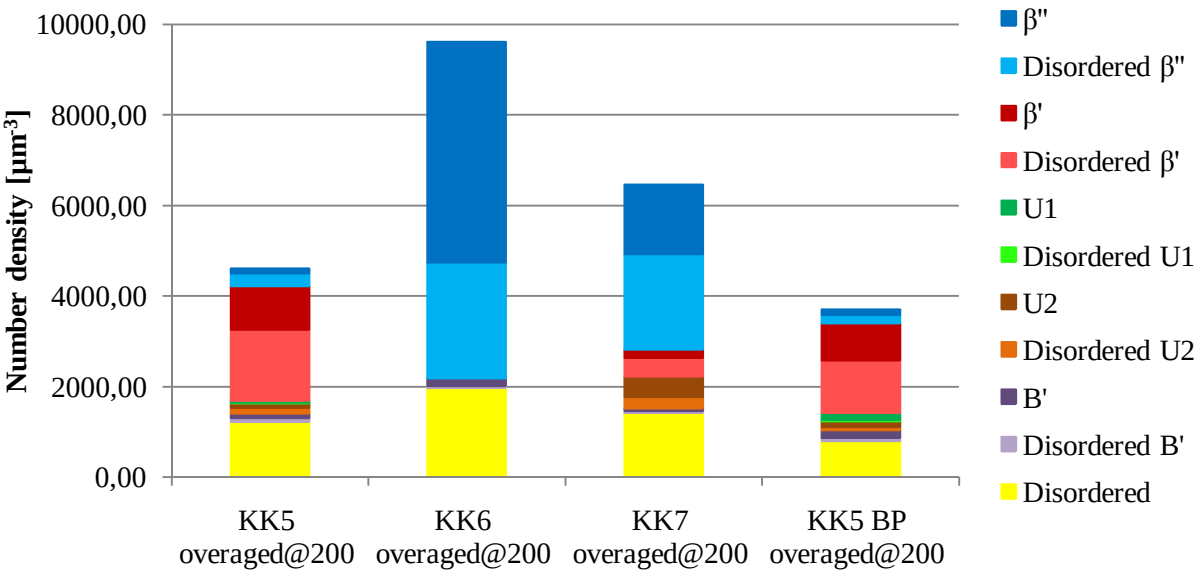

Figure 5.17: Needle number density at overaged local max hardness after artificial ageing at 200 °C for the different type of precipitates

It may be seen that the total number density is highest for KK6 and lowest for KK5 among the local maximum conditions (Figure 5.17) which also have been seen in Table 5.3 in Chapter 5.3.1. Like for maximum hardness after artificial ageing at 250 °C (Figure 5.11), more type of post-β" precipitates are present at this condition than at maximum hardness after artificial ageing at 200 °C. However, very little amount of the new precipitates were formed, so the amount of the β" and β' and disordered precipitates is not that different from the maximum hardness condition. By comparing KK5 with KK5 BP, one may see that KK5 BP has the lowest number density. The amount of the different precipitates is quite similar in the two conditions, but the amount of ordered U1, U2 and B' have increased a bit for KK5 BP on the expense of disordered β" and β' in addition to disordered precipitates.

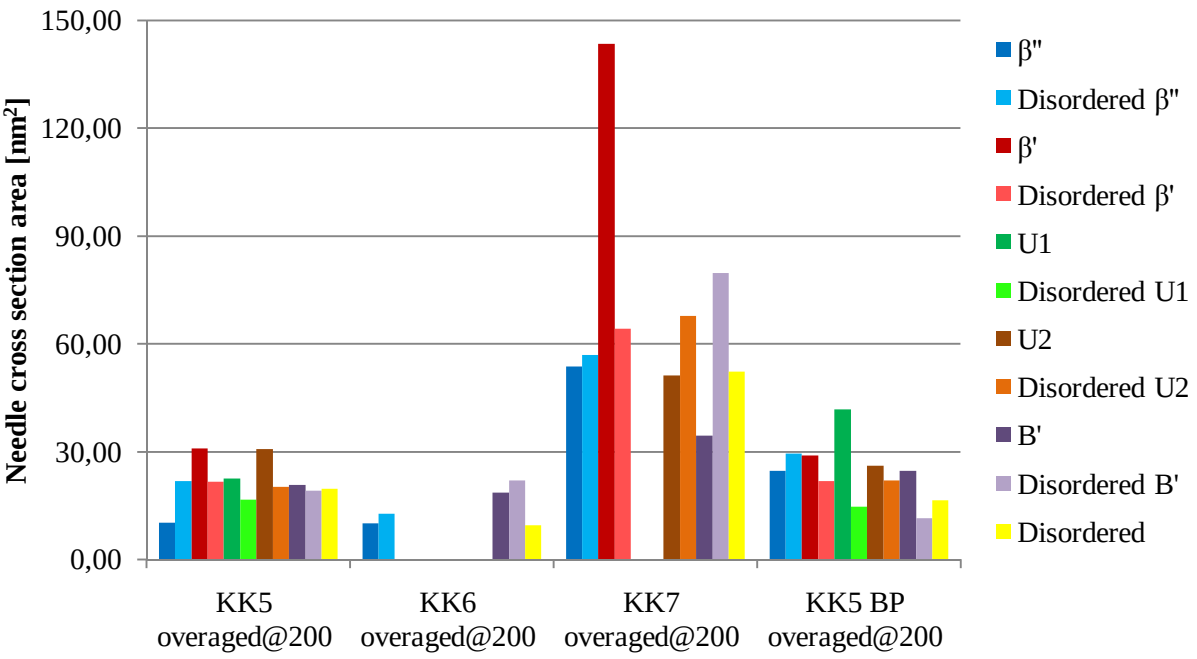

Figure 5.18: Needle cross sections at overaged local max hardness after artificial ageing at 200 °C for the different type of precipitates

By first considering the local maximum conditions, the ordered β' precipitates still have quite large cross sections compared to the other precipitates, especially for KK7 (Figure 5.18). In general, the cross section area is higher than at maximum hardness for the same artificial ageing temperature (Figure 5.6), but still with the same trend, that is KK7 has the largest cross section and KK6 the smallest as already seen in table 5.3 in Chapter 5.3.1. KK5 BP presents a condition at a shorter ageing time and lower hardness than KK5. By comparing these two, one may observe that the cross section of ordered U1 has increased noticeably for KK5 BP, and that this condition represents a bit larger cross section in general which also can be seen from Table 5.3.

5.4. Precipitates in high resolution images

The different type of precipitates present and their relative amounts for the different conditions have already been presented without any visual examples. Therefore, one zoomed in image for each type of precipitate observed during the master thesis is given in Figures 5.19 (a)-(e). It is observed that the crystal structure of the precipitates obtained agree with the reported crystal structures given in Figure 2.15 in Chapter 2.3.3.

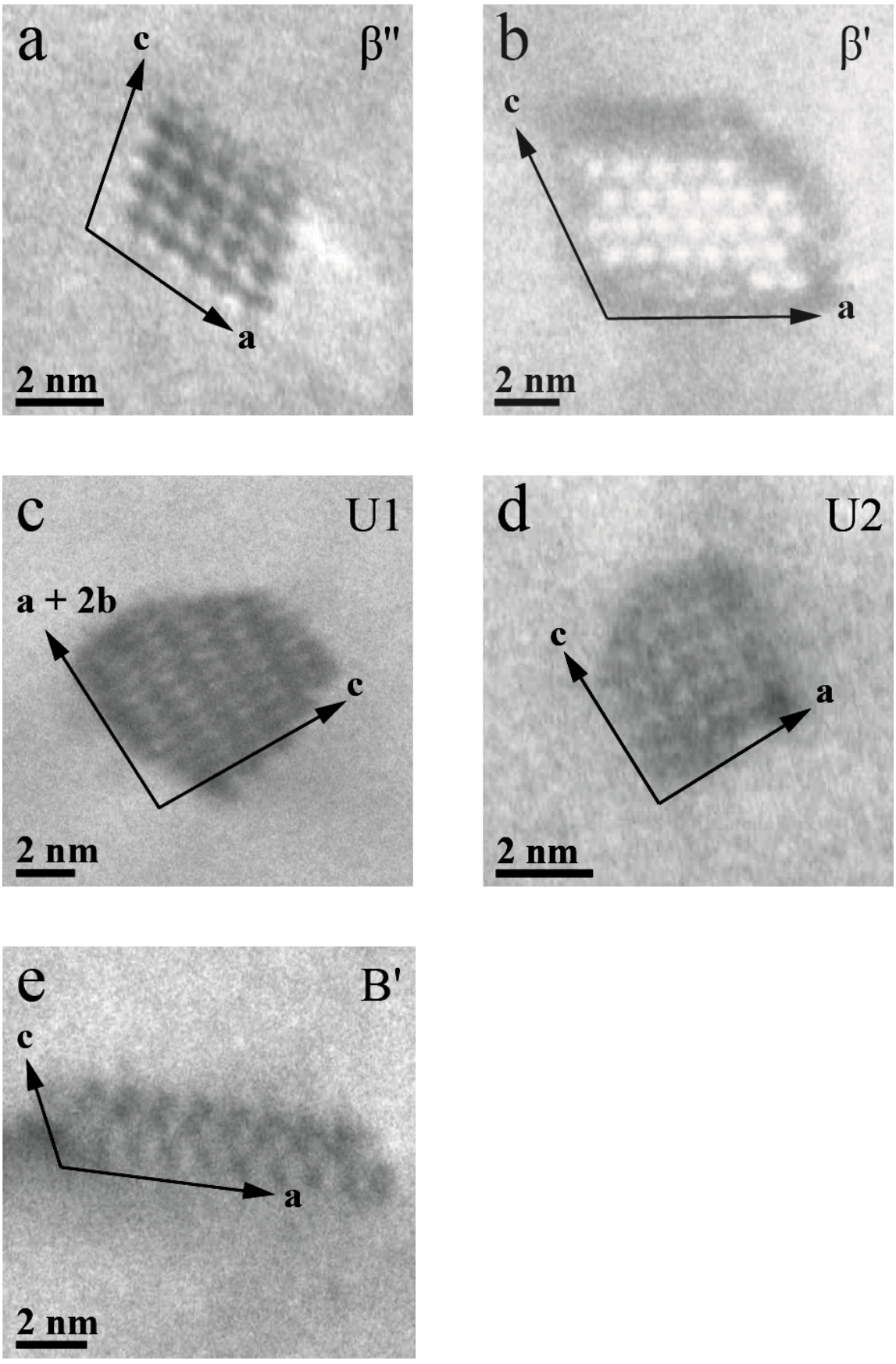

Figure 5.19: High resolution TEM image of (a) β'', (b) β', (c) U1, (d) U2 and (e) B'

6. Analysis and discussion

This section draws together and summarises the findings of Chapter 5 in combination with the previous work presented in Chapter 3. In Chapters 6.1-6.3, the experimental results from the investigation of KK5, KK6 and KK7 will be discussed individually for each of the given ageing conditions. A general comparison of the different conditions in order to get an overall understanding of the aging behaviour in these alloys is discussed in Chapter 6.4.

6.1. Maximum hardness for artificial ageing at 200 °C

Maximum hardness for KK5, KK6 and KK7 after artificial ageing at 200 °C differs noticeably in magnitude as seen in Table 5.1 in Chapter 5.1.1, where KK6 has the highest Vickers hardness and KK5 the lowest. From Chapter 2.3.3 it is known that Si-rich alloys have a fine precipitate microstructure with high and sharp peak hardness, and that Mg-rich alloys have a coarse microstructure and overage faster than Si-rich alloys resulting in strength reduction. By referring to Table 4.1 in Chapter 4.1.1, this relationship is clearly verified by the fact that KK6 is Si-rich, while KK5 is Mg-rich. By considering the obtained quantitative experimental data (Table 5.1), one may observe that KK6 has the highest number density and the lowest average needle length and cross section area, or in other words a large number of fine precipitates. KK5, on the other hand, is observed to have the coarsest precipitates and the lowest number density, so the effect of the Si/Mg amount is again verified. From Chapter 2.3.2 it is known that the precipitates generally increase the alloy strength with decreasing particle size, and increasing volume fraction and number density of the precipitates. The quantitative data obtained (Table 5.1) seem to agree with the theory, except for the volume fraction which should be highest for KK6 and lowest for KK5. A deviation from this relationship is observed. Here KK5 has the highest volume fraction, while KK7 has the lowest. Similar deviations has been reported earlier as described in Chapter 3.2, and is due to the substitution of β" with post-β" precipitates for the tempers resulting in such precipitates.

When it comes to the average needle length distribution in KK5, KK6 and KK7 at this condition, it is seen from Figure 5.3 in Chapter 5.1.1 that KK5 has a very broad distribution which indicates that different type of precipitates in considerably large amounts contribute to the precipitation hardening effect as stated in Chapter 2.3.3. The KK6 alloy, on the other

hand, has a very narrow distribution which therefore should contain either fewer type of precipitates, or that one of them is in great excess so that the others have little effect on the distribution. The distribution of KK7 is also narrow, but a bit broader than KK6. The amount of different precipitates present at maximum hardness in the three alloys after artificial ageing at 200 °C is given relatively in Figure 5.5 in Chapter 5.1.2 which actually shows the number density of the precipitates. These amounts are also given in percent in Table A.12 in Appendix A. One may observe that over 80 % of the precipitates in KK6 are β" precipitates (Figure 5.5), which explains the narrow needle length distribution. The theory behind this distribution (Chapter 2.3.3) also holds for KK7 which contains about 50 % β" precipitates, while the rest is represented by β' in addition to disordered precipitates. The broad needle length distribution for KK5 may be explained by the large number of partly disordered and disordered precipitates of about 90 % (Figure 5.5). The differences in the amount of the different precipitates in the three alloys also affect the observed variations in the Vickers hardness. The amount of the β" precipitates is highest in KK6 and lowest in KK5. The amount of the β' precipitates, on the other hand, is higher in KK7 than in KK6, and even higher in KK5. It was stated in Chapter 2.3.3 that the maximum hardness and strength is obtained by the β" precipitate, which seems to agree with the measured hardness for the three alloys. The high amount of disordered precipitates in KK5 is probably due to transformation from β" to β' precipitates as stated in Chapter 2.3.3. The same phenomenon is observed for KK7, but in a less degree. KK6 has a low amount of disordered precipitates since above 80 % of the microstructure consists untransformed β" precipitates.

The results from the analysis of each type of precipitate show that their contribution to the precipitate hardening effect is varying. By considering the volume fraction and the number density of the different precipitates given in Figures 5.4 and 5.5 in Chapter 5.1.2, respectively, it seems like these two quantities are related by means of their relative values for each temper. As an example, one may observe that both the number density and the volume fraction of the disordered precipitates in KK5 represent approximately 70 % of the total values (Figures 5.4 and 5.5). Since relative values in the number density chart also represents the relative amount of the different precipitates present in the three alloys, both the number densities and the volume fractions for the different precipitates are reflected in the percentage amount. Naturally, this means that the type of precipitates with high number density and volume fraction contribute more to the alloy hardening than the type of precipitates with low number density and volume fraction. However, the total volume fraction and number density does not

show the same relationship in such way that only increased total number density gives increased Vickers hardness as already discussed. The average needle cross section area chart in Figure 5.3 in Chapter 5.1.1 was broke down into the chart in Figure 5.6 in Chapter 5.1.2 where the cross section is presented for each of the precipitates present in KK5, KK6 and KK7. The trend seems to be that the β" precipitates in general have smaller cross sections than the β' precipitates (Figure 5.6) which means that the β" precipitates are finer and represent a greater contribution to the alloy hardness as explained in Chapter 2.3.2. It looks like an average ordered β" precipitate has a smaller cross section than a disordered β". In addition, it seems like the disordered precipitates get an average needle cross section in between that of the β" and β' precipitates.

The reason for the observed differences in the Vickers hardness for KK5, KK6 and KK7 at maximum hardness after artificial ageing at 200 °C was, in the project work, concluded to be that the precipitates present in each alloy were of different types as mentioned in Chapter 3.3. This conclusion was not correct since the type of precipitates present in the three alloys was partly or completely the same for all three alloys at this condition. It is seen that the actual reason for this deviation is due to several factors. The Vickers hardness is affected, not only by the type of precipitates present, but also by their amount and the obtained microstructure through quantities like size, number density and volume fraction. In addition all the different precipitates contribute differently to these quantities.

6.2. Maximum hardness for artificial ageing at 250 °C

From Table 5.2 in Chapter 5.2.1, the Vickers hardness of KK5, KK6 and KK7 at maximum hardness after artificial ageing at 250 °C is observed to be very close to each other at values quite similar to the Vickers hardness at maximum hardness for KK5 after artificial ageing at 200 °C. However, the Si-rich nature of KK6 still gives a bit higher value of hardness than the two others as discussed in Chapter 6.1. The fact that the maximum hardness values for the different alloys seem to approach each other at lower maximum hardness values is probably because all of them are going through overageing as presented in Chapter 2.3.1. The results from the quantitative measurements of the three alloys, given in Table 5.2 in Chapter 5.2.1, show that KK6 has the highest Vickers hardness because it has the smallest precipitates and the highest number density. In addition, KK5 and KK7 have approximately the same value of

number density which and that they both have coarser precipitates than KK6 which explains why the hardness values of KK5 and KK7 are so similar, but lower than for KK6. Like for the maximum hardness after artificial ageing at 200 °C, the volume fraction is observed to deviate from the relationship with Vickers hardness (Table 5.2) due to post-β" precipitates as discussed in Chapter 6.1.

The needle length distribution at maximum hardness after artificial ageing at 250 °C is relatively broad for all three alloys as seen from Figure 5.9 in Chapter 5.2.1 which indicates different type of precipitates as discussed in Chapter 6.1. From Figure 5.11 in Chapter 5.2.2, the relative amount of the different precipitates present is presented by the relative number densities in the number density chart, and these are also given in percent in Table A.13 in Appendix A. It can be seen that all the alloys in general have several type of precipitates without any of them in a particular large excess which verifies the observed broad needle distributions. However, the reason for KK6 having a bit more narrow distribution is not explained since KK5 has less type of precipitates than both KK6 and KK7, and that all the alloys show groups of a few type of precipitates in excess which are of approximately the same magnitude. Maximum strength is obtained by the β" precipitates as discussed in Chapter 6.1. However, for this condition the amount of these precipitates is relatively low for both KK5 and KK6, and is actually zero in KK7 (Figure 5.11). Thus, the observed hardness differences are not due to these precipitates, but the findings obtained by SINTEF might explain this behaviour. It was found that an additional hardening effect in the U2 and B' precipitates represent a greater contribution to the alloy hardness than the U1 and β' precipitates (Chapter 3.2). From Figure 5.11 one may observe that KK6 contains both β", U2 and B' precipitates in medium amounts, little U1 and no β'. In other words this alloy has more precipitates with greater hardening effect and less with poorer hardening effect which probably explains why KK6 show the highest value of Vickers hardness. By comparing KK5 and KK7, one may observe that KK5 contain medium amounts of β" and β' precipitates, while KK7 is characterized by medium amounts of U2 and β' precipitates. Thus, it is likely that the similar values of Vickers hardness for these two alloys are caused by the fact that they both have approximately the same amount of precipitates with greater and poorer hardening effects. The fact that β" is observed at all is a little surprising since none were present after artificial ageing at 260 °C as seen from Table 3.2 in Chapter 3.2. However, the high degree of overageing is still verified due to large amounts of both post-β" and disordered precipitates for all three alloys (Figure 5.11). For the KK7 alloy, some of the β' precipitates formed have

transformed further into U2 and B' precipitates, while the formation of β' precipitates is not observed at all for KK6.

The analysis of each type of precipitate present at maximum hardness after artificial ageing at 250 °C suggests that their contribution to the hardness is somewhat different. Also at this condition, is seems to be a relationship between volume fraction (Figure 5.10), number density (Figure 5.11) and amount in percent (Table A.13) of the different precipitates present in the same way as for maximum hardness after artificial ageing at 200 °C (Chapter 6.1). This means that precipitates with large number densities and volume fractions contribute more to the alloy hardness. Also here, the total volume fraction and the total number density do not show this relationship in the same way as for the first condition discussed. From Figure 5.12 in Chapter 5.2.2, it can be seen that the different precipitates get various cross section areas depending on their atomic structure. The β' precipitates still have the largest cross sections and therefore contribute to the hardness in a less degree than the other precipitates given that these are harder than the β' precipitates as already discussed. The smallest cross sections are found in the B' precipitates which therefore contribute more to the alloy hardness. Intermediate needle cross sections are observed for the β", U1 and U2 precipitates. By common sense one would expect the partly disordered precipitates to get a cross section between the disordered and each of the ordered precipitates. By investigation this is confirmed (Figure 5.12). The precipitates with intermediate cross section areas will therefore most likely give a medium contribution to the hardness.

In the project work it was concluded that the Vickers hardness for KK5, KK6 and KK7 at maximum hardness after artificial ageing at 250 °C was due to the fact that the precipitates present were of the same type as stated in Chapter 3.3. This was not correct either since the type of precipitates present in the three alloys was somewhat different. Also here the actual conclusion is far more complex. For this condition the precipitates present and the amount of them still affects the Vickers hardness, but the obtained microstructural quantities like size, number density and volume fraction seem to have somewhat greater impact on the hardness. In addition all the different precipitates are observed to contribute differently to these quantities.

6.3. Local peaks at overaged conditions for artificial ageing at 200 °C

The last condition investigated was the local maximum hardness for KK5, KK6 and KK7 at overaged conditions for artificial ageing at 200 °C. From Table 5.3 in Chapter 5.3.1 it is seen that the Vickers hardness value for each alloy is not too far away from each other. KK6 and KK7 show approximately the same value, while KK5 has a bit lower hardness. The difference in the Si/Mg ratio for the three alloys is not observed to have any particular effect on the hardness curves since they have become so close in magnitude. This is most likely due to the fact that all the alloys are at overaged conditions as discussed in Chapter 6.2. By first considering the local maximum hardness peaks, KK5 is observed to have lower number density and coarser precipitates than both KK6 and KK7 according to Table 5.3 which explains why KK5 has lowest value of Vickers hardness as discussed earlier. However, the observed differences in the microstructures for KK6 and KK7 do not explain why these have approximately the same value of Vickers hardness. The relation between hardness and volume fraction is not observed at all due to the presence of post-β" precipitates as discussed in Chapter 6.1.

The KK5 alloy was also investigated for a condition at a shorter artificial ageing time (called KK5 BP) which represents a lower value of Vickers hardness, thus before the local maximum hardness peak in the hardness curve for KK5. This additional condition was investigated for comparison of the microstructure at the local maximum hardness peaks with the general overaged condition in order to find out why these local peaks are observed. An extra condition for KK6 and KK7 was not investigated due to the fact that all three alloys show these local peaks, so it is reasonable to believe that the cause of these peaks are the same for all three alloys. From Table 5.3 one may observe that KK5 BP, which has the lowest Vickers hardness, fits the microstructural relationships described as discussed earlier by having a lower number density and coarser precipitates than KK5. KK5 BP should have a lower volume fraction due to its lower Vickers hardness (Chapter 6.1), but this is not observed (Table 5.3).

Figure 5.15 in Chapter 5.3.1 present the needle length distribution at the local maximum hardness peaks after artificial ageing at 250 °C. All the four overaged conditions show a broad distribution indicating different type of precipitates (Chapter 6.1). Still, KK6 seems to have a bit more narrow distribution than the other alloys (Figure 5.15). By using the number density

chart in Figure 5.17 in Chapter 5.3.2, one may observe the amount of the different precipitates which also is given in percent in Table A.14 in Appendix A. Since all the overaged conditions are observed to contain several different precipitates without any of them in a particular large excess, the broad needle distributions are confirmed for all the overaged alloys (Chapter 6.1). The fact that the needle length distribution of KK6 is a bit more narrow is probably due to the fact that this alloy is observed to have an amount of β" precipitates of about 50 % which represents a small excess larger than observed for the other overaged alloys. The β" precipitates represent the greatest contribution to the alloy hardness, and the U2 and B' precipitates give a greater hardness than the U1 and β' precipitates due to an additional hardening effect as discussed in Chapter 6.1 and 6.2, respectively. Thus, by first considering the local maximum hardness peaks, zero amount of β" precipitates seem to explain the lower hardness in KK5 (Figure 5.17). The amount of β" precipitates is higher in KK6 than in KK7, but the amount of U2 is higher in KK7 than in KK6. In addition, KK6 contains more β' precipitates which give less hardness, and the total amount of the β" and U2 precipitates is about 77 % for KK6 and about 67 % for KK7. This might explain why KK6 and KK7 have about the same value of Vickers hardness (Chapter 6.2). For this condition, β' precipitates have been transformed into other post-β" precipitates like U1, U2 and B' for both KK5 and KK7 which indicates a larger degree of overageing than for maximum hardness at the same temperature. KK6 still show less degree of overageing than KK5 and KK7. The amount of the disordered precipitates also indicates that overaging has occurred.

By comparing KK5 and KK5 BP, one may observe that the amount of the different precipitates present is approximately the same (Figure 5.17). The small differences observed might as well be a measurement error. Therefore, the observed differences in hardness between the local maximum hardness peaks and the general overaged condition are purely explained in terms of microstructural quantities like precipitate size, number density and volume fraction. The reason for the sudden change in these quantities is not clarified. However, all the alloys in the ageing time region including these conditions were heat treated together, so the observed local maximum hardness peaks might just be due to a mistake in the heating procedure. These conditions should be remade before substituting the old hardness values with new measured values. If the overaged part of the curve now has a straight decreasing slope, a mistake was made during the heat treatment. If the same results show up, this aspect will need further investigation.

The results from the analysis of the different precipitates present at the local maximum hardness peaks after artificial ageing at 200 °C show that these contribute differently to the hardness. Since the relative values in the number density also represent the relative amount of the different precipitates present, both number density (Figure 5.17) and volume fraction (Figure 5.16) is connected to the percentage amount (Table A.14) as stated in Chapter 6.1. The result of this is that type of precipitates with large volume fractions and number densities will contribute strongly to the hardening. As already seen for the two other conditions, the total number density and volume fraction do not show this relation in the same way as discussed in Chapter 6.1. The needle cross section area for each of the precipitates present is shown in Figure 5.18 in Chapter 5.3.2. The β' precipitates still have some of the largest cross sections and therefore contribute less to the hardness than many of the other precipitates given that these are harder than the β' precipitates as discussed in Chapter 6.1. Other overall trends are hard to spot due to the large differences between the three alloys. However, the partly disordered precipitates seem to get a cross section between the disordered and each of the ordered precipitates as discussed in Chapter 6.2.

By comparing KK5 and KK5 BP, it is seen that the cross section area of β" and the ordered U1 precipitates are larger, and that ordered U2, disordered U1 and B' precipitates are a bit smaller in KK5 BP. In addition, it is known from Chapter 2.3.3 that precipitates with large cross section areas in general are longer. These differences make the total average needle length larger and the total average cross section areas a bit larger in KK5 BP than in KK5 which explains why KK5 BP has a lower Vickers hardness as already discussed.

6.4. Comparison and summary of the three different conditions

The hardness curves for KK5, KK6 and KK7 obtained in the project work, and the ones obtained by SINTEF which were presented in Figures 3.4 and 3.1 in Chapter 3.3 and 3.2, respectively, show that the degree of overaging in general is increasing with increasing artificial ageing temperature. One may see that when the temperature is higher, the hardness curves will be shifted downwards and to the left, that is to lower hardness values and shorter artificial ageing times, respectively. The shorter ageing times are due to faster vacancy diffusion at higher temperatures as mentioned in Chapter 3.3, while the lower hardness is due to the formation of microstructures with different precipitate quantities like size, number

density and volume fraction, and that these precipitates are of different structural types as discussed in Chapter 6.1. This behavior is observed for all three alloys in Figures 3.1 and 3.4. The difference between the KK5, KK6 and KK7 alloys is their solute ratio Si/Mg given in Table 4.1 in Chapter 4.1.1 with KK5 as Mg-rich, KK6 as Si-rich and KK7 as an intermediate. The relationship between Si/Mg ratio and the Vickers hardness was discussed in Chapter 6.1 and can easily be seen from the hardness curves for artificial ageing at 200 °C (Figure 3.4) where KK5 has the lowest value of Vickers hardness, while KK6 clearly is the hardest alloy. This phenomenon is hard to see for both the artificial ageing at 250 °C and the overaged condition at 200 °C as discussed in Chapter 6.2 and 6.3, respectively, and may only be partly seen for artificial ageing at 175 °C (Figure 3.1).

An overview of the Vickers hardness values obtained for the different conditions is given in Figure 6.1. It is observed that the Vickers hardness is generally higher for maximum hardness after artificial ageing at 200 °C compared to at 250 °C. The local hardness peaks observed at overaged conditions after artificial ageing at 200 °C seem to obtain an average Vickers hardness in between the two maximum hardness conditions. In addition, KK5 has a higher Vickers hardness than KK5 BP at overaged conditions.

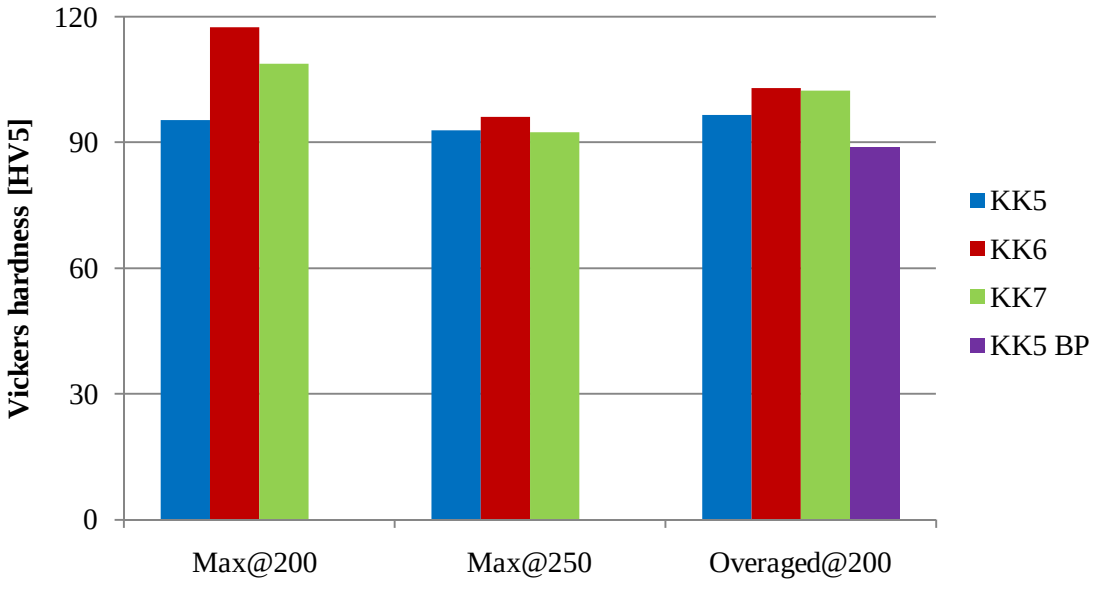

Figure 6.1: Vickers hardness for the three different artificial aging conditions

Microstructural quantities like precipitate size, number density and volume fraction strongly reflect the characteristic hardness values for KK5, KK6 and KK7 at the different artificial ageing conditions. A comparison of the needle length and cross section area for the different conditions is given in Figures 6.2 and 6.3, respectively. These show that both the average needle length and cross section area in general are smaller at 200 °C than at 250 °C. The microstructure at overaged conditions is characterized by a precipitate size between the maximum conditions. Thus, it looks like the observed differences in Vickers hardness for the three ageing conditions fits the fact that the hardness of an alloy increase with decreasing precipitate size as discussed in Chapter 6.1.

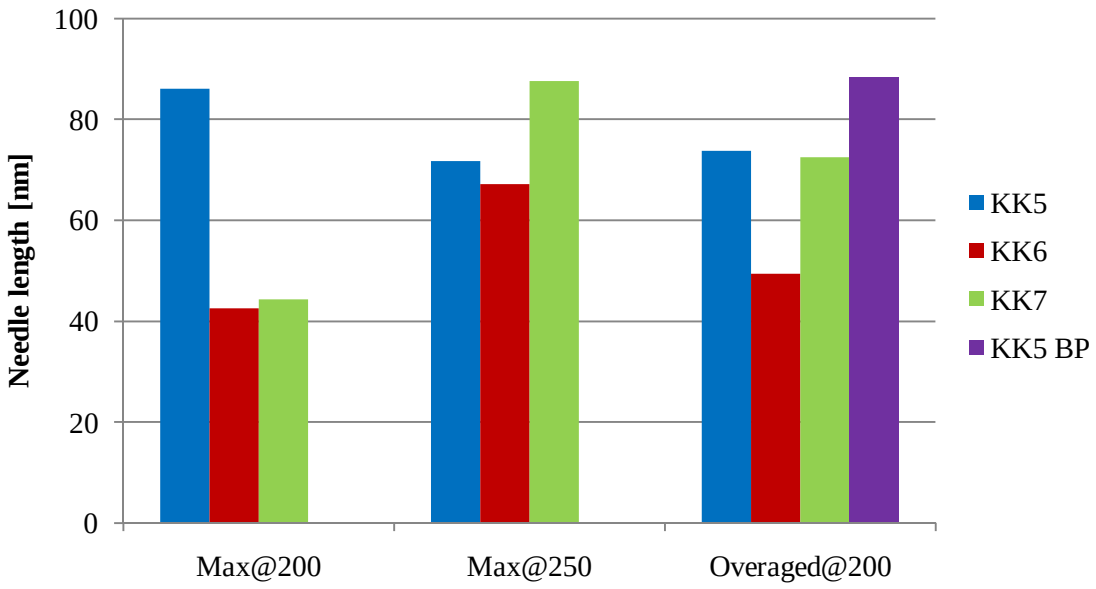

Figure 6.2: Average needle length for the three different artificial aging conditions

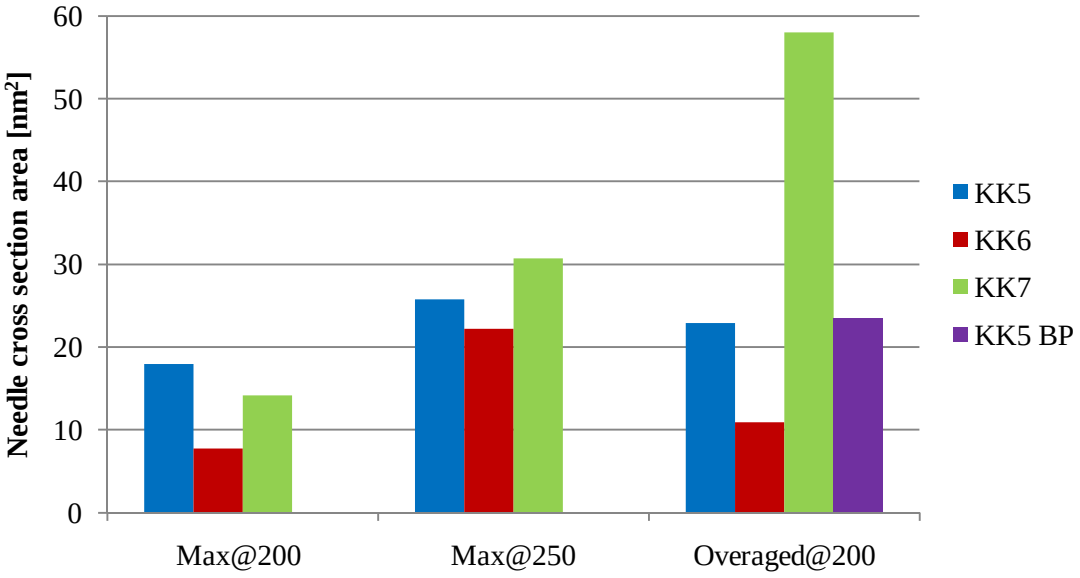

Figure 6.3: Average needle cross section area for the three different artificial aging conditions

As discussed in Chapter 6.1, the hardness of an alloy increases with increasing number density. The number density for all three conditions is given in Figure 6.4 for KK5, KK6 and KK7 where one may observe that the number density is considerably higher for the 200 °C case than for the 250 °C case, while the overaged conditions again obtains an intermediate value. Thus, the number density also contributes to the observed hardness differences.

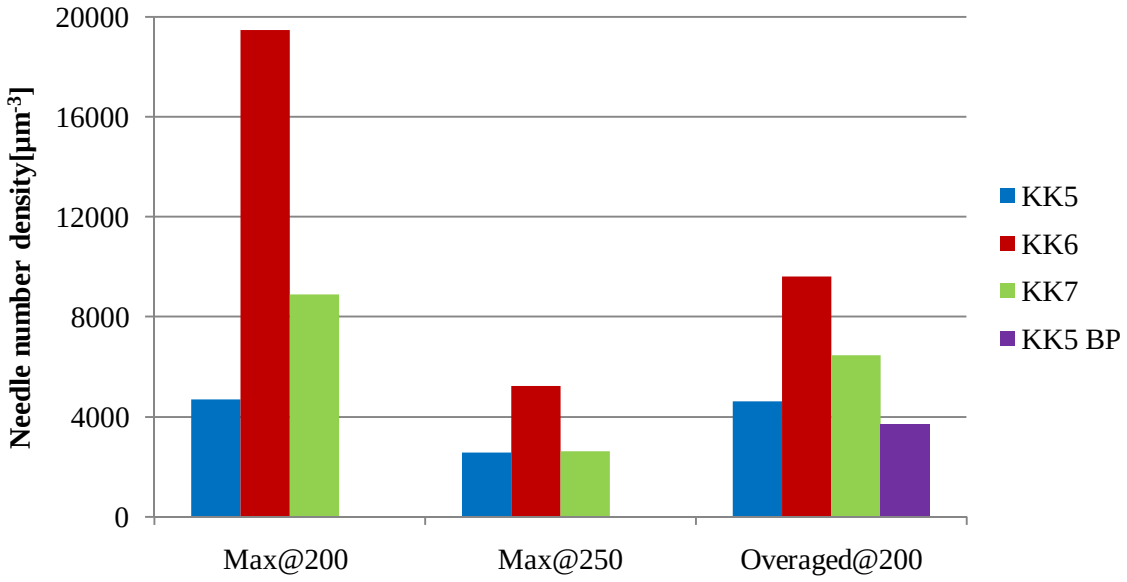

Figure 6.4: Average needle number density for the three different artificial aging conditions

By comparing the volume fractions given Figure 6.5, one may observe that volume fraction is almost identical for the maximum conditions when an average value is used for the different alloys. Due to a high volume fraction of KK7 at overaged conditions, the average volume fraction at overaged conditions is higher than for the maximum conditions. However, no relationship between the volume fraction and the Vickers hardness for the different conditions is observed due to the presence of post-β" precipitates in the same way as discussed in Chapter 6.1.

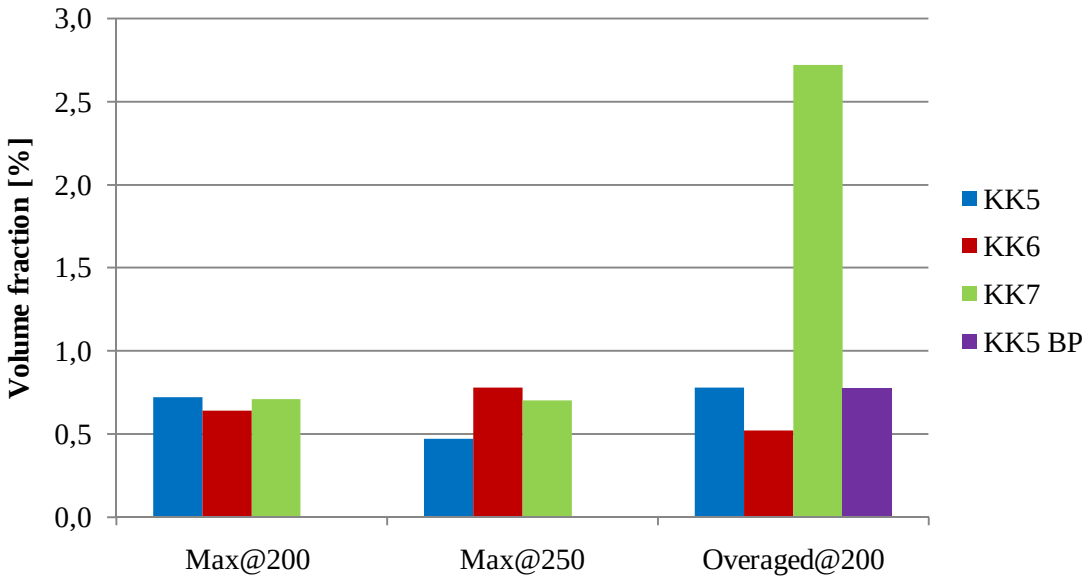

Figure 6.5: Average volume fraction for the three different artificial aging conditions

The needle length distribution is most narrow for maximum hardness after artificial ageing at 200 °C and broadest for maximum hardness after artificial ageing at 250 °C as seen from Figures 5.3 and 5.9 in Chapter 5.1.1 and 5.2.1, respectively. The overaged conditions obtain a distribution in between these two as seen in Figure 5.15 in Chapter 5.3.1 due to the different precipitates present and the amount of them as discussed in Chapter 6.1. This also shows that the degree of overageing is highest for maximum hardness at 250 °C and lowest for maximum hardness at 200 °C. As earlier discussed, different precipitates present contribute differently to the observed Vickers hardness. From Chapter 2.3.1 and 2.3.3 it is known that the type of precipitates present at overaged conditions contribute less to the hardness due to both their atomic structure, and microstructural quantities caused by precipitate growth and agglomeration. By referring to Figures 5.5, 5.11 and 5.17 in Chapter 5.1.2, 5.2.2 and 5.3.2, respectively, it can be seen that the degree of overageing is small for maximum hardness after artificial ageing at 200 °C due to small amounts of post-β" precipitates. The 250 °C case show

strong overageing due to large amounts of post-β" precipitates, while the overaged conditions obtain an intermediate position as usual. As discussed in Chapter 6.1, the degree of overageing and thus the amount of post-β" precipitates is related to the observed differences in Vickers hardness between the three ageing conditions.

Before a general discussion of each type of precipitate present, the strengthening model might be decided by plotting the results from the Vickers hardness measurements as a function of Equations 3.1 and 3.2 for all the alloys and conditions in the same way as described in Chapter 3.2. These plots are given in Figures 6.6 (a) and (b), respectively, where r_s and r_r represent the average cross sectional radius of the precipitates based on a circular shape.

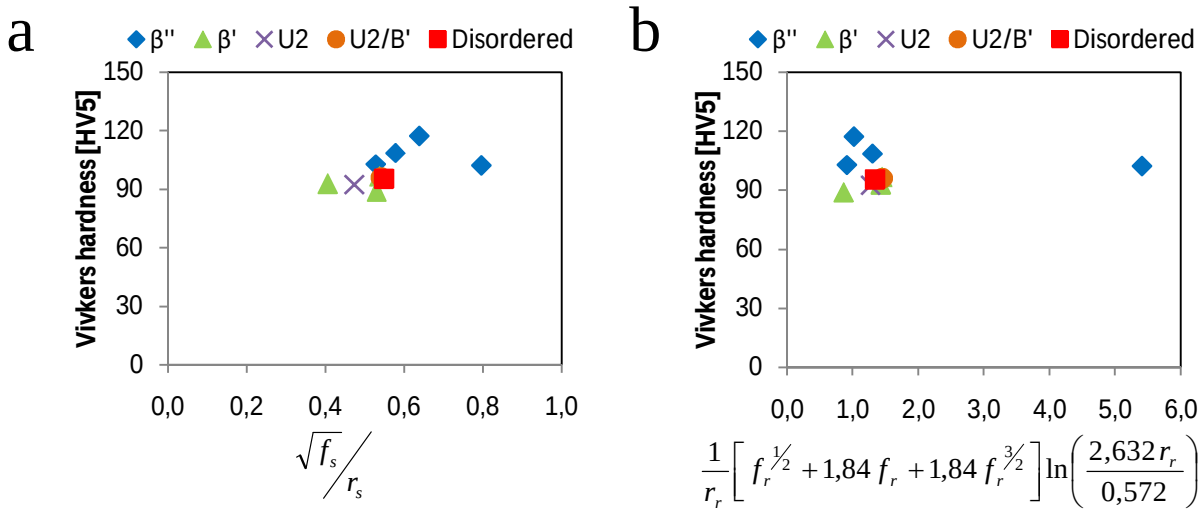

Figure 6.6: Vickers hardness as a function of (a) Equation 3.1 and (b) Equation 3.2

The relation between hardness and Equation 3.1 in Figure 6.6 (a) show a linear relationship. No correlation is observed for the relation between hardness and Equation 3.2 given in Figure 6.6 (b). Thus, it is reasonable to presume that the strengthening model for the assumed non-shareable precipitates is based on spherical precipitates even though they are observed to be needle or lath shaped in the same way as in Chapter 3.2. By referring to Chapter 2.3.2, one may observe that both Equations 3.1 and 3.2 are based on the general equation for bypassing stress given in Equation 2.4. Thus, the precipitates belong to the bypassing region in the right part of Figure 2.13 in Chapter 2.3.2.

The analysis of each type of precipitate present in the different conditions is quite complex. However, by plotting the results in the same way as done in [46] which were presented in Figures 3.2 (a)-(d) in Chapter 3.2, some trends might be observed. The plots of volume fraction, number density, cross section area and length of the needle precipitates for the conditions in the master thesis are given in Figures 6.7 (a)-(d). No clear relation is observed between Vickers hardness and volume fraction in Figure 6.7 (a) which is known to be due to the presence of large amounts of post-β" precipitates, while the number densities in Figure 6.7 (b) show almost a linear increment in hardness with increasing number density for all different type of precipitates as discussed in Chapter 6.1. In addition, it seems to be a relationship between number density, volume fraction (given in Chapter 5.1.2, 5.2.2 and 5.3.2) and amount in percent given in Tables A.12-14 in Appendix A of the precipitates for each condition in a similar way as discussed in Chapter 6.1. This is true for all the alloys and conditions. A linear decrease in hardness is seen with increasing precipitate cross section area and length as shown in Figures 6.7 (c) and (d), respectively. The β" precipitates seem to obtain the smallest needle cross section areas and lengths for all the conditions in general, while the β' precipitates tend to be coarse. Partly disordered precipitates will get a cross sections between the disordered and each of the ordered precipitates as discussed in Chapter 6.2. Summed up, the β" precipitates are generally observed to be the finest precipitates in addition to have a large number density. Thus, the β" precipitates contribute strongly to the Vickers hardness through quantities like size, volume fraction and number density.

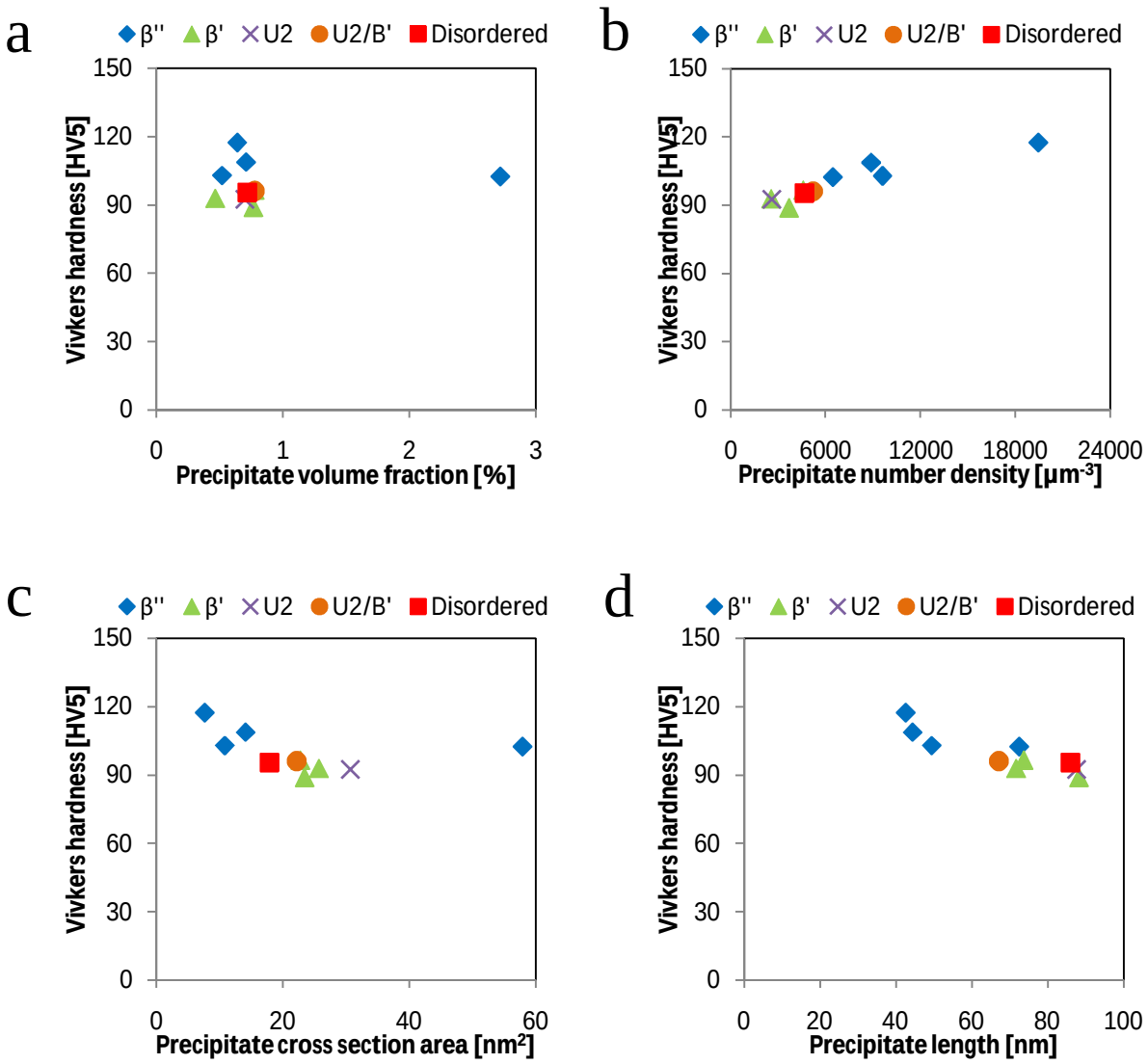

Figure 6.7: Vickers hardness as a function of (a) volume fraction, (b) number density, (c) cross section area and (d) length of hardening precipitates

7. Conclusions

- Some general trends have been observed which are valid for KK5, KK6 and KK7 at all three aging conditions:
  - Higher artificial ageing temperature increase the degree of overaging which means that the hardness curves is shifted towards shorter ageing times and lower values of Vickers hardness.
  - Mg-rich alloys (KK5) overage faster than Si-rich alloys (KK6), while alloys containing both Mg and Si (KK7) show a medium degree of overaging.
  - High number densities and fine precipitates give higher alloy hardness, while low number densities and coarse precipitates give lower alloy hardness. The volume fractions do not follow the expected trend for any conditions due to the presence of post-β" precipitates.
  - The relative amount of different type of precipitates present in KK5, KK6 and KK7 reflect the degree of overaging and thus contribute to the observed differences in Vickers hardness.
  - The different precipitates present in the three alloys at each condition contribute differently to the hardening effect through microstructural quantities like size, number density and volume fraction.
  - At higher degrees of overaging, the alloy hardness is influenced less by the different precipitates present and the relative amount of them, and more by the precipitate size and number density.
  - The strengthening model for the assumed non-shareable precipitates is based on spherical precipitates even though they are observed to be needle or lath shaped.

- Maximum hardness after artificial ageing at 200 °C has been observed to be quite different for KK5, KK6 and KK7. This is due to large differences in degree of overaging, that is differences in the type and relative amount of precipitates present, and the size and number density of these. KK6, which has the highest hardness, is characterized by small precipitates, a high number density and a large amount of β" precipitates, while KK5 with the lowest hardness has large precipitates, a low number density and a small amount of β" precipitates. KK7 has values in between. Influence from both type and relative amount of precipitates, and precipitate size and number density seem important to the hardness at this condition.

- Maximum hardness after artificial ageing at 250 °C has been found to be very similar and at a lower quantity than at maximum hardness after artificial at 200 °C for KK5, KK6 and KK7. The reason for this is that all three alloys show great overaging which is reflected in the larger amount of post-β" precipitates and the coarser microstructure. KK6 still has the highest hardness which is explained by the large amount of β", U2 and B' precipitates, in addition to having small precipitates and high number densities. KK5 and KK7 were observed to have approximately the same Vickers hardness due to considerably similarities in precipitate size and number density. The precipitates present in KK5 and KK7 are somewhat different, but the total amount of precipitates contributing in higher and lower degrees is quite similar. Therefore, the influence by the type and relative amount of different precipitates seem less important for the hardness than precipitate size and number density at this condition.

- Local maximum hardness peaks at overaged conditions after artificial ageing at 200 °C were also observed to have about the same values at a level between the two maximum hardness conditions mentioned above. This is connected to an intermediate degree of overaging which is reflected in the microstructure and in less degree in the number of post-β" precipitates compared to the two other conditions. The reason for these local maximum hardness peaks at overaged conditions is purely due to microstructural quantities like precipitate size, number density and volume fraction. However, an explanation for these sudden changes was not clarified, but this might have been caused by a mistake in the heating procedure. KK5 was observed to have coarser precipitates and a lower number density than KK6 and KK7 which explains its lower Vickers hardness. KK6 has finer precipitates and a higher number density than KK7, but their hardness values are approximately the same which is explained by the fact that the total amount of the precipitates contributing in higher and lower degrees is quite similar. Therefore, the type and relative amount of different precipitates seem a bit more important to the Vickers hardness for this condition than for the maximum hardness condition at 250 °C, but less important compared to the maximum hardness condition at 200 °C. However, the precipitate size and number density seem in general to be most important for the hardness at this condition.

8. Literature cited

1. Hu, R., T. Ogura, H. Tezuka, T. Sato, and Q. Liu, *Dispersoid Formation and recrystallization Behavior in an Al-Mg-Si-Mn Alloy.* Journal of Materials Science & Technology, 2010. **26**(3): p. 237-243.

2. Murayama, M. and K. Hono, *Pre-Preprecipitation Clusters And Precipitation Processes In Al-Mg-Si Alloys.* Acta Materialia, 1999. **47**(5): p. 1537-1548.

3. Polmear, I., *Light Alloys: From Traditional Alloys to Nanocrystals.* Vol. 4. 2005: Butterworth-Heinemann. p. 43-70, 109-115, 131-132, 138-142.

4. Ryen, Ø.J., *Work hardening of Al-Mg-Si alloys.* DMSE Report, 2005.

5. Chakrabarti, D.J. and D.E. Laughlin, *Phase relations and precipitation in Al-Mg-Si alloys with Cu addition.* Progress in Materials Science, 2004. **49**(3-4): p. 389-410.

6. Gulbrandsen-Dahl, S., K.O. Pedersen, C. Marioara, M. Kolar, and K. Marthinsen, *Mechanical characteristics of post-β'' precipitates in Al-Mg-Si alloy*, in *Aluminium Alloys. Their Physical and Mechanical Properties.* 2008, Wiley-VCH: Weinheim, Germany. p. 1634-1640.

7. Røyset, J., *Kimdanningskontroll for optimaliserte egenskaper*. 2006.

8. Solberg, J.K., *Teknologiske metaller og legeringer*. 2008: Institutt for materialteknologi, NTNU. p. 185, 200-209, 215-218.

9. *aluMATTER.* [cited 2010 08.26]; Available from: http://aluminium.matter.org.uk.

10. Andersen, S.J., H.W. Zandbergen, J. Jansen, C. Træholt, U. Tundal, and O. Reiso, *The crystal structure of the β'' phase in Al–Mg–Si alloys.* Acta Materialia, 1998. **46**(9): p. 3283-3298.

11. Callister, W.D.J., *Materials Science and Engineering: An Introduction*. Vol. 7. 2007: John Wiley & Sons, Inc. p. 40-63, 155-160, 383-384.

12. Marioara, C.D., H. Nordmark, S.J. Andersen, and R. Holmestad, *Post-β'' phases and their influence on microstructure and hardness in 6xxx Al-Mg-Si alloys.* Journal of Material Science, 2006. **41**: p. 471-478.

13. Reiso, O., *Extrusion of AlMgSi Alloys.* MATERIALS FORUM, 2004. **28**: p. 32-46.

14. Bauser, M., G. Sauer, and K. Siegert, *Extrusion*. Vol. 2. 2006: ASM International. p. 224-225.

15. Loukus, A., G. Subhash, and M. Imaninejad, *Mechanical properties and microstructural characterization of extrusion welds in AA6082-T4.* Journal of Materials Science & Technology, 2004. **39**: p. 6561 – 6569.

16. Marthinsen, K., *Diffusional transformations in solids*, Lecture notes, NTNU.

17. Holt, R., *Age (precipitation) hardening*, Lecture notes, Queen's University.

18. Marioara, C.D., S.J. Andersen, J. Jansen, and H.W. Zandbergen, *The influence of temperature and storage time at RT on nucleation of the β'' phase in a 6082 Al–Mg–Si alloy.* Acta Materialia, 2003. **51**(3): p. 789-796.

19. Porter, D.A., *Phase transformations in metals and alloys*. Vol. 3. 2009: CRC Press. p. 137-140, 276-284, 288-290.

20. Gulbrandsen-Dahl, S., *Private communication*, SINTEF Raufoss Manufacturing AS.

21. Gottstein, G., *Physical Foundations of Material Science* Vol. 1. 2004: Springer. p. 271-278.

22. Marthinsen, K., *Strengthening Mechanisms in Aluminium Alloys*, Lecture notes, NTNU.

23. Caillard, D. and J.L. Martin, *Thermally Activated Mechanisms in Crystal Plasticity*, ed. R.W. Chan. 2003: Elsevier Science. p. 281-282.

24. Putnis, A., *An Introduction to Mineral Sciences.* 1992: Cambridge University Press. p. 196.

25. Andersen, S.J., C.D. Marioara, R. Vissers, A. Frøseth, and Z.H. W., *The structural relation between precipitates in Al–Mg–Si alloys, the Al-matrix and diamond silicon, with emphasis on the trigonal phase U1-MgAl2Si2.* Materials Science and Engineering A, 2007. **444**: p. 157-169.

26. Vissers, R., M.A. van Huis, J. Jansen, H.W. Zandbergen, C.D. Marioara, and S.J. Andersen, *The crystal structure of the β' phase in Al–Mg–Si alloys.* Acta Materialia 2007. **55**(11): p. 3815-3823.

27. Andersen, S.J., C.D. Marioara, A. Frøseth, R. Vissers, and H.W. Zandbergen, *Crystal structure of the orthorhombic U2-Al4Mg4Si4 precipitate in the Al–Mg–Si alloy system and its relation to the β' and β'' phases.* Materials Science and Engineering A, 2005. **390**(1-2): p. 127-138.

28. Vissers, R., C.D. Marioara, S.J. Andersen, and R. Holmestad, *Crystal structure determination of the B' phase in Al-Mg-Si alloys by combining quantitative electron diffraction and ab initio calculations,* in *Aluminium Alloys. Their Physical and Mechanical Properties*. 2008, Wiley-VCH: Weinheim, Germany. p. 1263-1269.

29. Marioara, C.D., *Private communication*, SINTEF Materialer og Kjemi.

30. Marioara, C.D., S.J. Andersen, H.W. Zandbergen, and R. Holmestad, *The Influence of Alloy Composition on Precipitates of the Al-Mg-Si System.* Metallurgical and Materials Transactions A, 2005. **36**(3): p. 691-702.

31. *Electrical Conductivity and Resistivity*. [cited 2010 09.06]; Available from: http://www.ndt-ed.org/EducationResources/CommunityCollege/Materials/Physical_Chemical/Electrical.htm.

32. Småbråten, H.K., *Characterization of pecipitates at maximum hardness in Al-Mg-Si alloys*. 2010, Unpublished work, NTNU.

33. Solberg, J.K., *Lysmikroskopi*. 2006: Institutt for materialteknologi, NTNU. p. 8.

34. Solberg, J.K. and V. Hansen, *Innføring i transmisjons elektronmikroskopi*. 2007: Institutt for materialteknologi, NTNU. p. 5-12, 27-35, 39.

35. *Maurice Wilkins Centre*. [cited 2010 08.31]; Available from: http://www.mauricewilkinscentre.org/bioviz/forstudents/pharmacy751/2.jpg.

36. *The Transmission Electron Microscope*. [cited 2010 08.31]; Available from: http://nobelprize.org/educational/physics/microscopes/tem/index.html.

37. *Transmission Electron Microscopy (TEM)*. [cited 2010 08.31]; Available from: http://www.miplaza.com/materialsanalysis/projects/technicalnotessurfaceandthinfilmanalysis/temtn.pdf.

38. Spence, J.C.H., *High-Resolution Electron Microscopy (Monographs on the Physics and Chemistry of Materials)*. 2008: Oxford University Press, USA. p. 156-159.

39. *Pythagorean Theorem*. [cited 2011 01.25]; Available from: http://mathworld.wolfram.com/PythagoreanTheorem.html.

40. Yu, Y., *Kikuchi Line Map*, Unpublished work, NTNU.

41. Buddington, A., *Analyzing the thickness of a TEM sample using EELS and integration techniques*, Lecture notes, Princeton University.

42. *DigitalMicrograph EELS Analysis User's Guide*. 2003, Unpublished work.

43. *Fourier Transform*. [cited 2011 05.10]; Available from: http://homepages.inf.ed.ac.uk/rbf/HIPR2/freqfilt.htm.

44. *Frequency Filter*. [cited 2011 05.10]; Available from: http://homepages.inf.ed.ac.uk/rbf/HIPR2/freqfilt.htm.

45. Marioara, C.D., S.J. Andersen, and B. Holme, *Methodology for Quantification of Needle Precipitates in 6xxx Al-Mg-Si(-Cu) Alloys*, Unpublished work, SINTEF Materialer og Kjemi.

46. Gulbrandsen-Dahl, S., C.D. Marioara, K.O. Pedersen, and K. Marthinsen, *Hardening of Al-Mg-Si alloys and effect of particle structure*. To be published at THERMEC'2012.

47. Marioara, C.D., S.J. Andersen, T.N. Stene, H. Hasting, J. Walmsley, A.T.J. Van Helvoort, and R. Holmestad, *The effect of Cu on precipitation in Al–Mg–Si alloys.* Philosophical Magazine, 2007. **87**(23): p. 3385–3413.

48. *Material Safety Data Sheet.* [cited 2010 10.19]; Available from: http://msds.chem.ox.ac.uk/#MSDS.

49. *TEM sample preparation guide*. [cited 2010 10.26]; Available from: http://temsamprep.in2p3.fr/techniques.php?lang=eng.

50. *TenuPol-5*. [cited 2010 10.26]; Available from: http://struers.com/resources/elements/12/103090/TenuPol-5%20brochure%20English.pdf.

51. *Fischione Model 1010 Ion Mill Standard Magnification Version Instruction manual*, Unpublished work.

52. *Fischione Instruments*. [cited 2011 05.10]; Available from: http://www.fischione.com/products/model_1010.asp.

53. *Fischione Model 1020 Plasma Cleaner Instruction Manual*, Unpublished work.

54. Teichmann, K., *Private communication*, NTNU.

55. Walpole, R.E., R.H. Myers, S.L. Myers, and K. Ye, *Probability & Statistics for Engineers & Scientists*. Vol. 8. 2007: Dorling Kindersley. p. 25, 39-40.

Appendix A: Experimental data

Table A.1: Ageing procedure, Vickers hardness and electrical conductivity for KK5, 200 °C

Sample no.	Time [min]	Time [hh:mm]	Conduc-tivity [m/Ωmm^2]	Hardness [HV5]						
				1	2	3	4	5	AVG	SD
1	1	00:01	23,5	73,0	77,1	75,8	80,5	79,3	77,1	2,6
2	20	00:20	24,3	86,5	84,6	86,2	80,9	82,7	84,2	2,1
3	40	00:40	24,6	95,3	94,4	89,5	86,5	87,4	90,6	3,6
4	60	01:00	25,5	94,6	92,0	95,3	89,7	95,3	93,4	2,2
5	80	01:20	25,9	90,3	100,0	94,9	94,7	91,7	94,3	3,3
6	100	01:40	26,3	94,4	93,0	99,9	95,6	94,2	95,4	2,4
7	120	02:00	25,9	94,7	92,3	92,6	93,2	94,0	93,4	0,9
8	140	02:20	26,0	90,0	87,9	89,5	91,2	95,3	90,8	2,5
9	160	02:40	26,2	81,7	92,3	94,0	89,8	92,3	90,0	4,4
10	180	03:00	26,3	91,5	95,9	87,3	90,0	90,6	91,1	2,8
11	210	03:30	26,2	90,6	91,2	90,9	91,4	88,9	90,6	0,9
12	240	04:00	26,2	89,0	91,4	92,3	87,5	91,7	90,4	1,8
13	270	04:30	26,2	88,4	88,1	90,3	92,0	93,3	90,4	2,0
14	300	05:00	26,3	88,1	88,6	87,0	89,4	88,4	88,3	0,8
15	330	05:30	26,3	93,1	89,2	93,7	94,1	87,3	91,5	2,7
16	360	06:00	27,0	87,3	86,5	90,0	88,6	92,3	88,9	2,1
17	420	07:00	27,2	91,1	88,3	87,8	88,4	93,2	89,8	2,1
18	480	08:00	29,6	92,3	93,5	91,4	93,2	96,0	93,3	1,5
19	600	10:00	29,6	97,7	96,2	96,4	93,2	99,7	96,6	2,1
20	720	12:00	29,6	93,5	90,6	89,5	88,7	90,9	90,6	1,6
21	840	14:00	29,7	92,0	84,4	84,4	89,0	85,2	87,0	3,0
22	1020	17:00	29,3	84,9	90,6	89,7	90,3	95,9	90,3	3,5
23	1440	24:00	29,6	86,2	81,9	81,7	84,1	86,7	84,1	2,1

Table A.2: Ageing procedure, Vickers hardness and electrical conductivity for KK6, 200 °C

Sample no.	Time [min]	Time [hh:mm]	Conduc-tivity [m/Ωmm^2]	Hardness [HV5]						
				1	2	3	4	5	AVG	SD
1	1	00:01	23,4	82,4	83,4	76,8	77,7	85,4	81,1	3,3
2	20	00:20	24,7	101,5	93,4	96,5	92,8	99,4	96,7	3,4
3	40	00:40	25,5	120,0	111,5	115,0	115,0	116,5	115,6	2,7
4	60	01:00	26,6	121,7	118,5	115,0	116,0	116,0	117,4	2,4
5	80	01:20	26,8	119,5	117,5	115,0	118,0	113,5	116,7	2,2
6	100	01:40	26,6	115,0	118,0	112,5	111,5	106,5	112,7	3,8
7	120	02:00	26,7	115,5	114,0	113,0	109,5	113,0	113,0	2,0
8	140	02:20	26,7	106,5	114,0	113,0	113,0	110,5	111,4	2,7
9	160	02:40	26,8	114,0	109,5	110,5	115,5	116,0	113,1	2,6
10	180	03:00	27,0	105,0	105,0	105,0	107,0	105,5	105,5	0,8
11	210	03:30	27,0	107,0	101,7	110,0	105,5	105,5	105,9	2,7
12	240	04:00	27,1	108,0	106,5	107,0	111,0	104,5	107,4	2,1
13	270	04:30	27,2	102,5	104,5	105,5	105,5	101,5	103,9	1,6
14	300	05:00	27,2	105,5	103,0	105,5	102,0	99,5	103,1	2,3
15	330	05:30	27,2	103,0	100,5	101,3	105,5	102,4	102,5	1,7
16	360	06:00	27,3	102,0	102,5	103,5	99,1	101,4	101,7	1,5
17	420	07:00	28,1	98,6	99,4	101,2	101,5	99,5	100,0	1,1
18	480	08:00	28,5	103,0	95,1	101,9	96,8	103,0	100,0	3,3
19	600	10:00	28,4	101,5	105,5	105	100,1	102,6	102,9	2,1
20	720	12:00	28,4	90,6	93,8	89,2	94,3	90,3	91,6	2,0
21	840	14:00	28,4	84,9	94,7	88,4	91,5	90,9	90,1	3,3
22	1020	17:00	28,4	92,4	93,2	96,5	88,6	91,2	92,4	2,6
23	1440	24:00	29,1	87,0	85,0	83,1	88,3	90,9	86,9	2,7

Table A.3: Ageing procedure, Vickers hardness and electrical conductivity for KK7, 200 °C

Sample no.	Time [min]	Time [hh:mm]	Conduc-tivity [m/Ωmm^2]	Hardness [HV5]						
				1	2	3	4	5	AVG	SD
1	1	00:01	23,7	79,8	80,5	81,0	82,1	79,8	80,6	0,9
2	20	00:20	24,8	90,1	91,7	90,0	90,1	90,6	90,5	0,6
3	40	00:40	25,5	104,0	102,7	102,0	100,7	101,9	102,3	1,1
4	60	01:00	26,4	109,5	107,5	109,0	108,5	109,0	108,7	0,7
5	80	01:20	26,8	109,5	107,5	108,0	107,0	110,0	108,4	1,2
6	100	01:40	26,7	104,5	108,0	107,0	107,0	104,5	106,2	1,4
7	120	02:00	27,0	103,5	103,5	104,0	107,5	108,0	105,3	2,0
8	140	02:20	27,8	105,0	105,0	102,5	97,7	101,5	102,3	2,7
9	160	02:40	27,8	100,5	104,4	106,5	106,0	100,3	103,5	2,7
10	180	03:00	27,9	101,3	98,4	98,0	100,0	105,0	100,5	2,5
11	210	03:30	28,0	102,0	99,2	98,6	95,9	99,5	99,0	2,0
12	240	04:00	28,0	101,4	97,4	101,0	97,8	97,1	98,9	1,9
13	270	04:30	28,1	98,1	101,5	101,9	98,1	100,2	100,0	1,6
14	300	05:00	27,8	101,5	97,3	95,6	97,7	95,0	97,4	2,3
15	330	05:30	28,4	90,0	96,2	96,2	96,7	98,1	95,4	2,8
16	360	06:00	28,2	94,3	92,9	92,6	92,3	90,0	92,4	1,4
17	420	07:00	28,6	104,5	103,5	103,4	101,9	98,6	102,4	2,1
18	480	08:00	28,6	96,2	99,2	98,4	96,6	97,2	97,5	1,1
19	600	10:00	28,7	86,2	84,1	83,6	83,4	84,7	84,4	1,0
20	720	12:00	28,8	84,1	82,9	84,4	84,9	86,8	84,6	1,3
21	840	14:00	28,9	88,4	87,8	87,3	88,3	87,0	87,8	0,5
22	1020	17:00	28,6	104,5	103,5	103,4	101,9	98,6	102,4	0,9
23	1440	24:00	28,6	96,2	99,2	98,4	96,6	97,2	97,5	0,6

Table A.4: Ageing procedure, Vickers hardness and electrical conductivity for KK5, 250 °C

Sample no.	Time [min]	Time [hh:mm]	Conduc-tivity [m/Ωmm^2]	Hardness [HV5]						
				1	2	3	4	5	AVG	SD
1	1	00:01	25,8	70,2	67,5	68,2	67,3	66,9	68,0	1,2
24	2	00:02	24,9	72,6	74,2	70,2	73,0	74,2	72,8	1,5
25	3	00:03	25,8	77,5	83,9	80,0	83,1	81,7	81,2	2,3
26	4	00:04	25,7	87,5	83,4	83,9	83,9	81,9	84,1	1,8
2	5	00:05	27,5	92,0	97,8	90,3	94,2	90,1	92,9	2,9
27	7	00:07	27,1	82,6	82,9	82,4	79,3	81,2	81,7	1,3
3	10	00:10	27,0	86,6	85,7	85,7	87,4	91,9	87,5	2,3
4	15	00:15	30,2	80,5	82,3	83,1	82,1	83,2	82,2	1,0
5	20	00:20	30,3	80,4	88,9	88,9	81,7	85,1	85,0	3,5
6	25	00:25	30,3	91,1	86,2	88,9	84,9	82,4	86,7	3,0
7	30	00:30	30,7	74,9	75,3	73,2	71,8	75,8	74,2	1,5
8	40	00:40	30,7	77,0	76,1	70,1	73,6	73,8	74,1	2,4
9	50	00:50	30,8	72,1	72,6	74,3	73,2	72,8	73,0	0,7
10	60	01:00	30,8	71,2	72,1	69,4	72,3	69,2	70,8	1,3
11	80	01:20	31,0	68,1	66,3	67,4	67,6	72,1	68,3	2,0
12	100	01:40	31,3	67,8	65,6	66,7	63,7	65,2	65,8	1,4
13	120	02:00	31,3	68,7	62,7	63,3	64,1	67,4	65,2	2,4
14	150	02:30	31,4	65,2	63,8	64,2	64,6	63,9	64,3	0,5
15	180	03:00	31,4	63,9	60,2	60,1	63,6	61,5	61,9	1,6
16	210	03:30	31,6	59,5	60,7	61,4	63,2	63,2	61,6	1,4
17	240	04:00	31,6	58,6	58,4	58,4	62,3	62,6	60,1	2,0
18	300	05:00	31,8	55,1	61,6	61,8	60,5	61,1	60,0	2,5
19	330	05:30	31,9	59,4	57,7	58,4	58,8	61,6	59,2	1,3
20	360	06:00	32,0	57,3	55,4	57,0	58,6	55,9	56,8	1,1
21	390	06:30	30,9	59,3	58,3	56,5	57,1	55,6	57,4	1,3
22	420	07:00	31,9	58,3	57,5	57,5	57,5	56,3	57,4	0,6
23	480	08:00	32,0	53,8	55,1	56,3	56,5	56,6	55,7	1,1

Table A.5: Ageing procedure, Vickers hardness and electrical conductivity for KK6, 250 °C

Sample no.	Time [min]	Time [hh:mm]	Conduc-tivity [m/Ωmm^2]	Hardness [HV5]						
				1	2	3	4	5	AVG	SD
1	1	00:01	25,8	57,8	61,1	62,7	62,3	63,1	61,4	1,9
24	2	00:02	24,8	67,0	72,0	73,2	68,3	70,0	70,1	2,3
25	3	00:03	25,6	96,3	89,5	103,0	94,5	92,3	95,1	4,5
26	4	00:04	25,9	99,9	96,5	95,6	92,8	95,6	96,1	2,3
2	5	00:05	28,0	85,2	88,1	83,2	82,4	83,1	84,4	2,1
27	7	00:07	26,6	83,6	92,1	87,3	87,1	87,5	87,5	2,7
3	10	00:10	28,2	79,7	78,4	76,4	84,2	80,7	79,9	2,6
4	15	00:15	28,4	75,7	81,9	78,4	84,6	86,5	81,4	3,9
5	20	00:20	28,7	76,3	77,0	75,8	76,1	77,9	76,6	0,8
6	25	00:25	28,8	71,5	73,8	70,8	77,2	79,3	74,5	3,3
7	30	00:30	29,0	76,2	75,1	74,2	75,7	73,8	75,0	0,9
8	40	00:40	29,3	71,7	76,1	74,2	72,2	71,3	73,1	1,8
9	50	00:50	29,5	70,5	70,4	69,8	69,8	67,6	69,6	1,1
10	60	01:00	29,5	68,1	71,7	71,0	71,2	73,3	71,1	1,7
11	80	01:20	29,8	67,9	67,1	69,6	70,1	69,4	68,8	1,1
12	100	01:40	30,7	65,4	71,0	69,6	64,9	69,5	68,1	2,5
13	120	02:00	30,5	64,8	64,2	65,3	68,2	64,9	65,5	1,4
14	150	02:30	31,1	63,7	62,0	64,6	65,1	63,1	63,7	1,1
15	180	03:00	31,2	61,1	59,9	64,6	63,1	61,8	62,1	1,6
16	210	03:30	31,3	57,2	61,1	62,1	58,7	59,9	59,8	1,7
17	240	04:00	31,4	59,2	59,4	60,8	61,9	59,7	60,2	1,0
18	300	05:00	31,6	59,1	59,3	58,1	62,4	61,2	60,0	1,6
19	330	05:30	31,8	54,8	55,1	55,8	57,1	60,5	56,7	2,1
20	360	06:00	31,9	53,9	54,8	54,0	57,4	57,4	55,5	1,6
21	390	06:30	30,9	58,4	57,7	56,3	56,3	57,7	57,3	0,8
22	420	07:00	31,5	55,1	56,6	57,0	55,8	55,7	56,0	0,7
23	480	08:00	31,6	53,7	53,6	55,3	53,5	54,1	54,0	0,7

Table A.6: Ageing procedure, Vickers hardness and electrical conductivity for KK7, 250 °C

Sample no.	Time [min]	Time [hh:mm]	Conduc-tivity [m/Ωmm^2]	Hardness [HV5]						
				1	2	3	4	5	AVG	SD
1	1	00:01	25,0	73,8	71,9	73,6	72,1	70,4	72,4	1,2
24	2	00:02	25,0	68,2	76,6	70,0	71,4	74,7	72,2	3,1
25	3	00:03	26,0	85,1	85,5	84,7	86,8	84,1	85,2	0,9
26	4	00:04	26,4	86,6	88,9	91,4	92,0	90,9	90,0	2,0
2	5	00:05	26,4	92,6	93,4	92,0	92,7	92,0	92,5	0,5
27	7	00:07	27,4	86,7	87,7	86,5	84,7	85,3	86,2	1,1
3	10	00:10	28,3	87,5	88,6	87,8	89,7	88,1	88,3	0,8
4	15	00:15	28,5	82,7	84,4	83,4	82,6	84,9	83,6	0,9
5	20	00:20	27,8	78,0	79,4	77,7	80,7	76,4	78,4	1,5
6	25	00:25	28,2	75,2	77,3	76,8	77,4	78,6	77,1	1,1
7	30	00:30	28,3	73,4	72,0	73,8	72,8	74,0	73,2	0,7
8	40	00:40	28,4	72,4	71,0	72,8	71,3	72,3	72,0	0,7
9	50	00:50	28,6	69,3	68,9	68,7	72,8	71,3	70,2	1,6
10	60	01:00	28,3	69,4	68,5	67,4	67,9	68,0	68,2	0,7
11	80	01:20	28,7	68,1	67,7	66,7	65,8	66,6	67,0	0,8
12	100	01:40	28,7	68,9	67,4	67,5	65,8	65,6	67,0	1,2
13	120	02:00	29,2	63,8	64,3	64,8	65,8	65,8	64,9	0,8

Table A.7: Average needle length

Condition	Alloy	Average needle length [nm]
Maximum hardness at 200 °C	KK5	86,04
	KK6	42,56
	KK7	44,39
Maximum hardness at 250 °C	KK5	71,75
	KK6	67,14
	KK7	87,60
Local maximum hardness at 200 °C	KK5	73,77
	KK6	49,44
	KK7	72,54
	KK5 BP	88,31

Table A.8: Needle length distribution

Condition	Alloy	0-25 nm [#]	25-50 nm [#]	50-75 nm [#]	75-100 nm [#]	100-125 nm [#]	125+ nm [#]
Maximum hardness at 200 °C	KK5	66	214	224	161	103	178
	KK6	63	678	210	37	6	3
	KK7	87	602	206	41	12	3
Maximum hardness at 250 °C	KK5	25	276	244	160	84	73
	KK6	5	267	494	179	49	44
	KK7	16	147	229	195	94	136
Local maximum hardness at 200 °C	KK5	40	293	262	155	83	105
	KK6	80	541	289	88	31	16
	KK7	29	449	322	127	74	132
	KK5 BP	20	206	223	174	107	171

Table A.9: Total average needle cross section area

Condition	Alloy	Average needle cross section area [nm^2]
Maximum hardness at 200 °C	KK5	17,95
	KK6	7,72
	KK7	14,17
Maximum hardness at 250 °C	KK5	25,77
	KK6	22,21
	KK7	30,71
Local maximum hardness at 200 °C	KK5	22,86
	KK6	10,88
	KK7	57,96
	KK5 BP	23,51

Table A.10: Total needle number density

Condition	Alloy	Needle number density [μm^{-3}]
Maximum hardness at 200 °C	KK5	4679,81
	KK6	19480,91
	KK7	8884,74
Maximum hardness at 250 °C	KK5	2565,98
	KK6	5222,63
	KK7	2620,56
Local maximum hardness at 200 °C	KK5	4605,92
	KK6	9607,56
	KK7	6463,02
	KK5 BP	3705,11

Table A.11: Total needle volume fraction

Condition	Alloy	Needle volume fraction [%]
Maximum hardness at 200 °C	KK5	0,72
	KK6	0,64
	KK7	0,71
Maximum hardness at 250 °C	KK5	0,47
	KK6	0,78
	KK7	0,70
Local maximum hardness at 200 °C	KK5	0,78
	KK6	0,52
	KK7	2,72
	KK5 BP	0,77

Table A.12: Amount of precipitates for maximum hardness after artificial ageing at 200 °C

Presipitattype	KK5 [%]	KK6 [%]	KK7 [%]
β"	2,52	53,69	16,51
β'	1,89	-	3,30
U1	-	-	-
U2	-	-	-
B'	-	-	-
β	-	-	-
Disordered β"	3,77	30,05	37,74
Disordered β'	19,50	-	10,38
Disordered U1	-	-	-
Disordered U2	-	-	-
Disordered B'	-	-	-
Disordered β	-	-	-
Disordered	72,33	16,26	32,08

Table A.13: Amount of precipitates for maximum hardness after artificial ageing at 250 °C

Presipitattype	KK5 [%]	KK6 [%]	KK7 [%]
β"	9,55	11,03	-
β'	12,56	-	21,02
U1	-	4,78	-
U2	-	27,57	31,85
B'	-	30,88	9,55
β	-	-	-
Disordered β"	20,60	-	-
Disordered β'	31,66	-	9,55
Disordered U1	-	-	-
Disordered U2	-	8,82	10,83
Disordered B'	-	2,94	2,55
Disordered β	-	-	-
Disordered	25,63	13,97	14,65

Table A.14: Amount of precipitates for local maximum hardness after artificial ageing at 200 °C

Presipitattype	KK5 [%]	KK6 [%]	KK7 [%]	KK5 BP [%]
β"	2,26	50,67	23,92	3,38
β'	20,68	-	2,87	21,94
U1	0,75	-	-	4,22
U2	2,26	-	7,18	3,38
B'	2,26	1,78	0,96	4,64
β	-	-	-	-
Disordered β"	6,39	26,67	32,54	5,06
Disordered β'	34,21	-	6,22	31,22
Disordered U1	0,38	-	-	0,84
Disordered U2	2,63	-	3,83	2,11
Disordered B'	1,88	0,44	0,48	1,69
Disordered β	-	-	-	-
Disordered	26,32	20,44	22,01	21,52

Table A.15: Needle cross section area for each type of precipitate for maximum hardness after artificial ageing at 200 °C

Presipitattype	KK5 [nm^2]	KK6 [nm^2]	KK7 [nm^2]
β"	13,95	7,28	13,13
β'	21,10	-	17,26
U1	-	-	-
U2	-	-	-
B'	-	-	-
β	-	-	-
Disordered β"	15,79	8,09	14,36
Disordered β'	21,69	-	14,24
Disordered U1	-	-	-
Disordered U2	-	-	-
Disordered B'	-	-	-
Disordered β	-	-	-
Disordered	17,11	8,49	14,13

Table A.16: Needle cross section area for each type of precipitate for maximum hardness after artificial ageing at 250 °C

Presipitattype	KK5 [nm^2]	KK6 [nm^2]	KK7 [nm^2]
β"	24,78	23,11	-
β'	41,46	-	40,94
U1	-	28,19	-
U2	-	27,00	32,63
B'	-	15,76	17,31
β	-	-	-
Disordered β"	19,48	-	-
Disordered β'	28,52	-	29,26
Disordered U1	-	-	-
Disordered U2	-	26,72	27,42
Disordered B'	-	22,91	24,73
Disordered β	-	-	-
Disordered	20,10	21,25	25,03

Table A.17: Needle cross section area for each type of precipitate for local maximum hardness after artificial ageing at 200 °C

Presipitattype	KK5 [nm^2]	KK6 [nm^2]	KK7 [nm^2]	KK5 BP [nm^2]
β"	10,18	10,05	53,65	24,65
β'	30,83	-	143,41	28,91
U1	22,57	-	-	41,76
U2	30,76	-	51,17	26,14
B'	20,80	18,59	34,53	24,75
β	-	-	-	-
Disordered β"	21,83	12,76	56,94	29,44
Disordered β'	21,68	-	64,15	21,83
Disordered U1	16,60	-	-	14,61
Disordered U2	20,20	-	67,72	21,91
Disordered B'	19,12	21,91	79,67	11,45
Disordered β	-	-	-	-
Disordered	19,60	9,57	52,31	16,44

Table A.18: Needle number density for each type of precipitate for maximum hardness after artificial ageing at 200 °C

Presipitattype	KK5 [µm^{-3}]	KK6 [µm^{-3}]	KK7 [µm^{-3}]
β"	117,73	10460,19	1466,82
β'	88,30	-	293,36
U1	-	-	-
U2	-	-	-
B'	-	-	-
β	-	-	-
Disordered β"	176,60	5853,87	3352,73
Disordered β'	912,42	-	922,00
Disordered U1	-	-	-
Disordered U2	-	-	-
Disordered B'	-	-	-
Disordered β	-	-	-
Disordered	3384,77	3166,85	2849,82

Table A.19: Needle number density for each type of precipitate for maximum hardness after artificial ageing at 250 °C

Presipitattype	KK5 [µm^{-3}]	KK6 [µm^{-3}]	KK7 [µm^{-3}]
β"	244,99	576,02	-
β'	322,36	-	550,82
U1	-	249,61	-
U2	-	1440,06	834,57
B'	-	1612,87	250,37
β	-	-	-
Disordered β"	528,67	-	-
Disordered β'	812,35	-	250,37
Disordered U1	-	-	-
Disordered U2	-	460,82	283,76
Disordered B'	-	153,61	66,77
Disordered β	-	-	-
Disordered	657,61	729,63	383,90

Table A.20: Needle number density for each type of precipitate for local maximum hardness after artificial ageing at 200 °C

Presipitattype	KK5 [µm^{-3}]	KK6 [µm^{-3}]	KK7 [µm^{-3}]	KK5 BP [µm^{-3}]
β''	103,89	4867,83	1546,18	125,07
β'	952,35	-	185,54	812,93
U1	34,63	-	-	156,33
U2	103,89	-	463,85	125,07
B'	103,89	170,80	61,85	171,97
β	-	-	-	-
Disordered β''	294,36	2562,02	2102,80	187,60
Disordered β'	1575,71	-	402,01	1156,87
Disordered U1	17,32	-	-	31,27
Disordered U2	121,21	-	247,39	78,17
Disordered B'	86,58	42,70	30,92	62,53
Disordered β	-	-	-	-
Disordered	1212,08	1964,21	1422,48	797,30

Table A.21: Needle volume fraction for each type of precipitate for maximum hardness after artificial ageing at 200 °C

Presipitattype	KK5 [%]	KK6 [%]	KK7 [%]
β''	0,014	0,324	0,085
β'	0,016	-	0,022
U1	-	-	-
U2	-	-	-
B'	-	-	-
β	-	-	-
Disordered β''	0,024	0,201	0,214
Disordered β'	0,170	-	0,058
Disordered U1	-	-	-
Disordered U2	-	-	-
Disordered B'	-	-	-
Disordered β	-	-	-
Disordered	0,498	0,114	0,179

Table A.22: Needle volume fraction for each type of precipitate for maximum hardness after artificial ageing at 250 °C

Presipitattype	KK5 [%]	KK6 [%]	KK7 [%]
β"	0,044	0,089	-
β'	0,096	-	0,198
U1	-	0,047	-
U2	-	0,261	0,239
B'	-	0,171	0,038
β	-	-	-
Disordered β"	0,074	-	-
Disordered β'	0,166	-	0,064
Disordered U1	-	-	-
Disordered U2	-	0,083	0,068
Disordered B'	-	0,024	0,014
Disordered β	-	-	-
Disordered	0,095	0,104	0,084

Table A.23: Needle volume fraction for each type of precipitate for local maximum hardness after artificial ageing at 200 °C

Presipitattype	KK5 [%]	KK6 [%]	KK7 [%]	KK5 BP [%]
β"	0,008	0,242	0,602	0,027
β'	0,217	-	0,193	0,208
U1	0,006	-	-	0,058
U2	0,024	-	0,172	0,029
B'	0,016	0,016	0,015	0,038
β	-	-	-	-
Disordered β"	0,047	0,162	0,869	0,049
Disordered β'	0,252	-	0,187	0,223
Disordered U1	0,002	-	-	0,004
Disordered U2	0,018	-	0,122	0,015
Disordered B'	0,012	0,005	0,018	0,006
Disordered β	-	-	-	-
Disordered	0,175	0,093	0,540	0,116

Table A.24: Image calibration data for calculation of common scale factor

Image number	Actual scalebar [nm]	Measured scalebar [mm]	Scale factor[nm/mm]
1	20	21,5	0,930232558
2	20	21,25	0,941176471
3	20	20	1
4	20	23	0,869565217
5	20	22	0,909090909
6	20	22	0,909090909
7	20	22	0,909090909
8	20	22	0,909090909
9	20	22	0,909090909
10	20	23,5	0,85106383
11	20	21	0,952380952
12	20	22	0,909090909
13	20	23	0,869565217
14	20	21,5	0,930232558
15	20	21,5	0,930232558
16	20	21,5	0,930232558
17	20	21,5	0,930232558
18	20	23	0,869565217
19	20	22	0,909090909
20	20	21	0,952380952
21	20	21	0,952380952
22	20	21	0,952380952
23	20	21	0,952380952
24	20	22,5	0,888888889
Average	-	-	**0,919438698**

Table A.25: Relative error for needle cross section, length, number density and volume fraction

Condition	Alloy	Δ<CS>/<CS>	Δ<l>/<l>	Δρ‖/ρ‖	ΔVF/VF upper	ΔVF/VF lower
Maximum hardness at 200 °C	KK5	0,476659542	0,083705863	0,119935972	0,484903723	0,491624542
	KK6	0,596236219	0,053640138	0,107873052	0,599124257	0,60592463
	KK7	0,498608803	0,102971063	0,114447115	0,510496253	0,511706294
Maximum hardness at 250 °C	KK5	0,579724859	0,092995708	0,115385532	0,588187878	0,591197894
	KK6	0,530427804	0,045000674	0,10660643	0,5326247	0,541035741
	KK7	0,657176641	0,041345968	0,10851756	0,658678928	0,666077484
Local maximum hardness at 200 °C	KK5	0,53431098	0,095013989	0,119168457	0,544300123	0,547503701
	KK6	0,660559083	0,079412959	0,11073285	0,666120723	0,669788137
	KK7	0,623979954	0,008548846	0,108846698	0,624058262	0,633414192
	KK5 BP	0,582867484	0,077106262	0,118097943	0,588751011	0,594726229

Appendix B: Suggested annealing procedures

Table B.1: Initial screening, KK5, KK6 and KK7 at 200 °C and 250 °C

Suggestion for 200 °C			Suggestion for 250 °C		
Sample no.	**Time [min]**	**Time [hh:mm]**	**Sample no.**	**Time [min]**	**Time [hh:mm]**
1	1	00:01	1	1	00:01
3	40	00:40	3	30	00:30
8	140	02:20	8	105	01:45
13	270	04:30	13	180	03:00
18	480	08:00	18	330	05:30

Table B.2: Suggested annealing procedure, KK5, KK6 and KK7 at 200 °C and 250 °C

Suggestion for 200 °C			Suggestion for 250 °C			New suggestion for 250 °C		
Sample no.	**Time [min]**	**Time [hh:mm]**	**Sample no.**	**Time [min]**	**Time [hh:mm]**	**Sample no.**	**Time [min]**	**Time [hh:mm]**
1	1	0:01	1	1	0:01	1	1	00:01
2	20	0:20	2	15	0:15	24	2	00:02
3	40	0:40	3	30	0:30	25	3	00:03
4	60	1:00	4	45	0:45	26	4	00:04
5	80	1:20	5	60	1:00	2	5	00:05
6	100	1:40	6	75	1:15	27	7	00:07
7	120	2:00	7	90	1:30	3	10	00:10
8	140	2:20	8	105	1:45	4	15	00:15
9	160	2:40	9	120	2:00	5	20	00:20
10	180	3:00	10	135	2:15	6	25	00:25
11	210	3:30	11	150	2:30	7	30	00:30
12	240	4:00	12	165	2:45	8	40	00:40
13	270	4:30	13	180	3:00	9	50	00:50
14	300	5:00	14	210	3:30	10	60	01:00
15	330	5:30	15	240	4:00	11	80	01:20
16	360	6:00	16	270	4:30	12	100	01:40
17	420	7:00	17	300	5:00	13	120	02:00
18	480	8:00	18	330	5:30	-	-	-
19	600	10:00	19	360	6:00	-	-	-
20	720	12:00	20	390	6:30	-	-	-
21	840	14:00	21	420	7:00	-	-	-
22	1020	17:00	22	450	7:30	-	-	-
23	1440	24:00	23	480	8:00	-	-	-

Appendix C: TEM images

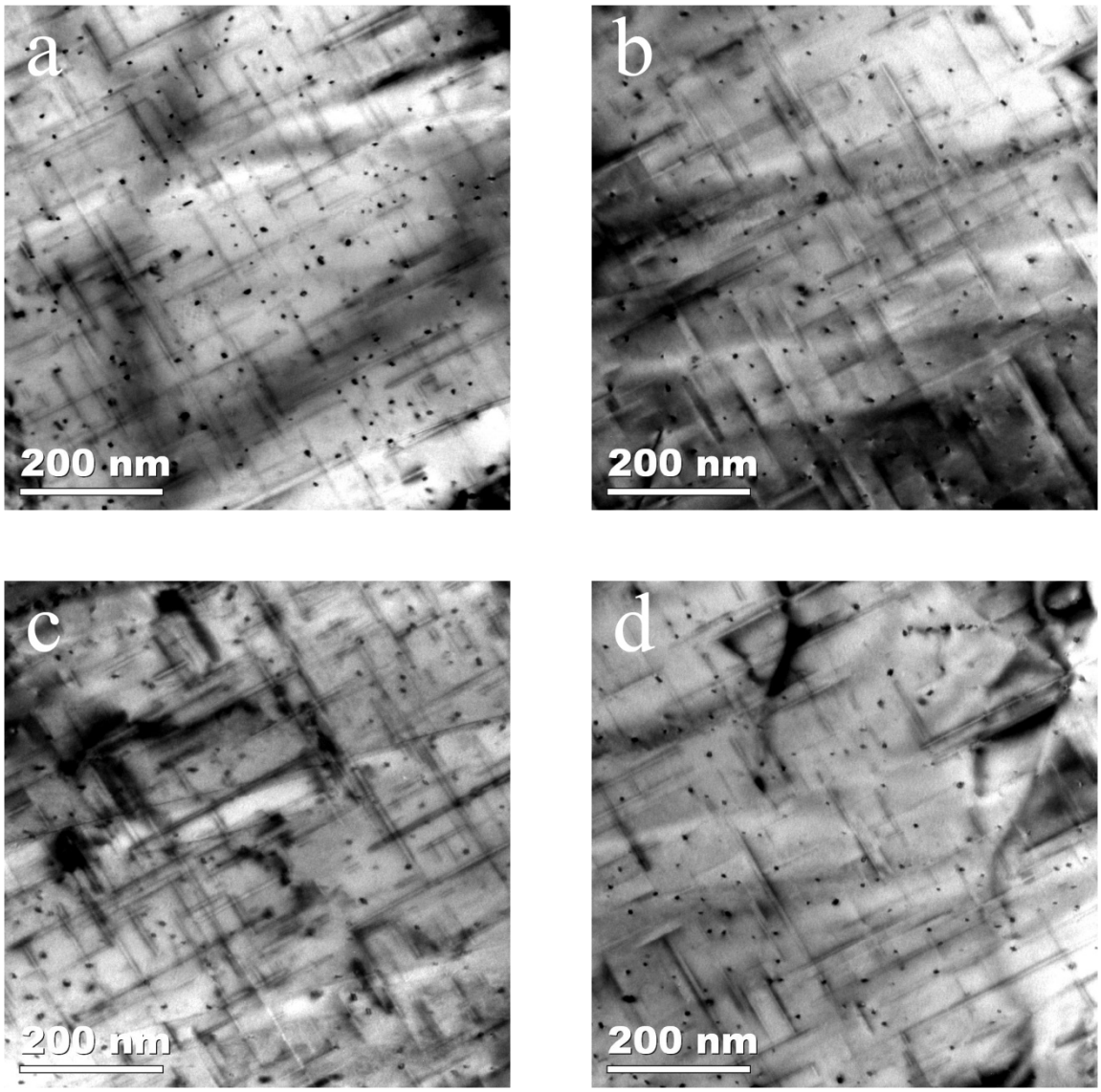

Figures C.1 (a)-(d): Examples of TEM images taken with JEOL JEM-2010 at max hardness after artificial ageing at 200 °C for KK5 at 30k magnification

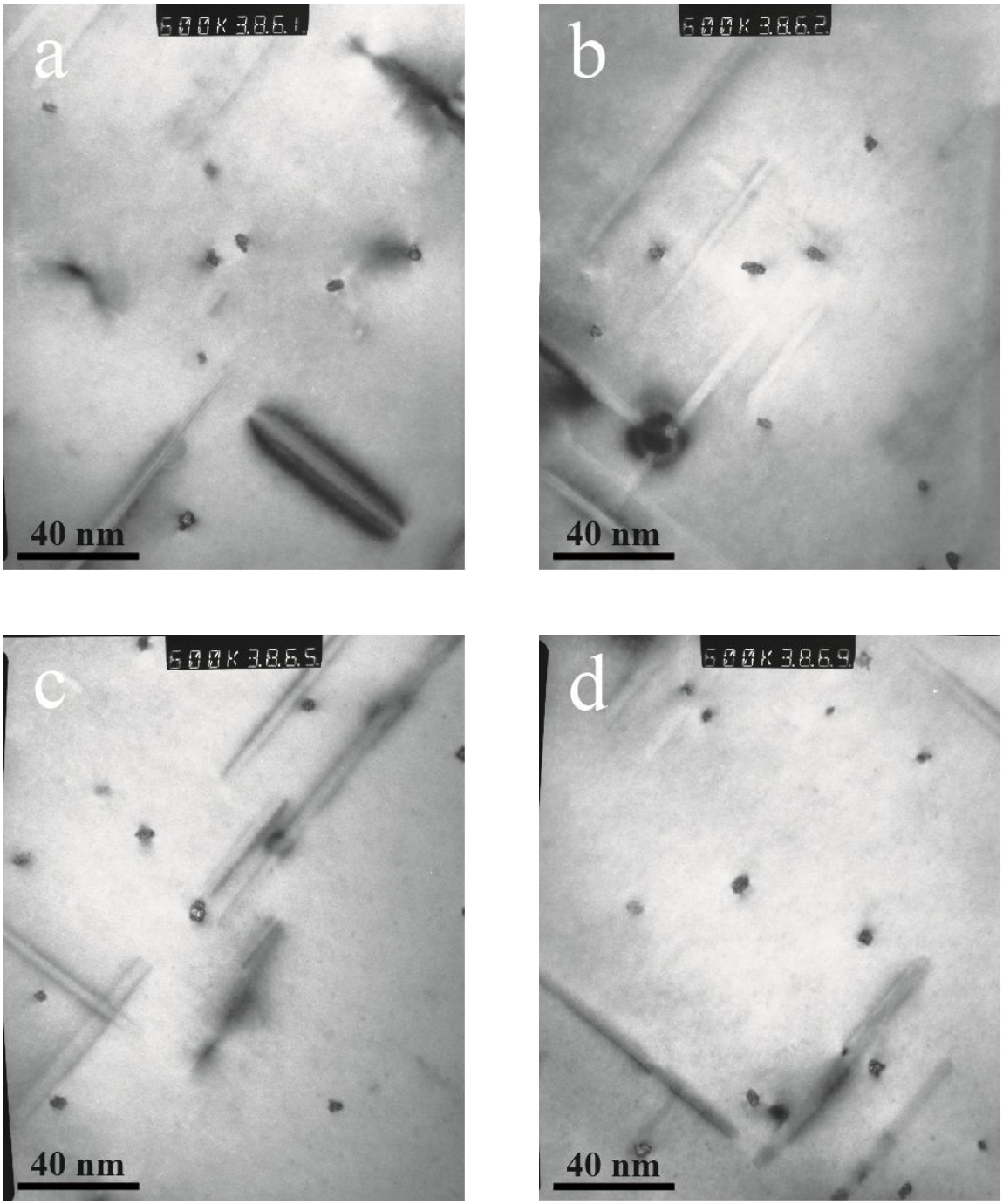

Figures C.2 (a)-(d): Examples of TEM images taken with Philips CM30 at max hardness after artificial ageing at 200 °C for KK5 at 600k magnification

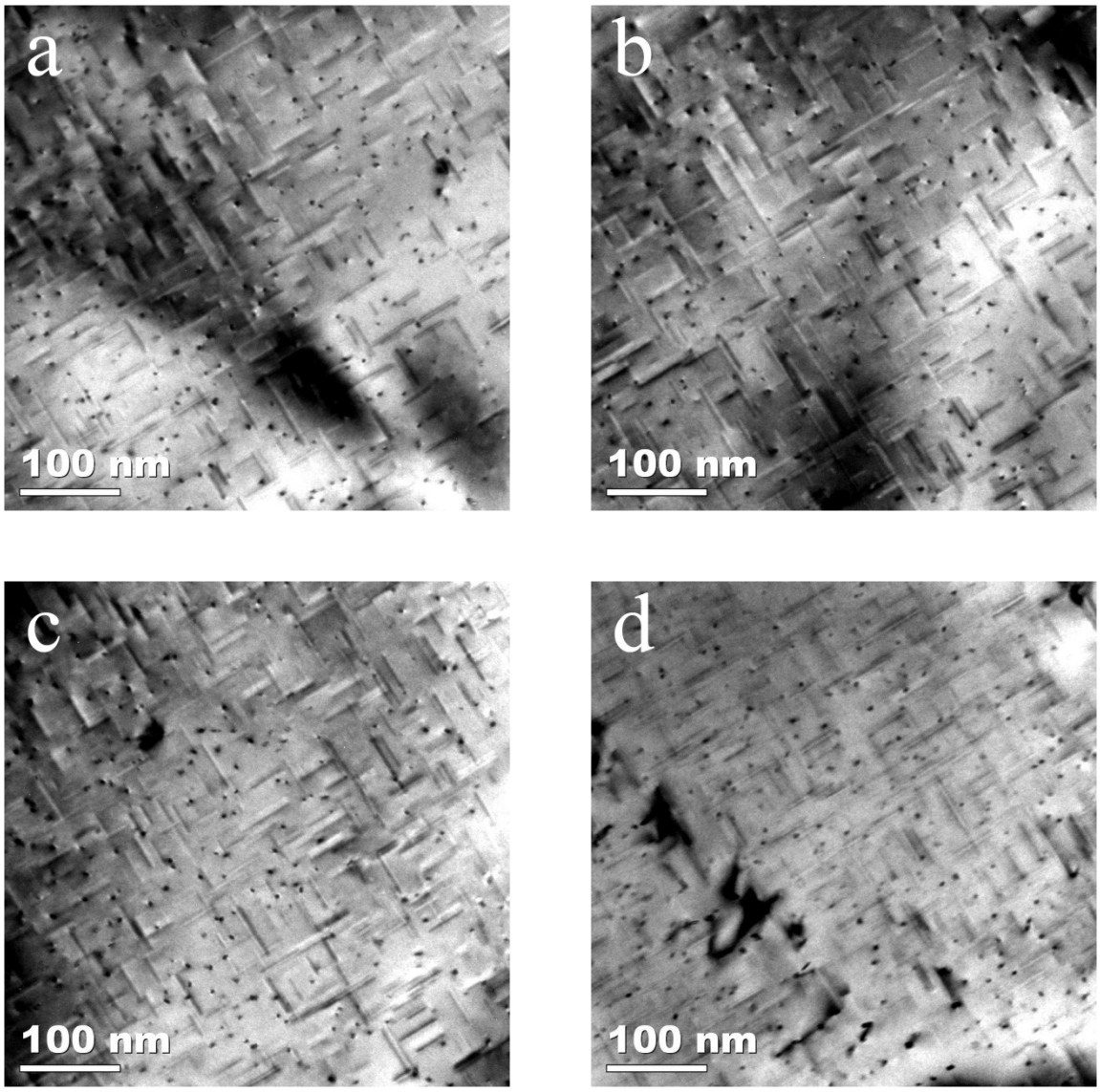

Figures C.3 (a)-(d): Examples of TEM images taken with JEOL JEM-2010 at max hardness after artificial ageing at 200 °C for KK6 at 40k magnification

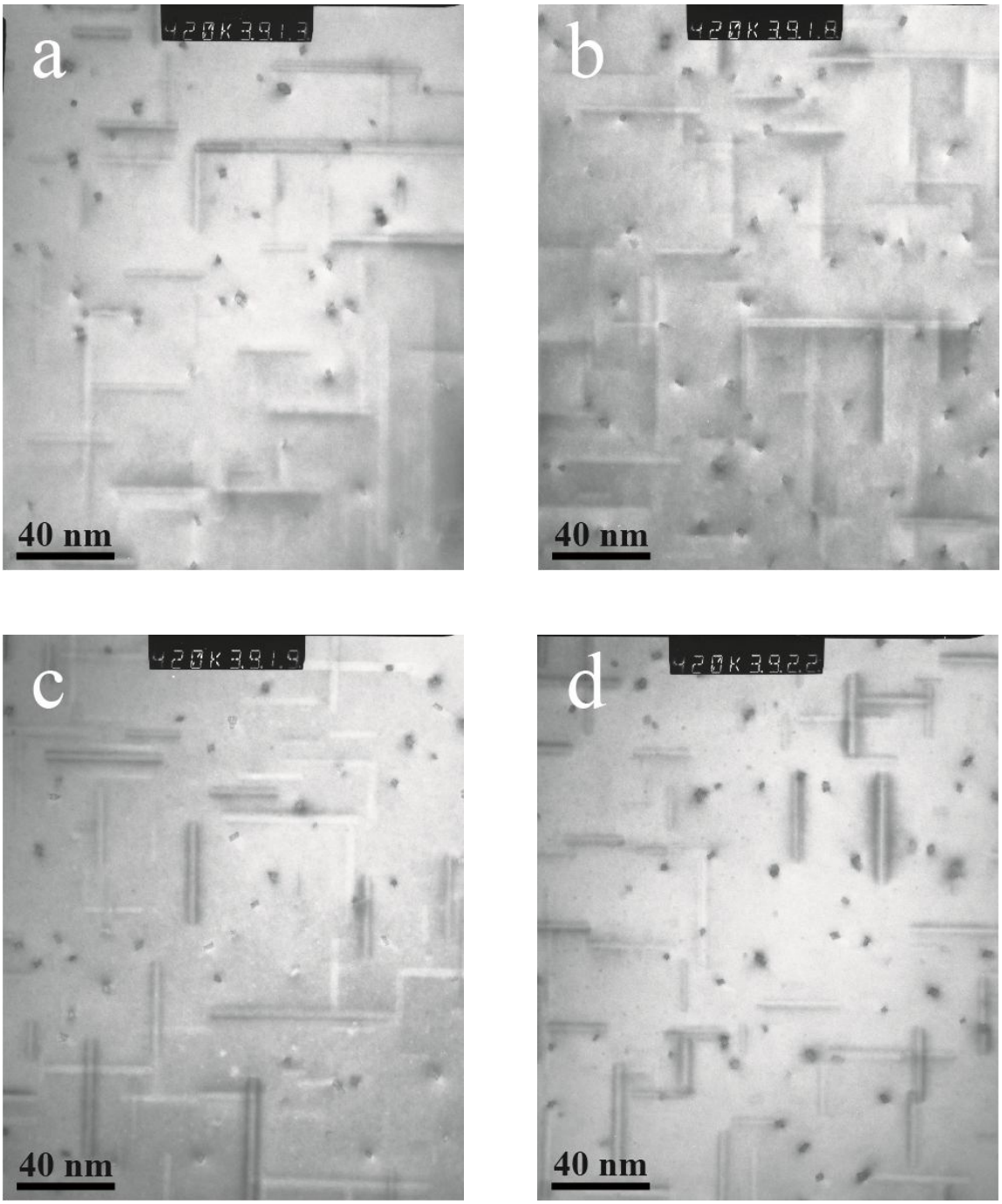

Figures C.4 (a)-(d): Examples of TEM images taken with Philips CM30 at max hardness after artificial ageing at 200 °C for KK6 at 420k magnification

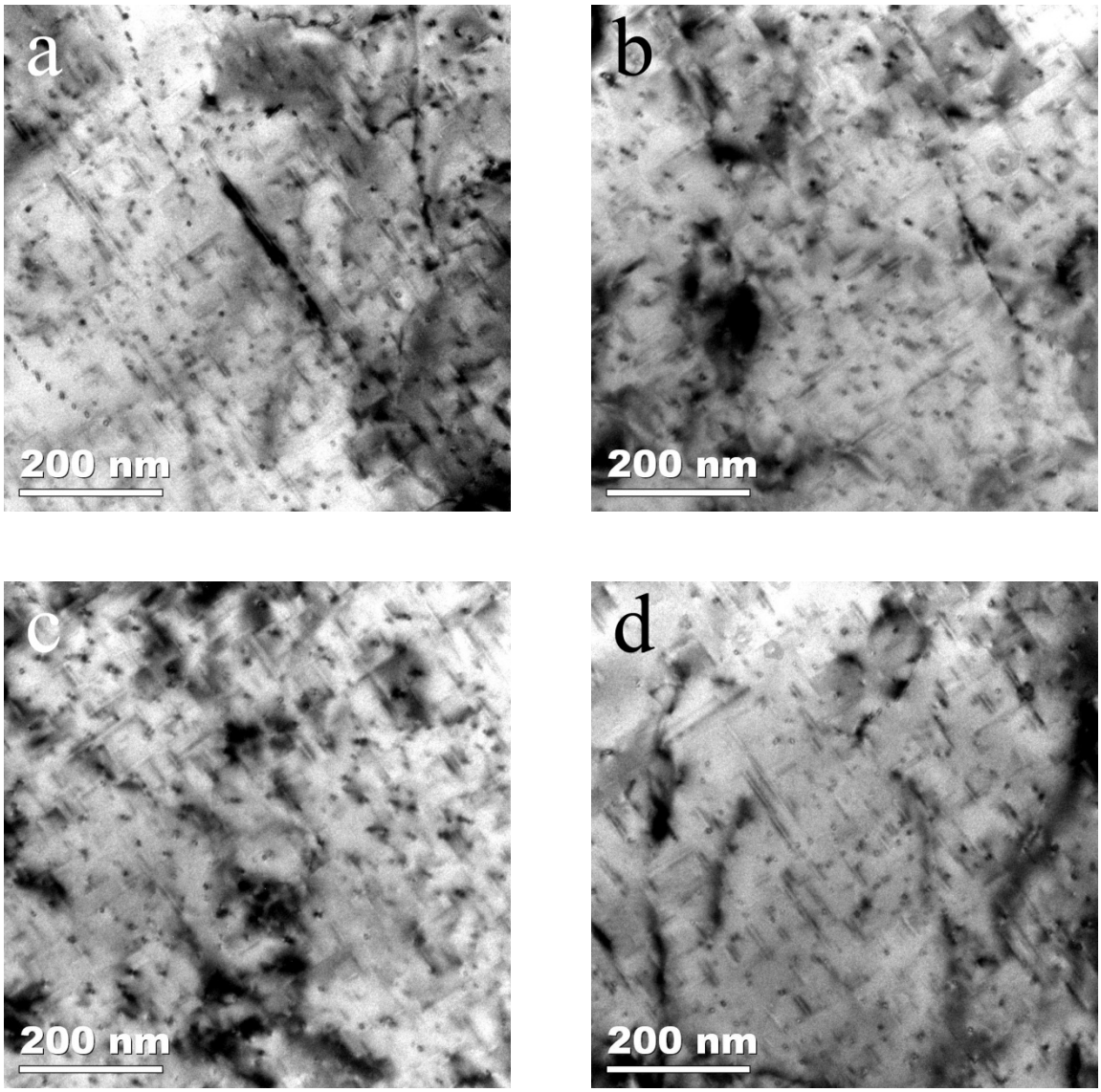

Figures C.5 (a)-(d): Examples of TEM images taken with JEOL JEM-2010 at max hardness after artificial ageing at 200 °C for KK7 at 30k magnification

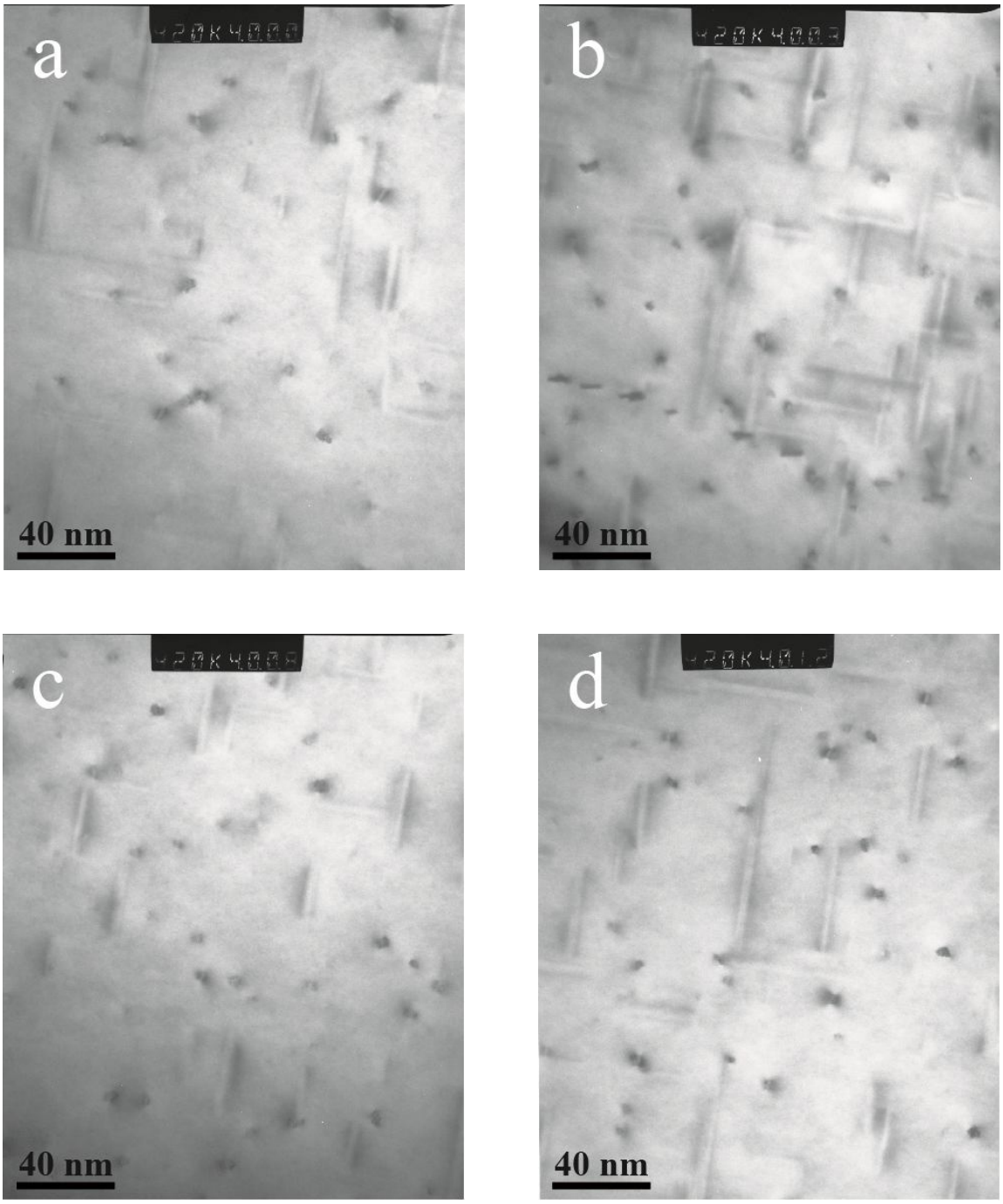

Figures C.6 (a)-(d): Examples of TEM images taken with Philips CM30 at max hardness after artificial ageing at 200 °C for KK7 at 420k magnification

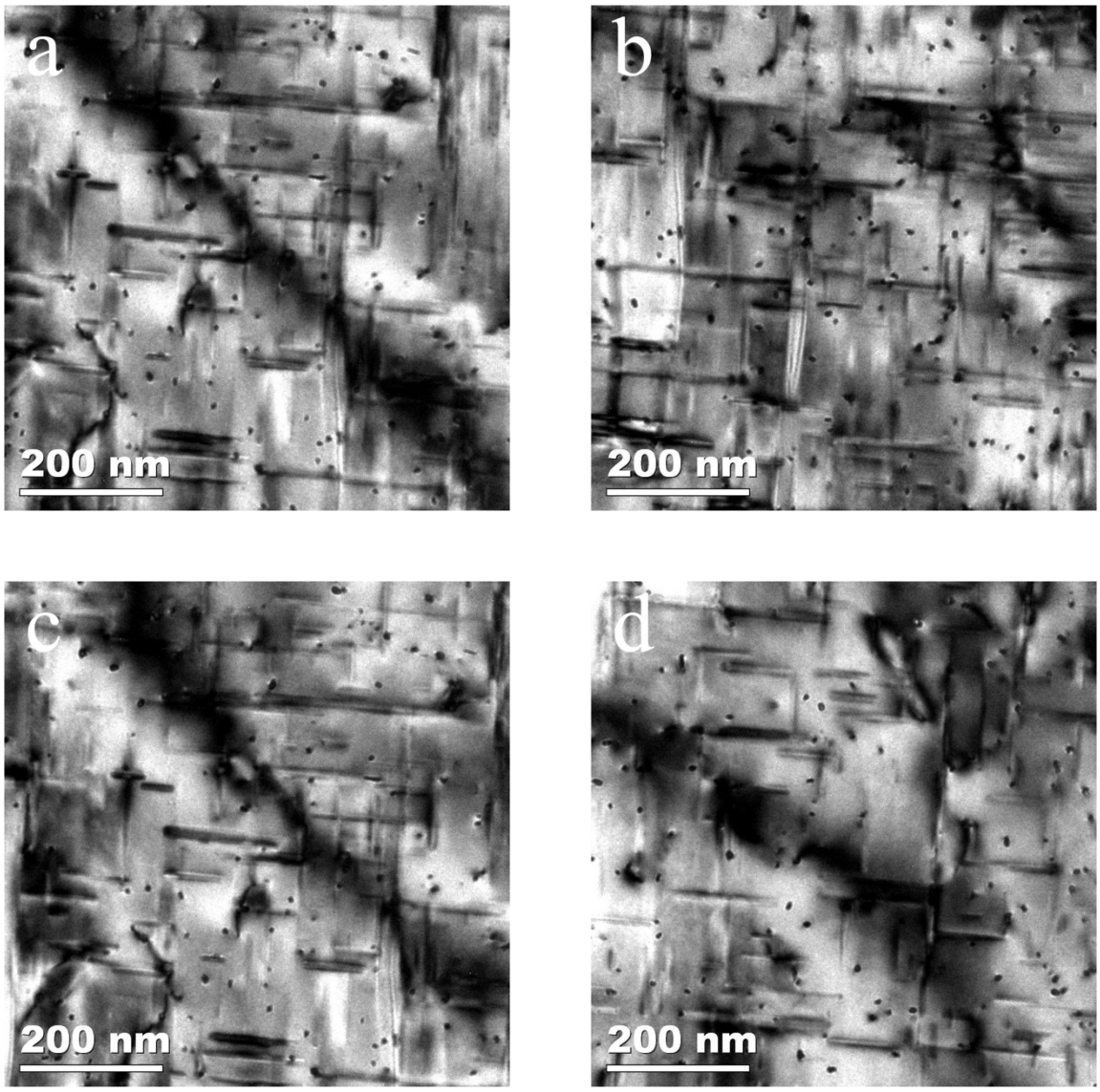

Figures C.7 (a)-(d): Examples of TEM images taken with JEOL JEM-2010 at max hardness after artificial ageing at 250 °C for KK5 at 30k magnification

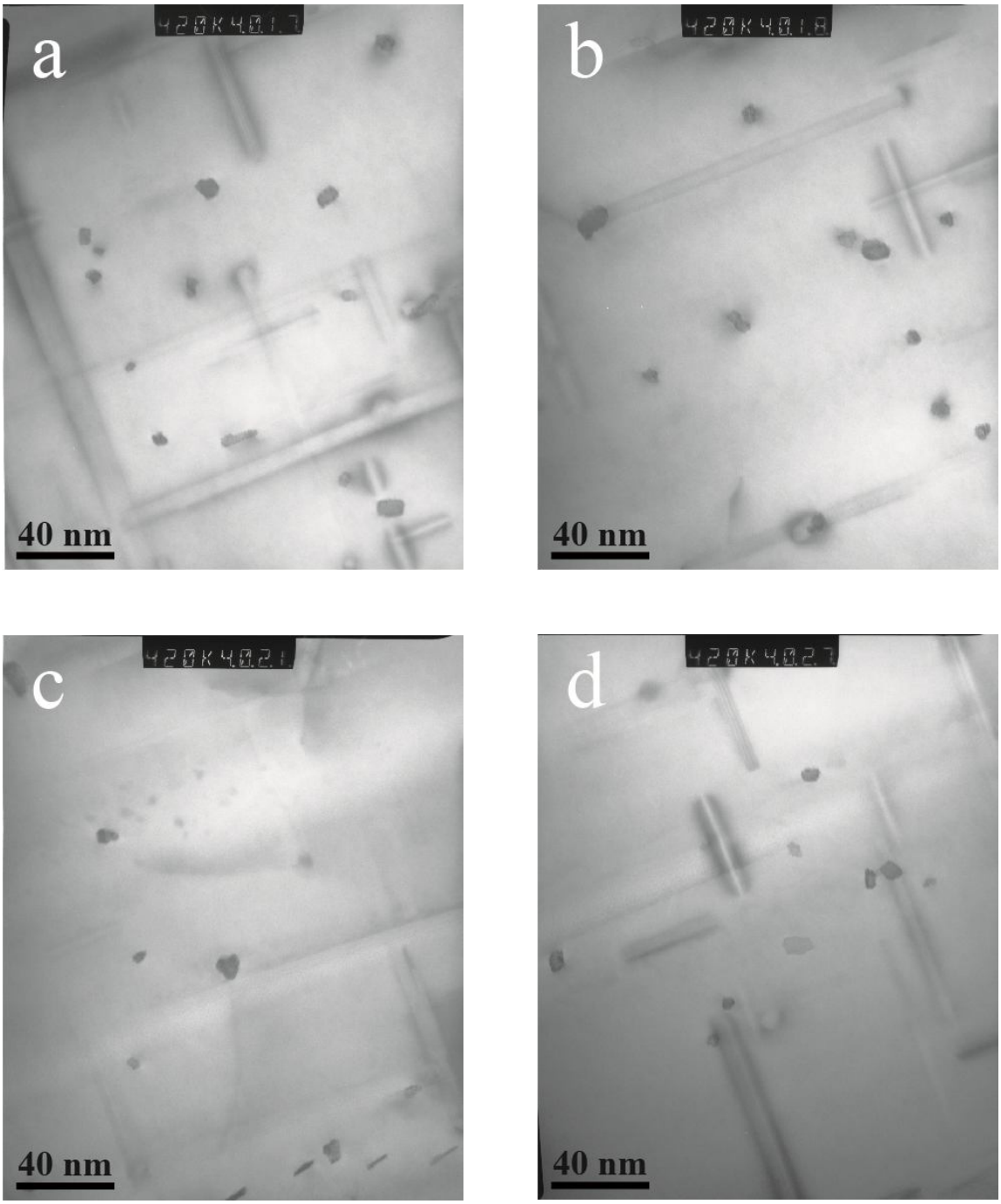

Figures C.8 (a)-(d): Examples of TEM images taken with Philips CM30 at max hardness after artificial ageing at 250 °C for KK5 at 420k magnification

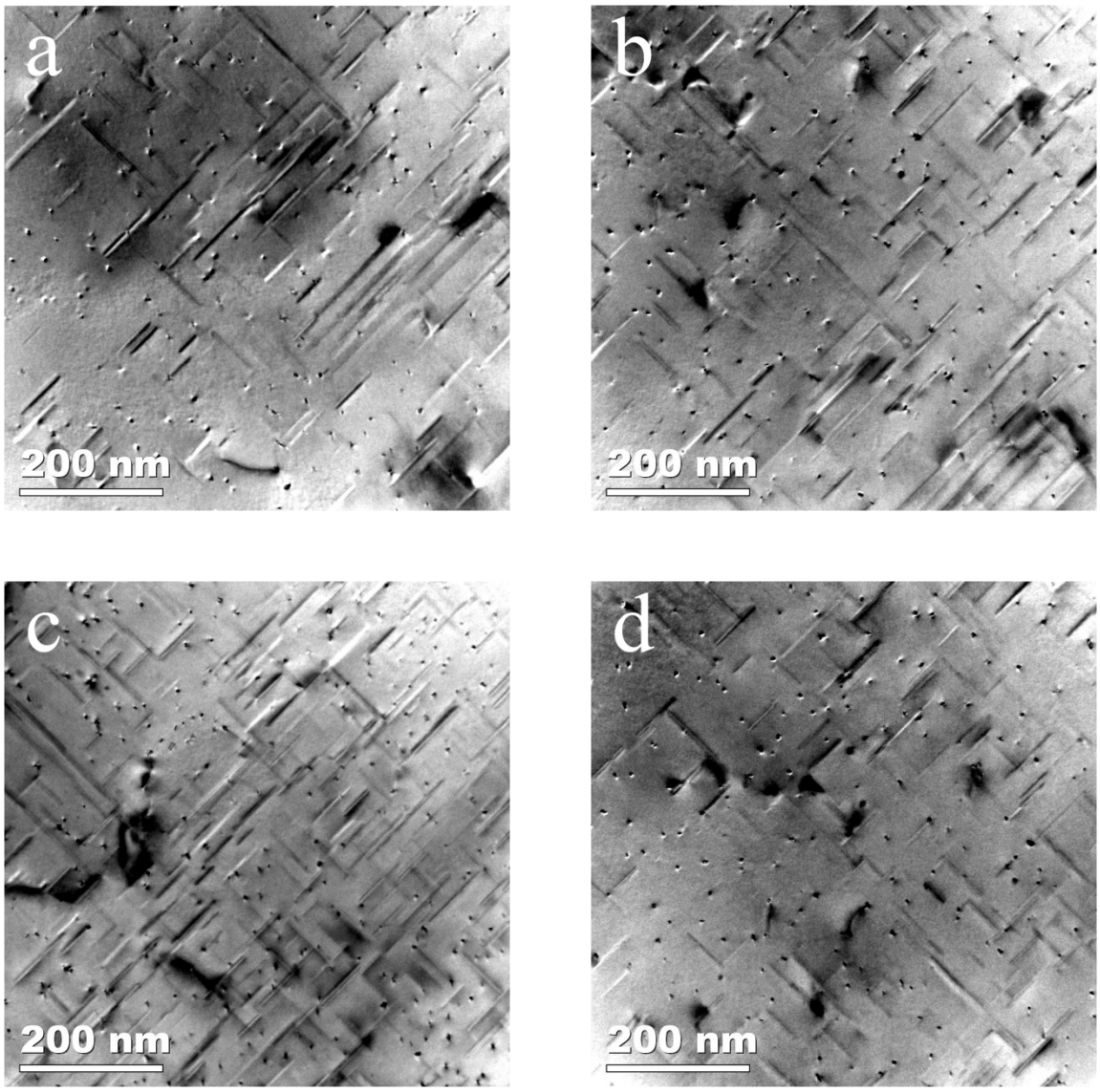

Figures C.9 (a)-(d): Examples of TEM images taken with JEOL JEM-2010 at max hardness after artificial ageing at 250 °C for KK6 at 30k magnification

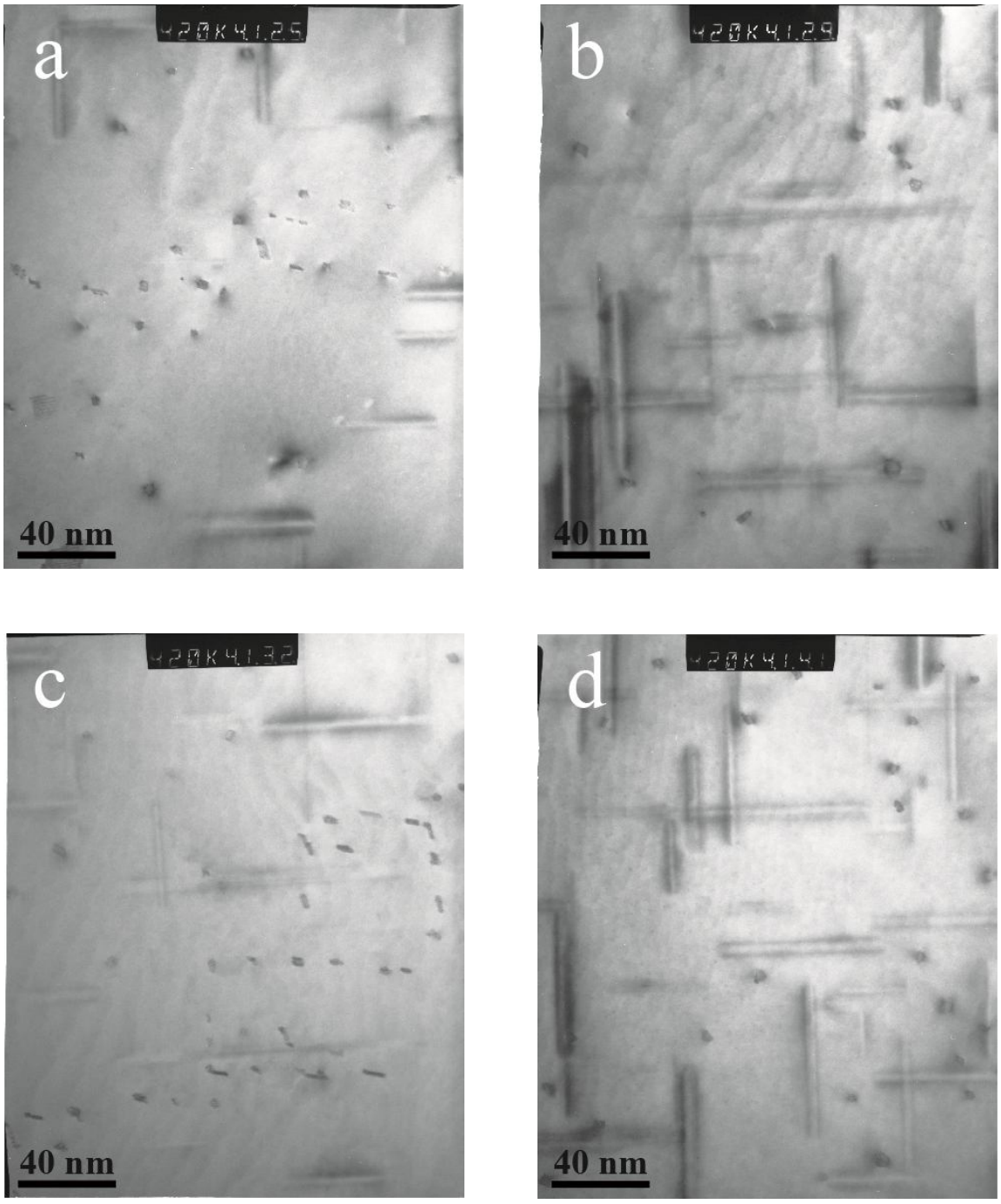

Figures C.10 (a)-(d): Examples of TEM images taken with Philips CM30 at max hardness after artificial ageing at 250 °C for KK6 at 420k magnification

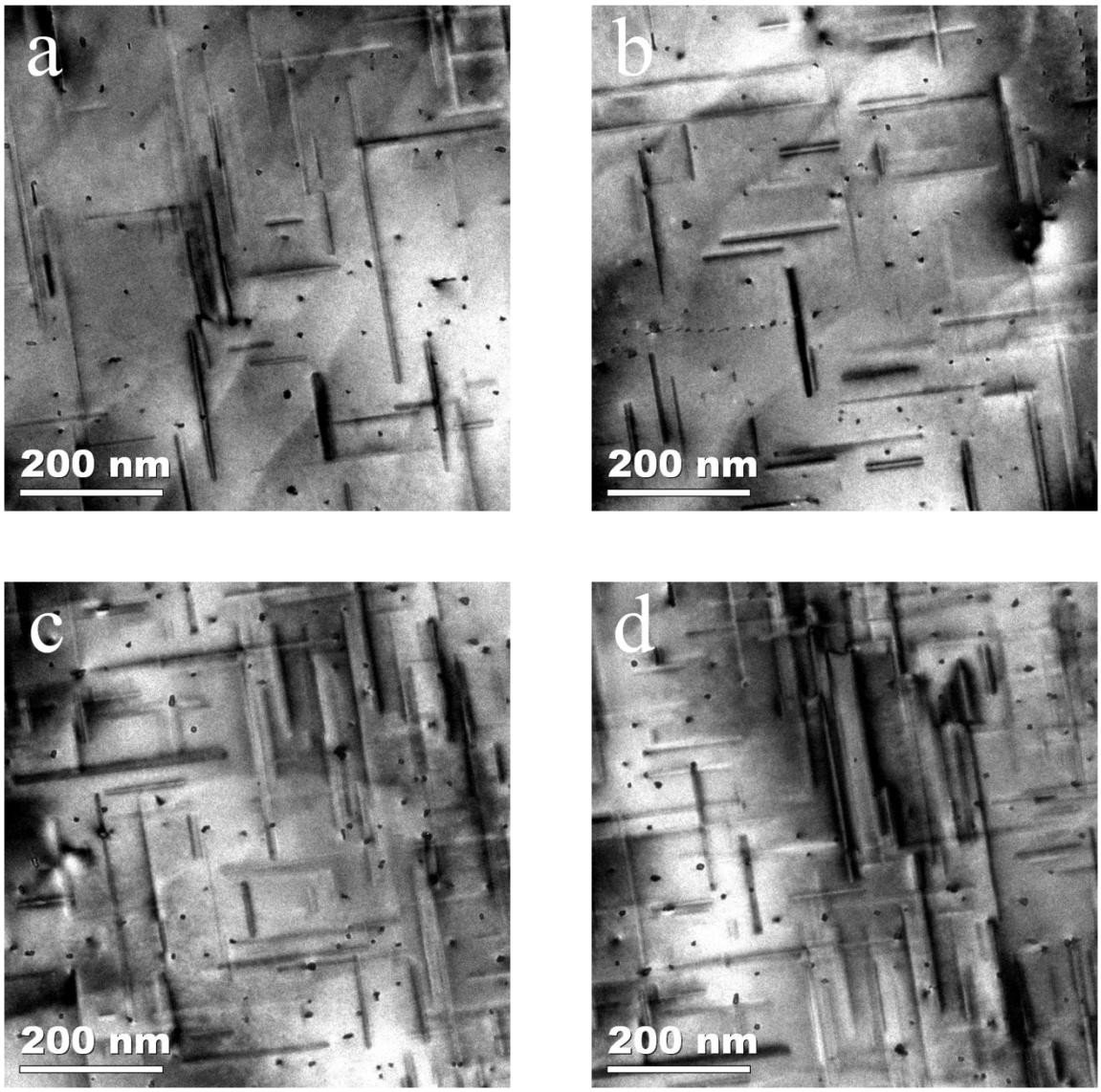

Figures C.11 (a)-(d): Examples of TEM images taken with JEOL JEM-2010 at max hardness after artificial ageing at 250 °C for KK7 at 30k magnification

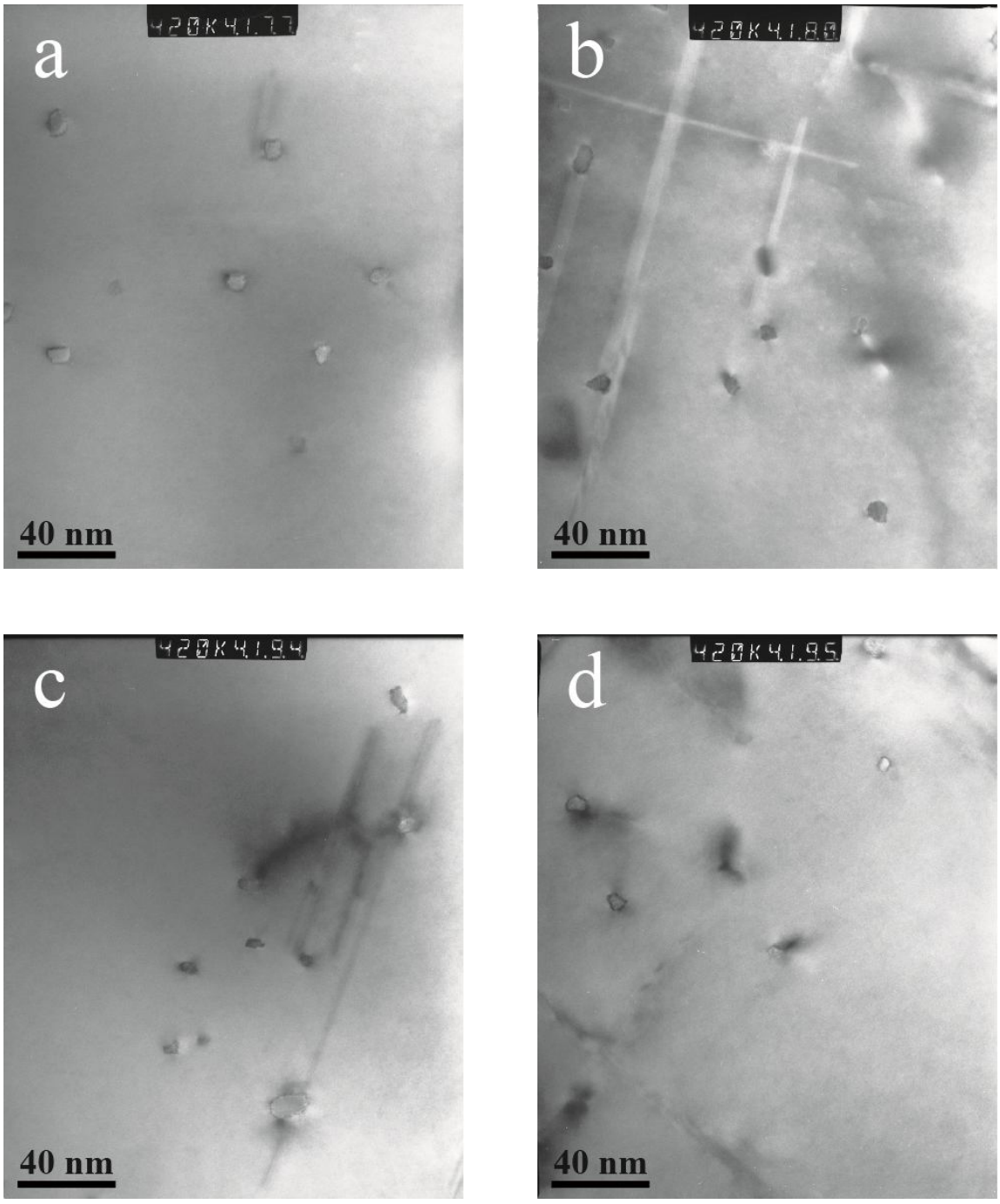

Figures C.12 (a)-(d): Examples of TEM images taken with Philips CM30 at max hardness after artificial ageing at 250 °C for KK7 at 420k magnification

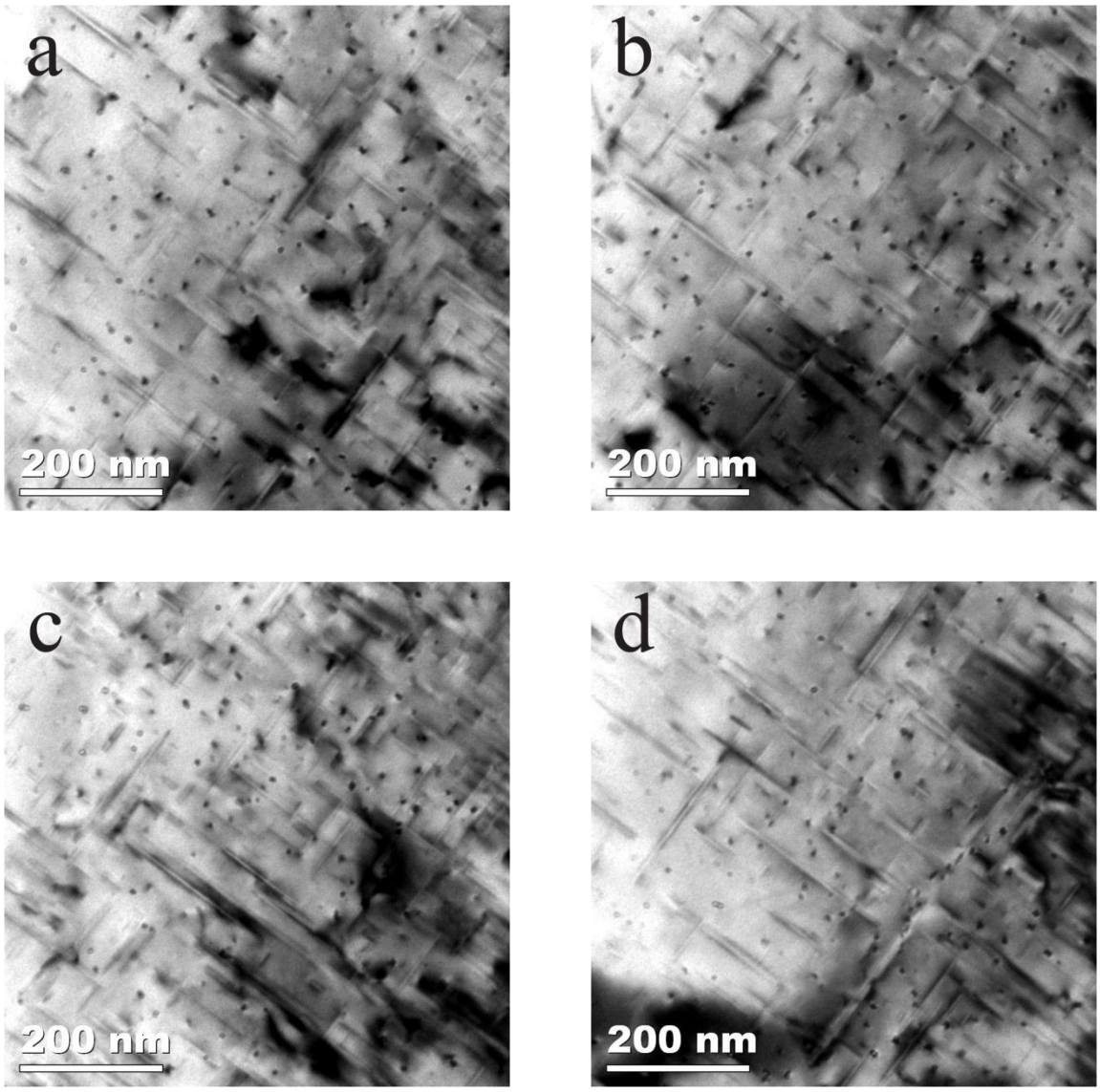

Figures C.13 (a)-(d): Examples of TEM images taken with JEOL JEM-2010 at local max at overaged conditions after artificial ageing at 200 °C for KK5 at 30k magnification

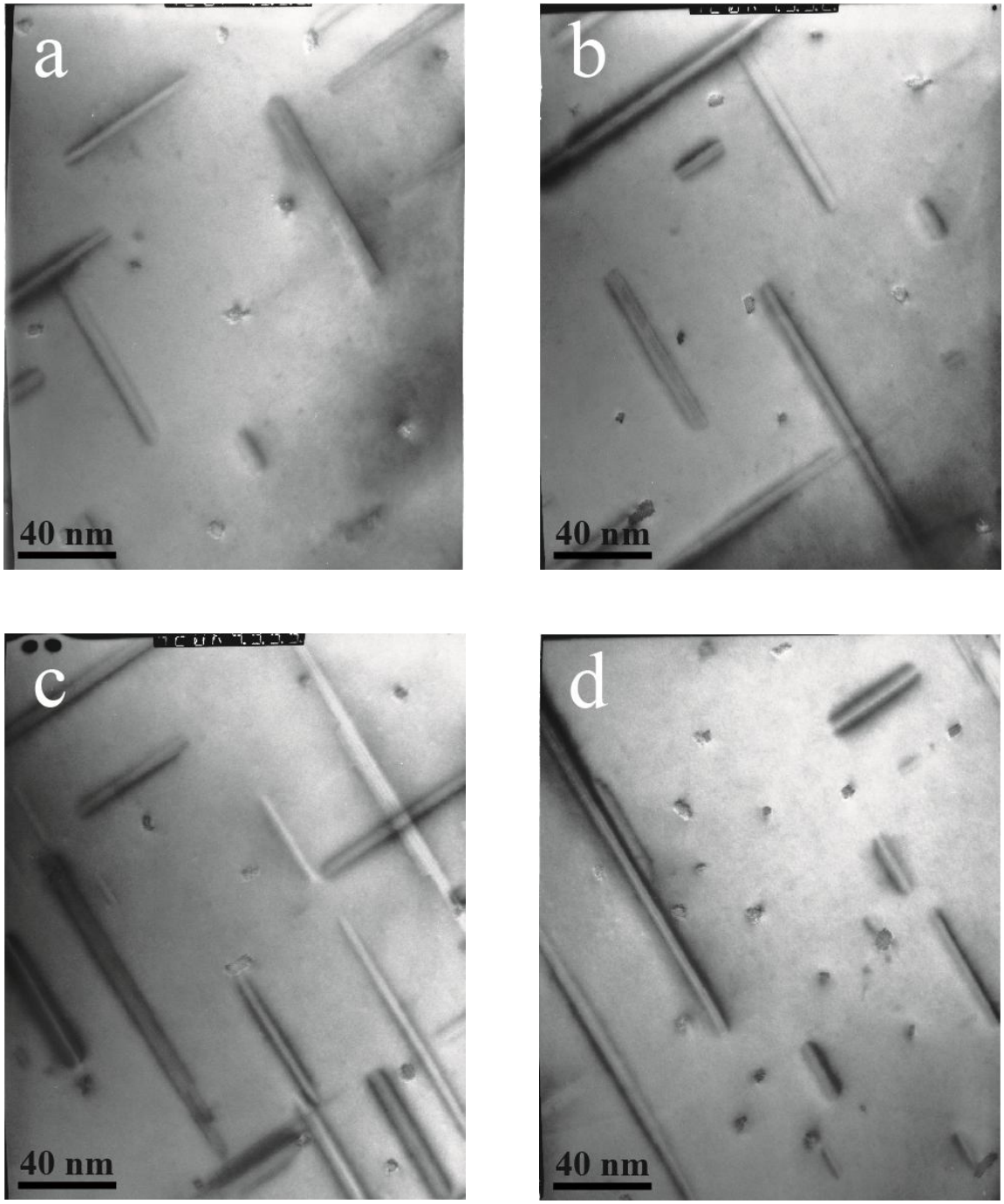

Figures C.14 (a)-(d): Examples of TEM images taken with Philips CM30 at local max at overaged conditions after artificial ageing at 200 °C for KK5 at 420k magnification

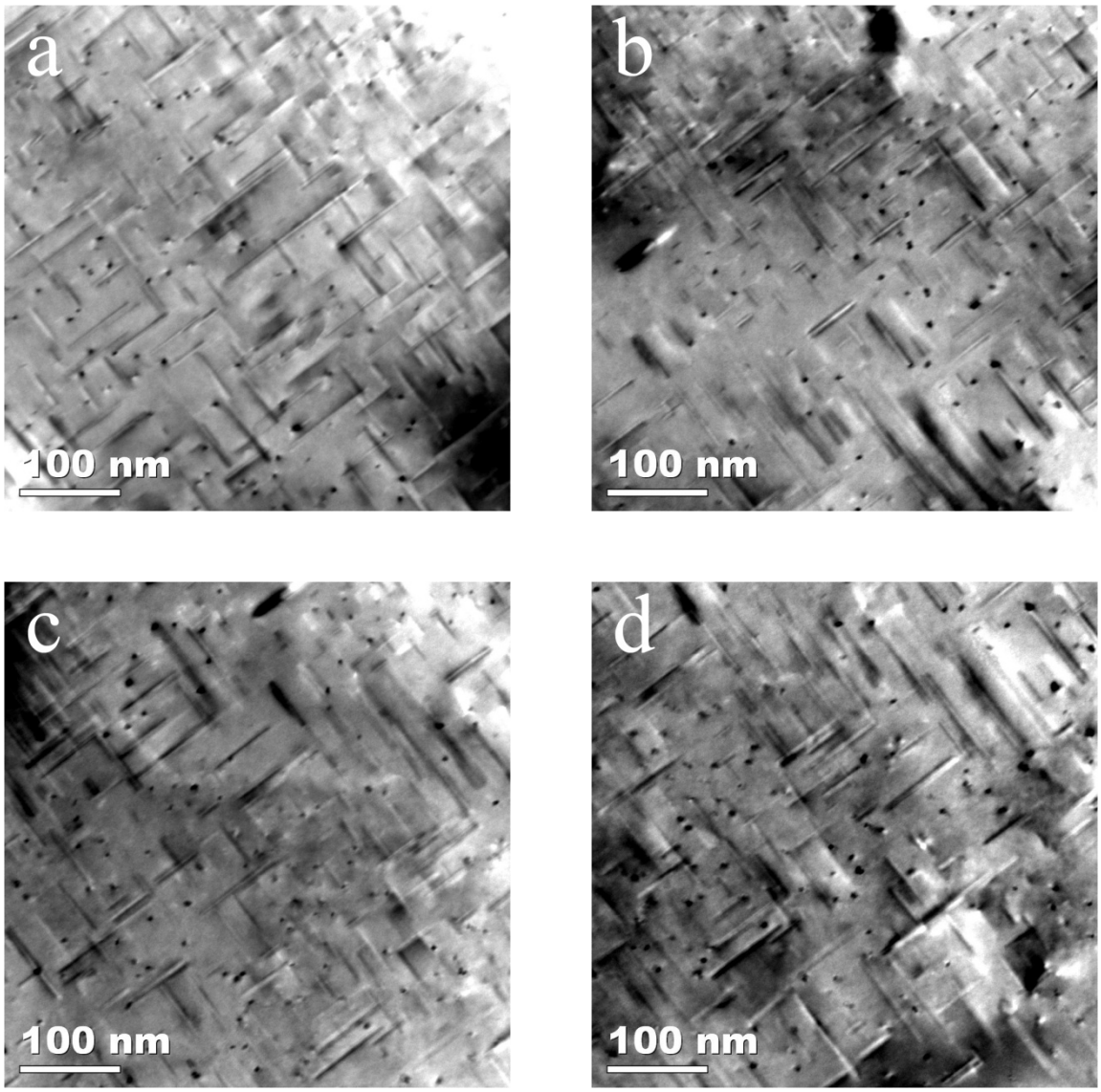

Figures C.15 (a)-(d): Examples of TEM images taken with JEOL JEM-2010 at local max at overaged conditions after artificial ageing at 200 °C for KK6 at 40k magnification

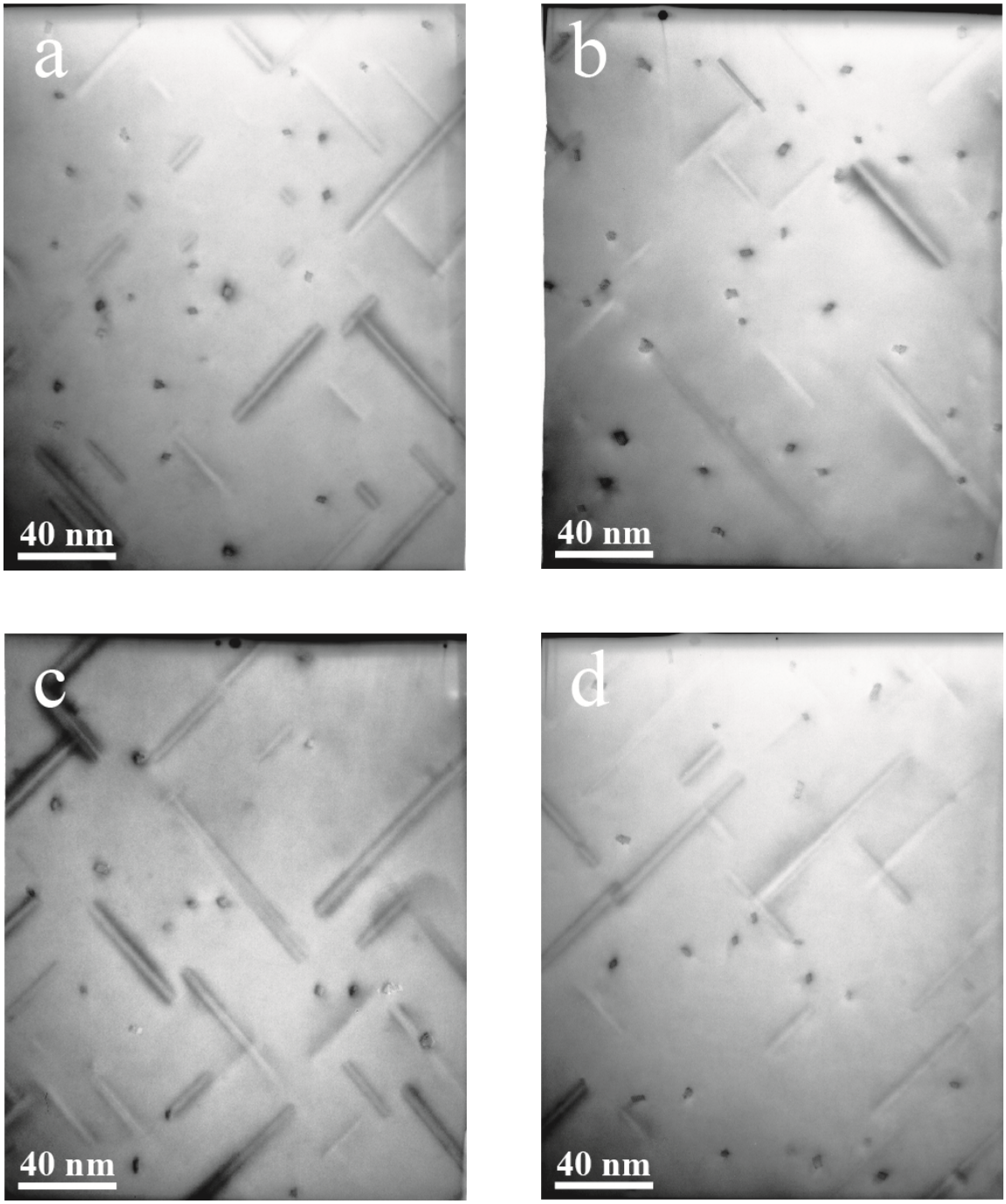

Figures C.16 (a)-(d): Examples of TEM images taken with Philips CM30 at local max at overaged conditions after artificial ageing at 200 °C for KK6 at 420k magnification

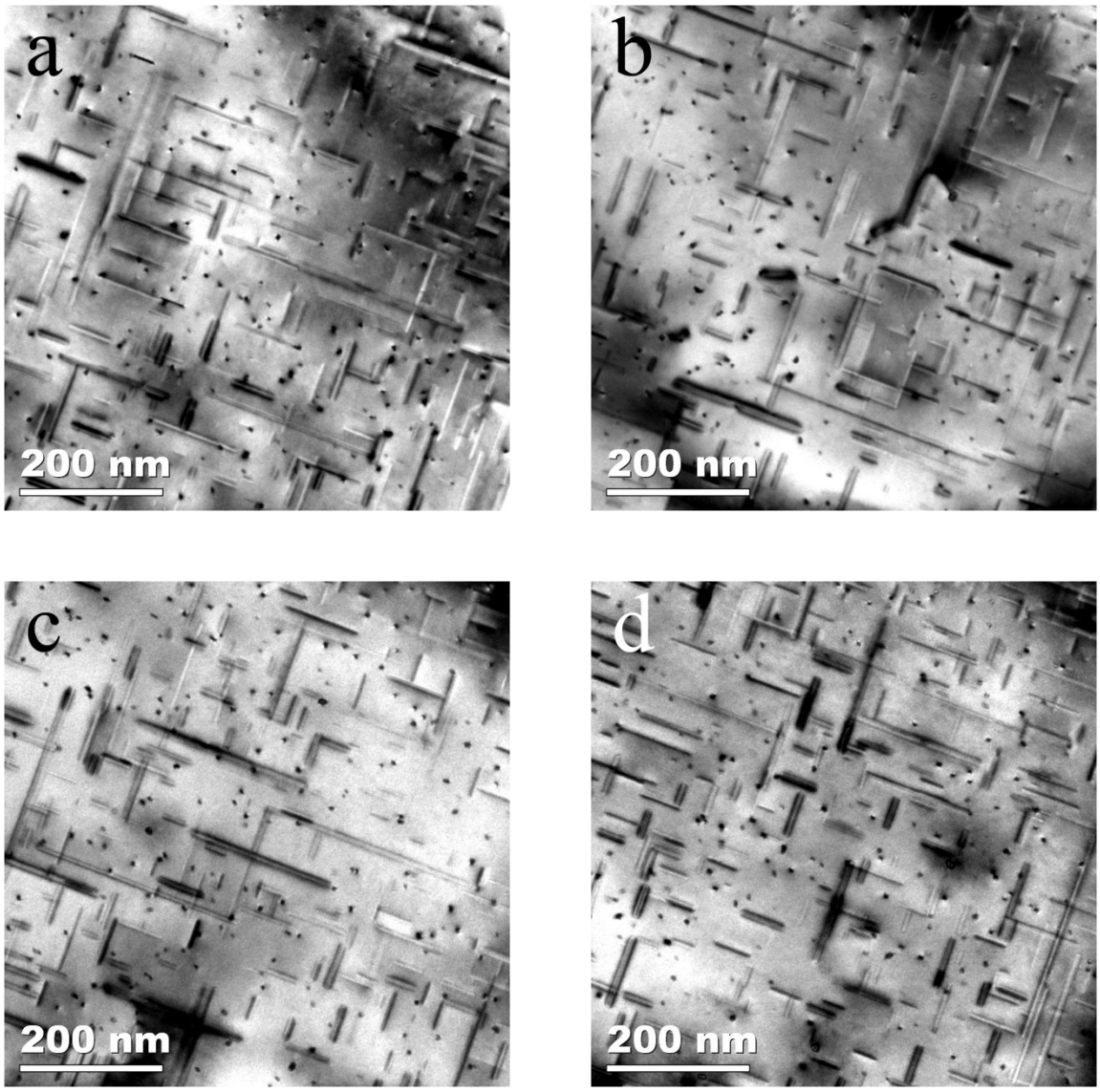

Figures C.17 (a)-(d): Examples of TEM images taken with JEOL JEM-2010 at local max at overaged conditions after artificial ageing at 200 °C for KK7 at 30k magnification

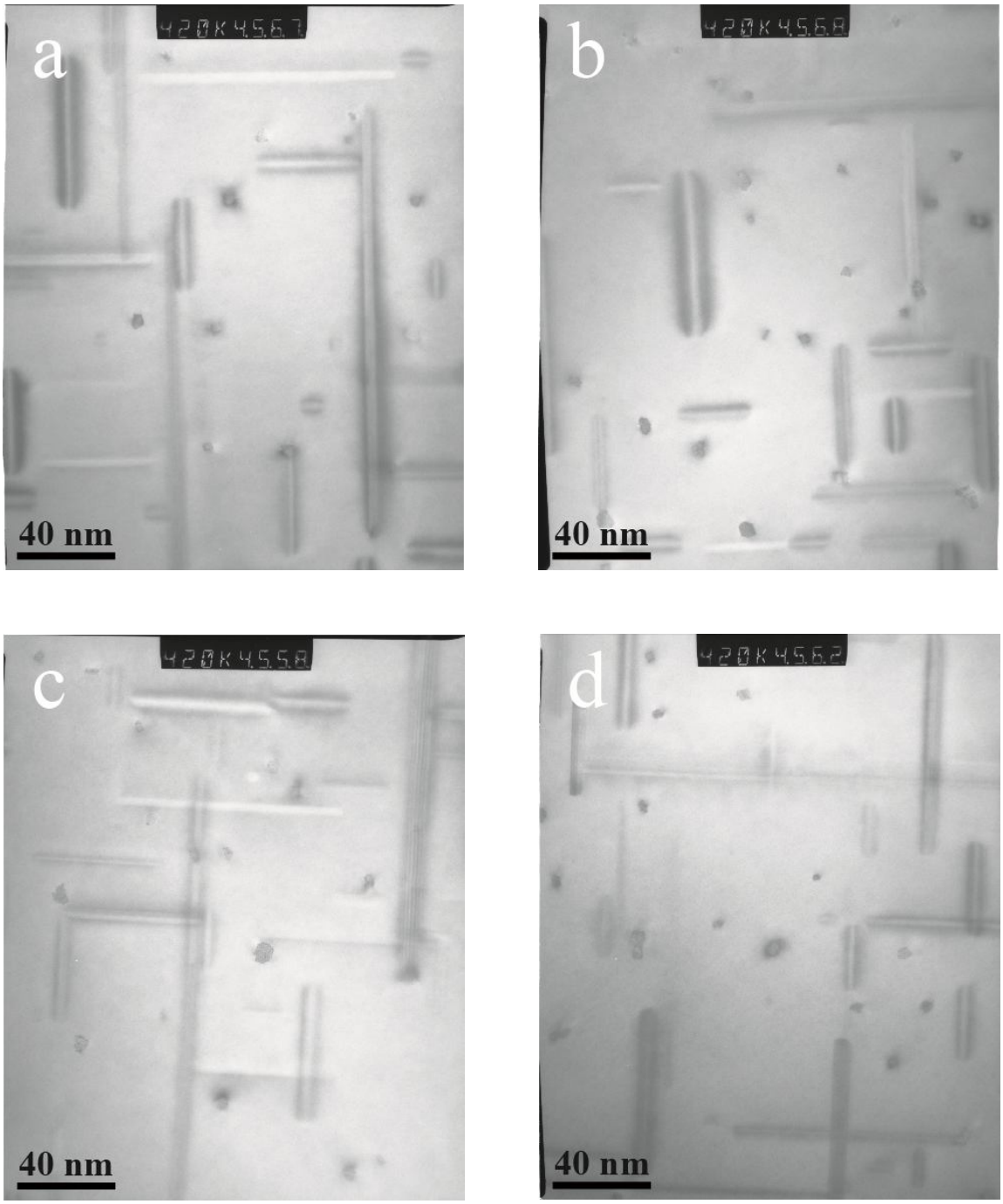

Figures C.18 (a)-(d): Examples of TEM images taken with Philips CM30 at local max at overaged conditions after artificial ageing at 200 °C for KK7 at 420k magnification

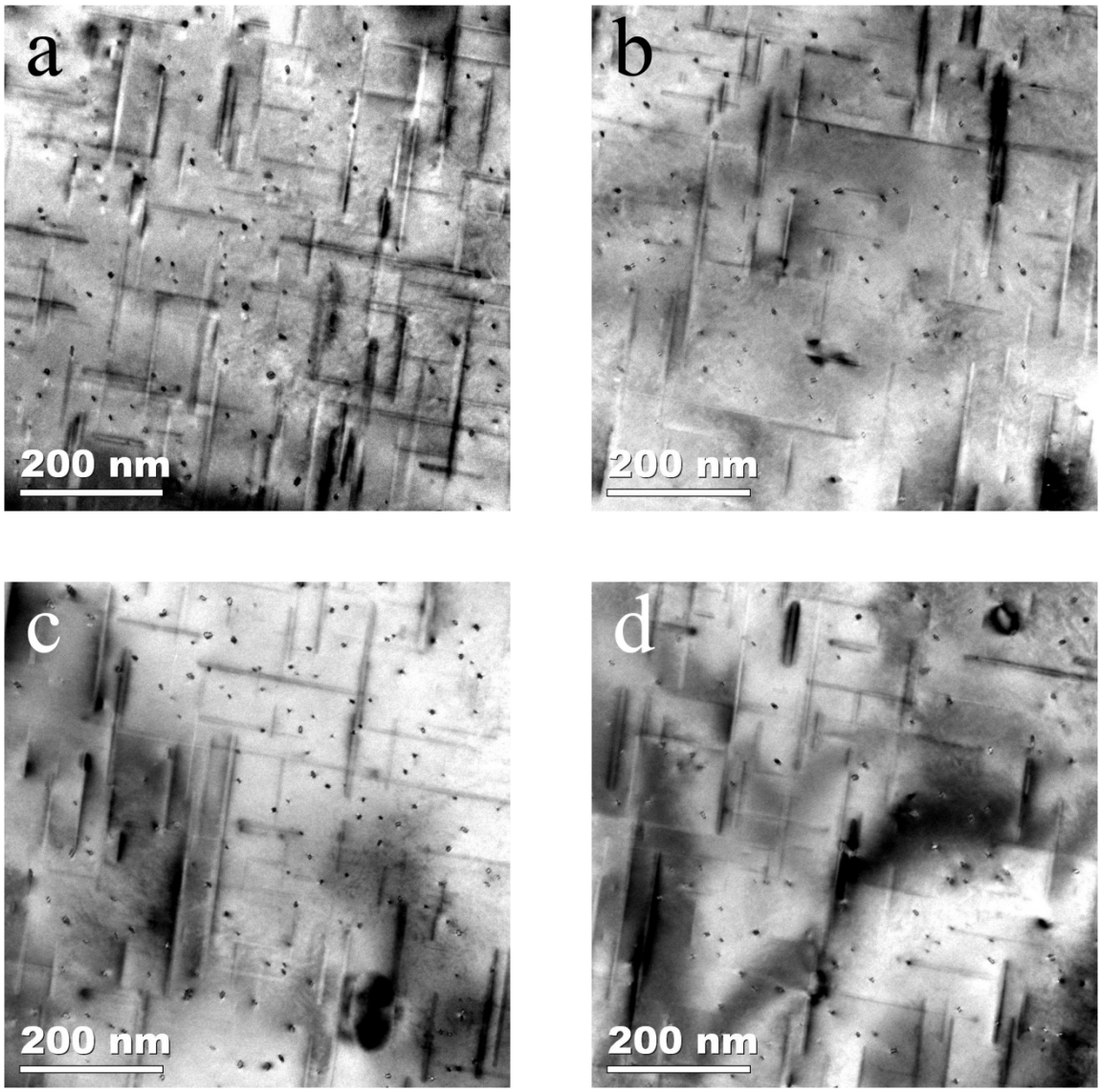

Figures C.19 (a)-(d): Examples of TEM images taken with JEOL JEM-2010 before local max at overaged conditions after artificial ageing at 200 °C for KK5 at 30k magnification

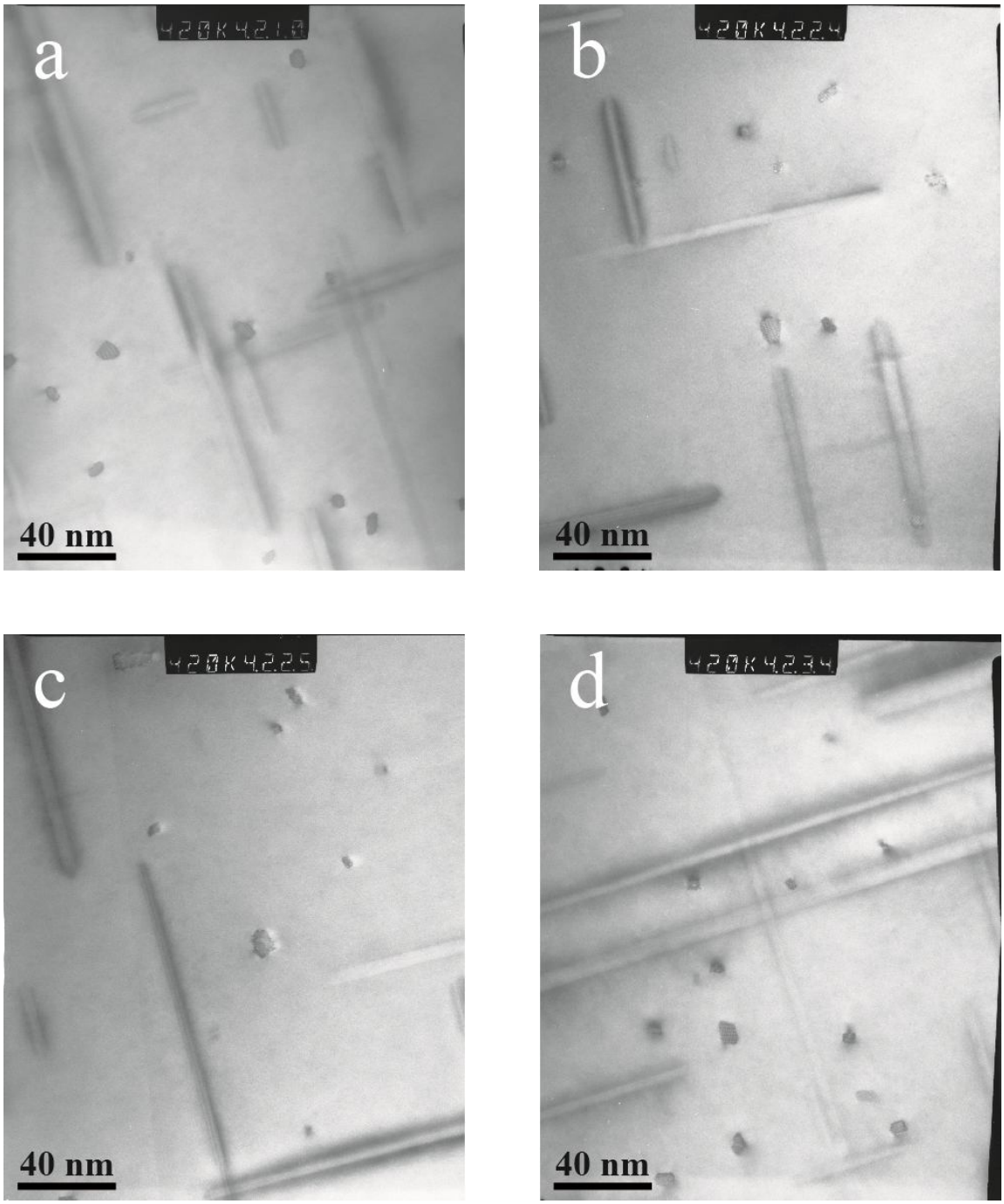

Figures C.20 (a)-(d): Examples of TEM images taken with Philips CM30 before local max at overaged conditions after artificial ageing at 200 °C for KK5 at 420k magnification

Appendix D: Material properties

Table D.1: Composition of the alloys analysed in the master thesis [6]

Alloy	Alloy designation	Solute content [wt%]	Solute content [at%]	Total (Si + Mg) [at%]	Solute ratio (Si/Mg) [at%]
KK5	β'	0,64 Si 0,90 Mg 0,21 Fe 0,55Mn	0,62 Si 1,00 Mg 0,10 Fe 0,27 Mn	1,54	0,71
KK6	U1 + B'	1,16 Si 0,45 Mg 0,20 Fe 0,55 Mn	1,12 Si 0,50 Mg 0,10 Fe 0,27 Mn	1,61	2,58
KK7	U2	0,90 Si 0,67 Mg 0,21 Fe 0,55 Mn	0,87 Si 0,75 Mg 0,10 Fe 0,27 Mn	1,57	1,34

Table D.2: Overview of the important precipitates and phases existing in the Al-Mg-Si system

Phase	Shape	Formula	Space group	Lattice parameters [nm]	References
GP-zone	Needle	AlMg4Si6	*C*2/*m*	*a*= 1,48 *b* = 0,405 *c* = 0,648, β = 105,3°	[27]
GP-zone	Plate	Si/Mg = 1	(fcc L10)	*a* = 0,405	[27]
β"	Needle	Mg5Si6	*C*2/*m*	*a*= 1,516 *b* = 0,405 *c* = 0,674 *β* = 105,3°	[10, 27]
β'	Needle	$Mg_{1,8}Si$	$P6_3/m$	a = b = 0,715 c = 0,405 γ = 120°	[26, 27]
B'	Lath	$Mg_9Al_4Si_7$	$P6_3/m$	a = b = 0,405 c = 0,674 γ = 120°	[28]
U1	Needle	$MgAl_2Si_2$	$P_{\bar{3}m1}$	a = b = 0,405 c = 0,674 γ = 120°	[25]
U2	Needle	$Mg_4Al_4Si_4$	P_{nma}	a = 0,675 b = 0,405 c = 0,794	[27]
β	Plate/cube	Mg_2Si	$F_{m\bar{3}m}$	*a* = 635.4	[25]

Appendix E: Risk and safety phrases

Table E.1: List of risk and safety phrases [48]

Risk phrases		Safety phrases	
Number	Phrase	Number	Phrase
R8	Contact with combustible material may cause fire	S7	Keep container tightly closed
R11	Highly flammable	S9	Keep container in a well-ventilated place
R20	Harmful by inhalation	S16	Keep away from sources of ignition
R21	Harmful in contact with skin	S24	Avoid contact with skin
R22	Harmful if swallowed	S25	Avoid contact with eyes
R23	Toxic by inhalation	S26	In case of contact with eyes, rinse immediately with plenty of water and seek medical advice
R24	Toxic in contact with skin	S36	Wear suitable protective clothing
R25	Toxic if swallowed	S37	Wear suitable gloves
R35	Causes severe burns	S38	In case of insufficient ventilation, wear suitable respiratory equipment.
R36	Irritating to eyes	S39	Wear eye / face protection
R37	Irritating to respiratory system	S45	In case of accident or if you feel unwell, seek medical advice immediately (show the label whenever possible.)
R38	Irritating to skin	S51	Use only in well ventilated areas
R39	Danger of very serious irreversible effects		
R40	Limited evidence of a carcinogenic effect		
R41	Risk of serious damage to the eyes		
R66	Repeated exposure may cause skin dryness or cracking		
R67	Vapours may cause drowsiness and dizziness		

Appendix F: Mathematical derivations and relations

Average hardness value

There are many different descriptive statistics that can be chosen as a measurement of the central tendency of the data items, but the most common method is the arithmetic mean which is defined as the sum of all the given values divided by the number of values. Here the average hardness value is calculated from Equation F.1 where n numbers are given, each number denoted by a_i, and i = 1, ..., n [55].

$$AVG = \frac{1}{n}\sum_{i=1}^{n} a_i \tag{F.1}$$

Standard deviation

Standard deviation is a widely used measure of the variability or dispersion, being easy to use though practically less robust than the expected deviation or average absolute deviation. The standard deviation of a data set is defined as the square root of the mean variance of all the values. Here the standard deviation is calculated from Equation F.2 where n numbers are given, each number denoted by a_i, and i = 1, ..., n. AVG is the average value explained above [55].

$$SD = \sqrt{\frac{1}{n}\sum_{i=1}^{n}(a_i - AVG)^2} \tag{F.2}$$

Relative error of the average needle length

When estimating the relative error of the average needle length, <l>, worst case scenario is assumed where all the needle parts that are sticking out of the matrix are cut during sample preparation. The sketch in Figure F.1 illustrates the principle used to derive a formula for this error, and the derivation itself is given by Equations F.3-F.8 [45]. All the symbols that are not explained here are given in Table G.1 in Appendix G.

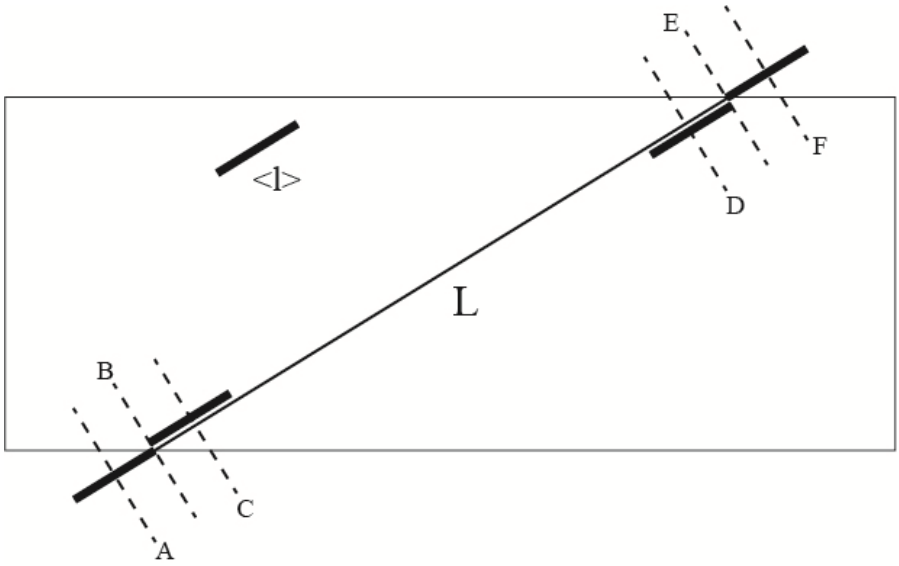

Figure F.1: Illustration related to estimation of error of the average needle length

$$f_{uncut} = \frac{CD}{AF} = \frac{L - < l >}{L + < l >} \tag{F.3}$$

$$f_{cut} = \frac{AC + DF}{AF} = \frac{2 < l >}{L + < l >} \tag{F.4}$$

$$L = \frac{L_0}{\cos\omega} \tag{F.5}$$

$$L_0 = \frac{t}{\tan\Phi} \tag{F.6}$$

$$< l >_m = f_{uncut} < l > + f_{cut} \frac{< l >}{2} = \frac{< l > L}{L + < l >} \tag{F.7}$$

$$\frac{\Delta < l >}{< l >} = \frac{< l > - < l >_m}{< l >} = 1 - \frac{< l >_m}{< l >} = 1 - \frac{1}{1 + \frac{< l >}{t} \cos\omega \tan\Phi}$$

$$= \frac{< l >_m}{t} \cos\omega \tan\Phi \tag{F.8}$$

Relative error of the needle number density

The relative error of the needle number density is calculated by rules of error propagation. The volume in Equation 2.16 in Chapter 2.6 is defined as given in Equation F.9 where A_m is the measured area in the TEM image and M is the image magnification [45]. Due to small uncertainties in the measured TEM image area and image magnification, the relative error for the volume becomes as given in Equation F.10 [45]. All the symbols that are not explained here are given in Table G.1 in Appendix G.

$$V = At = \frac{A_m t}{M^2} \tag{F.9}$$

$$\frac{\Delta V}{V} = \sqrt{\left(\frac{\Delta A_m}{A_m}\right)^2 + 4\left(\frac{\Delta M}{M}\right)^2 + \left(\frac{\Delta t}{t}\right)^2} \approx \frac{\Delta t}{t} \approx 10\% \tag{F.10}$$

From Equation 2.15 in Chapter 2.6 the relative error of the needle number density is obtained as shown in Equation F.11 [45]. The uncertainty in the number of precipitates is very small and will be neglected in the same way as shown above.

$$\frac{\Delta \rho_{\parallel}}{\rho_{\parallel}} = \sqrt{\left(\frac{\Delta N_{\parallel}}{N_{\parallel}}\right)^2 + \left(\frac{\Delta V'_{\parallel}}{V'_{\parallel}}\right)^2} \approx \left(\frac{\Delta V'_{\parallel}}{V'_{\parallel}}\right)^2 = \sqrt{\left(\frac{\Delta V}{V}\right)^2 + \frac{\left(\frac{\Delta < l >}{< l >}\right)^2 + \left(\frac{\Delta t}{t}\right)^2}{\left(1 + \frac{t}{< l >_m}\right)^2}} \tag{F.11}$$

Relative error of the precipitate volume fraction

The volume fraction of precipitates is defined in.16 in Chapter 2.6. The upper and lower limit for the relative precipitate volume fraction are then given by Equations F.12 and F.13, respectively [45]. All the symbols that are not explained here are given in Table G.1 in Appendix G.

$$\frac{\Delta VF}{VF} upper = \sqrt{\left(\frac{\Delta < CS >}{< CS >}\right)^2 + \left(\frac{\Delta < l >}{< l >}\right)^2} \tag{F.12}$$

$$\frac{\Delta VF}{VF}lower = \sqrt{\left(\frac{\Delta < CS >}{< CS >}\right)^2 + \left(\frac{\Delta V_{\parallel}'}{V_{\parallel}'}\right)^2} \qquad \text{(F.13)}$$

Here $\left(\Delta V_{\parallel}'/V_{\parallel}'\right)^2$ is defined in Equation F.11. Here the relative error of the cross section area, $\Delta < CS > / < CS >$, is given as the standard error divided by the average cross section area.

Appendix G: Nomenclature list

Table G.1: List of nomenclature

$\perp$	Normal to
$\parallel$	Parallel with
(fcc L10)	Space group
(100)	Crystallographic plane
[100]	Crystallographic direction
[110]	Crystallographic direction
[111]	Crystallographic direction
<100>	Family of crystallographic directions
<CS>	Average cross sectional area of needle/lath shaped precipitates
<l>	Average precipitate length
$<l>_m$	Average measured precipitate length
α	Pure aluminium phase
α'	Temperature correction slope
α_0	Original aluminium supersaturated solid solution
α_1	Composition of matrix in equilibrium with GP zones
α_2	Composition of matrix in equilibrium with θ''
α_3	Composition of matrix in equilibrium with θ'
α_4	Composition of matrix in equilibrium with θ'
β	Lattice parameter (angle)
β	Mg_2Si precipitate, stable
β'	$Mg_{1,8}Si$ precipitate, metastable
β''	Mg_5Si_6 precipitate, most likely also contains some alumina, metastable
γ	Lattice parameter (angle)
γ_b	Specific boundary energy
γ_s	Surface energy
$\Delta < CS > / < CS >$	Relative error of average precipitate cross section area
$\Delta < l > / < l >$	Relative error of average precipitate needle length
$\Delta\rho_{\parallel} / \rho_{\parallel}$	Relative error of number density
$\Delta\sigma_r$	Strength from rod-like precipitates
$\Delta\sigma_s$	Strength from spherical precipitates
$\Delta A_m / A_m$	Relative error of measured image area
ΔG^*	Activation energy barrier
$\Delta M / M$	Relative error of image magnification
$\Delta N_{\parallel} / N_{\parallel}$	Relative error of volume with correction (precipitate length || [001])
$\Delta t / t$	Relative error of specimen thickness
$\Delta V / V$	Relative error of volume
$\Delta V'_{\parallel} / V'_{\parallel}$	Relative error of volume with correction (precipitate length || [001])
$\Delta VF / VF\ lower$	Relative error of volume fraction of precipitates, lower limit
$\Delta VF / VF\ upper$	Relative error of volume fraction of precipitates, upper limit
θ	Incoherent Al_2Cu precipitate, stable
θ'	Semicoherent Al_2Cu precipitate, metastable
θ''	Coherent Al_2Cu precipitate, metastable
µm	Micrometers

λ	Inelastic mean free path
ρ	Electrical resistivity
$\rho_{\|\|}$	Number density of precipitates || [001]
ρ_i	Specific electrical resistivity of the *i*th solute
ρ_{ppt}	Contribution of precipitates to resistivity
$\rho_{pure}(T)$	Temperature dependent resistivity term,
Σ	Summation operator
σ	Electrical conductivity
σ'	Electrical conductivity value known or measured at temperature T’
τ	Strength
τ_b	Bypassing stress
τ_s	Shear stress
Φ	Tilt angle in order to obtain a <100> direction
Φ_1	Tilt angle in a certain direction
Φ_2	Tilt angle in a certain direction
ψ	Constant
Ω	Ohm
ω	Angle showing how the [100] and [010] direction are oriented
A	Image area
a	Lattice constant
AA6xxx	Aluminium alloys with Mg and Si as alloying elements
a_i	Value of a given number
$\mathbf{a}_{B'}$	Lattice constant direction in B' precipitate
AC	Line segment
AF	Line segment
A_m	Measured image area
$\mathbf{a}_{U2}$	Lattice constant direction in U2 precipitate
Al	Aluminium
APB	Anti-phase boundary
Ar^+	Argon ion
at%	Atomic percent
AVG	Average value
b	Lattice constant
B'	$Mg_9Al_4Si_7$ precipitate
b_l	Burgers length
b_v	Burgers vector
c	Lattice constant
*C*2/*m*	Space group
CBD	Convergence beam diffraction
CCD	Charge coupled device
CD	Line segment
C_i	Concentration of the *i*th solute
CO	Carbon monoxide
CO_2	Carbon dioxide
CS	Cross sectional area of needle/rod shaped precipitates
Cu	Copper
$\bar{d}$	Average indentation diagonal
DC	Direct-chill
DF	Line segment
DFT	Discret Fourier Transform
EDS	Energy dispersive spectroscopy
EELS	Electron energy loss spectroscopy

eV	Electron volt
F	Load in kg
f	Function
fcc	Face-centred cubic crystal system
f_{cut}	Fraction cut precipitates
Fe	Iron
FFT	Fast Fourier Transform
$F_{m\bar{3}m}$	Space group
f_p	Volume fraction of precipitates
f_r	Volume fraction of rod precipitates
f_s	Mean volume fraction of spherical pre-β precipitates
f_{uncut}	Fraction uncut precipitates
G	Shear modulus
G_0	Free energy for α_0
G_1	Free energy for α_1 + GP zones
G_2	Free energy for α_2 + θ"
G_3	Free energy for α_3 + θ'
G_4	Free energy for α_4 + θ
GP	Guinier-Preston
H_2O	Water
HRTEM	High resolution transmission electron microscopy
i	Value number
I_0	Sum of zero-loss peak counts
I_t	Sum of total spectrum counts
k	Kilo
KK	Kimdanningskontroll
KK5	Al-Mg-Si alloy (Mg:Si = 1,41)
KK5 BP	KK5 artificially aged to a time before maximum hardness at overaged condition
KK6	Al-Mg-Si alloy (Mg:Si = 0,39)
KK7	Al-Mg-Si alloy (Mg:Si = 0,75)
kV	Kilovolt
L	Geometrical length parallel to [010] and normal to [001]
L_0	Geometrical length normal to [001] as a function of L
M	Image magnification
m	Meters
MFP	Mean free path
Mg	Magnesium
mm	Millimeters
min	Minutes
Mn	Manganese
MPa	Mega Pascal
M_T	Taylor factor
$N_{\|\|}$	Number of precipitates parallel with [001]
n	Number of values
nm	Nanometers
n_s	Surface normal
$P_{\bar{3}m1}$	Space group
$P6_3/m$	Space group
P_{nma}	Space group
P_z	Zener pinning pressure
r	Precipitate radius
r_0	Inner cut-off of radius

R_1	Distance between 000 and another reflection
R_2	Distance between 000 and a second reflection
R_3	Distance between 000 and a third reflection
r_{crit}	Critical precipitate radius
r_r	Cross sectional radius
r_s	Mean radius of spherical pre-β precipitates
R(xx)	Risk phrase, xx indicates a certain number of risk phrase
S	Siemens
SD	Standard deviation
Si	Silicone
SSSS	Supersaturated solid solution
STEM	Scanning transmission electron microscope
S(xx)	Safety phrase, xx indicates a certain number of safety phrase
T	Temperature at which conductivity value needs to be known
t	Specimen thickness
T'	Temperature at which known or measured value was obtained
$t'_{\perp}$	Specimen thickness plus length of precipitate normal to [001]
$t'_{\parallel}$	Specimen thickness plus length of precipitate parallel with [001]
T_1	Solution heat treatment temperature
T_2	Artificial ageing temperature
TEM	Transmission electron microscopy
TiN	Titanium nitride
Torr	Non-SI unit of pressure with the ratio of 760 to 1 standard atmosphere
U1	$MgAl_2Si_2$ precipitate
U2	$Mg_4Al_4Si_4$ precipitate
V	Volume
$V'_{\parallel}$	Volume with correction (precipitate length || [001])
VF	Volume fraction of precipitates
V_{max}	Maximum extrusion speed
wt%	Weight percent
yy	Load in kg
Zn	Zink
xxx	Vickers hardness number
xxxHVyy	Representation of Vickers hardness number